### Прилог 1:

# Доказ о научним публикацијама категорије M21 и M52

Volume 25 Number 42 14 November 2023 Pages 28543-29366

## PCCP

Physical Chemistry Chemical Physics rsc.li/pccp



ISSN 1463-9076



#### **PAPER**

Frank De Proft *et al.*The electrophilic aromatic bromination of benzenes: mechanistic and regioselective insights from density functional theory



#### PCCP



View Article Online **PAPER** 



Cite this: Phys. Chem. Chem. Phys., 2023, 25, 29017

#### Ab-initio calculations of temperature dependent electronic structures of inorganic halide perovskite materials†

Milan Jocić and Nenad Vukmirović \*

Despite wide interest in halide perovskite materials, it is still challenging to accurately calculate their electronic structure and its temperature dependence. In this work, we present ab-initio calculations of the temperature dependence of the electronic structure of CsPbX3 materials (X = Cl, Br or I) in the cubic form and of the zero temperature electronic structure of the orthorhombic phase of these materials. Phononinduced temperature dependent band energy renormalization was calculated within the framework of Allen-Heine-Cardona theory, where we exploited the self-consistent procedure to determine both the energy level shifts and their broadenings. The phonon spectrum of the materials was obtained using the self-consistent phonon method since standard density functional perturbation theory calculations in harmonic approximation yield phonon modes with imaginary frequencies due to the fact that the cubic structure is not stable at zero temperature. Our results suggest that low energy phonon modes mostly contribute to phonon-induced band energy renormalization. The calculated values of the band gaps at lowest temperature where the material exhibits a cubic structure are in good agreement with experimental results from the literature. The same is the case for the slope of the temperature dependence of the band gap for the CsPbI<sub>3</sub> material where reliable experimental data are available in the literature. We also found that phonon-induced temperature dependence of the band gap is most pronounced for the conduction band minimum and valence band maximum, while other bands exhibit a weaker dependence.

Received 4th May 2023, Accepted 26th September 2023

DOI: 10.1039/d3cp02054a

rsc.li/pccp

#### 1 Introduction

Halide perovskite materials emerged in the last decade as revolutionary materials for applications in solar cells, 1-4 lasers,<sup>5</sup> light-emitting diodes,<sup>6,7</sup> photodetectors,<sup>8,9</sup> detectors of ionizing radiation, 10,11 thermoelectric and other devices. 13 To understand the characteristics of these devices and to design improved materials and devices, it is essential to be able to predict the electronic structure of the material. Despite great interest in understanding the electronic structure of halide perovskites and numerous developments of the methods for electronic structure calculations and the software for performing such calculations, it is still rather challenging to accurately determine the electronic structure of halide perovskites.

It is currently well understood that in electronic structure calculations of halide perovskites one has to take into account the effects of spin-orbit interactions due to the presence of

Institute of Physics Belgrade, University of Belgrade, Pregrevica 118, 11080 Belgrade, Serbia. E-mail: milan.jocic@ipb.ac.rs, nenad.vukmirovic@ipb.ac.rs † Electronic supplementary information (ESI) available: Supplementary figures and cif files with initial and relaxed coordinates of the orthorhombic structure of CsPbX<sub>3</sub> materials. See DOI: https://doi.org/10.1039/d3cp02054a

heavy atoms such as lead. 14-16 As in the case for many other semiconductors, standard local or semilocal approximations to density functional theory (DFT) underestimate the material band gap<sup>14-16</sup> and more sophisticated approaches, such as the use of GW approximation<sup>17–19</sup> or hybrid functionals, <sup>20,21</sup> are necessary.

A group of challenges arises when it comes to predicting the electronic structures of halide perovskites at room or higher temperatures which are relevant for application in the mentioned devices. Temperature effects on the band gap and the overall electronic structure of perovskites are rather pronounced<sup>22-28</sup> and one cannot simply consider the electronic structure calculated for fixed atoms in a crystal lattice as the electronic structure at higher temperatures.

The most successful theory for determining the temperature effects on the electronic structure of semiconductors is the Allen-Heine-Cardona theory.<sup>29-31</sup> Within this theory, one expands the Hamiltonian up to second order terms in atomic displacements from the equilibrium position and perturbatively evaluates the change in band energies. In conjunction with the methods for the electronic structure calculation for fixed atomic positions, this theory was used to study the temperature dependence of the band gap and zero temperature band gap renormalization in a variety of semiconductors. 31-36 However, this theory can be

straightforwardly applied to a particular material only if its crystal structure at a given temperature is the same as at zero temperature.

The last condition is not fulfilled in halide perovskite materials. Inorganic halide perovskite materials CsPbX<sub>3</sub> (X = Cl, Br or I) that are of main interest in this work exhibit a cubic structure at high temperatures only.  $^{37-42}$  As the temperature is lowered, they transform into a tetragonal structure and finally to an orthorhombic structure.  $^{37-40}$  Therefore, the cubic structure is not a stable structure at zero temperature. When one attempts to calculate the phonon dispersion in the material by assuming a cubic structure at zero temperature, phonon modes of imaginary frequencies are obtained  $^{40,43-45}$  and it is not clear how to treat such phonons within the Allen–Heine–Cardona theory.

Previous studies on the effects of temperature on halide perovskite semiconductors have not addressed other bands than the conduction band minimum (CBM) and the valence band maximum (VBM). While these two bands are most relevant for the determination of the band gap of the material, there is significant interest in knowing the energies of the other bands. These are important, for example, to understand the optical response of the material in the ultraviolet spectral range relevant for ultraviolet detectors.9 On the theoretical side, the knowledge of band energies at characteristic points in the Brillouin zone is necessary to construct multiband Hamiltonians46-49 that can further be used to predict the electronic states in halide perovskite nanostructures. While the renormalization of energies of the other bands can in principle be obtained in the same way as for CBM and VBM within Allen-Heine-Cardona theory, certain issues, related to the energy level broadening parameter  $\delta$ , arise. On the one hand, band renormalization for other bands converges linearly with respect to  $\delta$  when  $\delta \rightarrow 0$  in contrast to Lorentzian convergence of CBM and VBM,32 which makes it more challenging to obtain the convergence of other bands. On the other hand, other bands typically exhibit larger broadening of energy levels compared with the CBM and VBM. Consequently, it is questionable if one should evaluate the  $\delta \rightarrow 0$ limit for other bands at all. Preferably, the broadening of the energy levels should be evaluated simultaneously with the band energy renormalization.

In this work, we perform electronic structure calculations of the temperature dependence of the band gap and band energies for halide perovskite materials CsPbX<sub>3</sub> (X = Cl, Br or I) in a cubic crystal structure. Electronic structure calculations (without the effects of phonon-induced band renormalization) are performed using a hybrid functional that satisfies the Koopmans condition. The challenge of treating phonons within the Allen-Heine-Cardona theory is overcome by performing phonon band structure calculations at a finite temperature within the framework of self-consistent phonon (SCPH) theory, where all phonon modes remain stable. The challenge of the choice of energy level broadening is overcome by performing the calculation in which energy levels and their broadening are determined selfconsistently. We compare the obtained temperature dependence of the band gap for the cubic structure to experimental results from the literature. We also perform calculations of the orthorhombic structure at zero temperature and comment on the

overall temperature dependence of the band gap of CsPbX<sub>3</sub> materials from zero to high temperatures.

This paper is organized as follows. In Section 2, we present the main methods that were used in this work. Allen-Heine-Cardona theory is briefly reviewed in Section 2.1 along with the description of the two approaches that were used to calculate phonon-induced band energy renormalization within this theory. The SCPH method is reviewed in Section 2.2. In Section 3 we present the results obtained and the details of the calculations. We start with the results obtained using standard density functional theory (DFT) calculations with semilocal functionals that are presented in Section 3.1. In Section 3.2 we present the results obtained using a hybrid functional that gives improved values of the material band gap. Density functional perturbation theory (DFPT) based calculations of the phonon spectrum are reported in Section 3.3, while SCPH calculations of the phonon spectrum are presented in Section 3.4. In Sections 3.5 and 3.6 we present the main results of this work for the temperature dependence of renormalization of band energies, while we compare the results obtained with experiments in Section 3.7. We close the paper with a discussion and conclusions in Section 4.

#### 2 Methods

#### 2.1. Allen-Heine-Cardona theory

In this section, we briefly review the Allen–Heine–Cardona theory that describes phonon-induced band gap renormalization in semi-conductor materials and present the procedure for self-consistent calculation of phonon-induced renormalization of band energies and their broadenings. The Hamiltonian of the system is given as

$$H = H_{\rm el} + H_{\rm ph} + H_{\rm el-ph}.$$
 (1)

The first term

$$H_{\rm el} = \sum_{kn} \varepsilon_{kn} \hat{c}_{kn}^{\dagger} \hat{c}_{kn}, \qquad (2)$$

describes the electrons, where  $\hat{c}_{kn}^{\dagger}$  and  $\hat{c}_{kn}$  are creation and annihilation operators, respectively, of an electron with wave vector k and electronic band n whose energy is  $\varepsilon_{kn}$ . The second term

$$H_{\rm ph} = \sum_{\boldsymbol{q}\nu} \hbar \omega_{\boldsymbol{q}\nu} \left( \hat{a}^{\dagger}_{\boldsymbol{q}\nu} \hat{a}_{\boldsymbol{q}\nu} + \frac{1}{2} \right) \tag{3}$$

describes the phonons, where  $\hat{a}_{q\nu}^{\dagger}$  and  $\hat{a}_{q\nu}$  are phonon creation and annihilation operators, respectively, of a phonon with wave vector  $\boldsymbol{q}$  and phonon mode  $\nu$  whose angular frequency is  $\omega_{q\nu}$ . The third term  $H_{\text{el-ph}}$  is the Hamiltonian of the electron–phonon interaction. By including the terms up to second order with respect to atomic displacements, it takes the form

$$H_{\text{el-ph}} = \frac{1}{N_q^{1/2}} \sum_{kmn} \sum_{\boldsymbol{q}\nu} g_{mm,\nu}^{\text{Fan}}(\boldsymbol{k}, \boldsymbol{q}) \hat{c}_{\mathbf{k}+\mathbf{q}m}^{\dagger} \hat{c}_{\mathbf{k}n} (\hat{a}_{-\mathbf{q}\nu}^{\dagger} + \hat{a}_{\mathbf{q}\nu})$$

$$+ \frac{1}{N_q} \sum_{kmn} \sum_{\boldsymbol{q}\boldsymbol{q}'\nu\nu'} g_{nm,\nu\nu'}^{\text{DW}}(\boldsymbol{k}, \boldsymbol{q}, \boldsymbol{q}') \hat{c}_{\boldsymbol{k}+\boldsymbol{q}+\boldsymbol{q}'m}^{\dagger} \hat{c}_{\mathbf{k}n}$$

$$\times (\hat{a}_{-\mathbf{q}\nu}^{\dagger} + \hat{a}_{\mathbf{q}\nu}) (\hat{a}_{-\mathbf{q}'\nu'}^{\dagger} + \hat{a}_{\mathbf{q}'\nu'}),$$

$$(4)$$

where  $g_{\mathrm{nm},\nu}^{\mathrm{Fan}}(\pmb{k},\pmb{q})$  and  $g_{nm,\nu\nu'}^{\mathrm{DW}}(\pmb{k},\pmb{q},\pmb{q}')$  are first order Fan and second order Debye-Waller matrix elements of electron-phonon interactions and  $N_q$  is the number of points in reciprocal space. The first order Fan matrix element is given as:

$$g_{nm,\nu}^{\text{Fan}}(\mathbf{k}, \mathbf{q}) = \sum_{\kappa\alpha} \left(\frac{\hbar}{2M_{\kappa}\omega_{\mathbf{q}\nu}}\right)^{1/2} \times \langle \mathbf{k} + \mathbf{q}n| \frac{\partial V_{\text{SCF}}}{\partial R_{\kappa\alpha}(\mathbf{q})} |\mathbf{k}m\rangle \xi_{\kappa\alpha,\nu}(\mathbf{q}) e^{i\mathbf{q}\cdot\mathbf{R}_{\kappa}}$$
(5)

where  $\frac{\partial V_{\text{SCF}}}{\partial R_{\kappa \alpha}(\boldsymbol{q})}$  and  $\xi_{\kappa \alpha, \nu}(\boldsymbol{q})$  are the perturbation of the Kohn–Sham

potential due to nuclear displacement and the phonon eigenvector, respectively, describing the displacement of atom  $\kappa$  with mass  $M_{\kappa}$ at position  $R_{\kappa}$  in Cartesian direction  $\alpha$  corresponding to phonon vector (mode)  $q(\nu)$ . The self-energy stemming from the first term in egn (4) reads

$$\Sigma_{kn}^{\text{Fan}}(\omega, T) = \frac{1}{N_q} \sum_{m, \mathbf{q}\nu} \left| g_{mm,\nu}^{\text{Fan}}(\mathbf{k}, \mathbf{q}) \right|^2 \times \left( \frac{n_{\mathbf{q}\nu}(T) + 1 - f_{\mathbf{k} + \mathbf{q}m}}{\omega - \varepsilon_{\mathbf{k} + \mathbf{q}m} - \omega_{\mathbf{q}\nu} + i\delta} + \frac{n_{\mathbf{q}\nu}(T) + f_{\mathbf{k} + \mathbf{q}m}}{\omega - \varepsilon_{\mathbf{k} + \mathbf{q}m} + \omega_{\mathbf{q}\nu} + i\delta} \right)$$
(6)

where  $n_{q\nu}(T)$  is the Bose-Einstein occupation factor at a temperature T,  $f_{k+qm}$  is the Fermi-Dirac occupation factor and  $\delta$  is a positive infinitesimal. The self-energy from the second term in eqn (4) takes the form

$$\Sigma_{knm}^{\text{DW}}(T) = \frac{1}{N_q} \sum_{\mathbf{q}\nu} g_{nm,\nu\nu}^{\text{DW}}(\mathbf{k}, \mathbf{q}, -\mathbf{q}) (2n_{\mathbf{q}\nu}(T) + 1), \tag{7}$$

where the second order electron-phonon matrix elements  $g_{nm,\nu}^{DW}$ (k, q, -q) from eqn (7) can be expressed in terms of first order electron-phonon matrix elements by making use of translational invariance and rigid-ion approximation.<sup>29,50</sup>

The renormalization of energy levels can be calculated from the self-energies. Within the so-called on-the-mass-shell (OTMS) approximation,  $^{51}$  the renormalized energy of band nat point k in the Brillouin zone is

$$E_{kn}(T) = \varepsilon_{kn} + \text{Re}\Sigma_{kn}^{\text{Fan}}(\varepsilon_{kn}, T) + \text{Re}\Sigma_{kn}^{\text{DW}}(T). \tag{8}$$

As discussed in the Introduction, there are challenges in obtaining converged results for band energy renormalization for bands other than VBM and CBM using eqn (6), (7) and (8). The convergence with respect to energy level broadening parameter  $\delta$  as  $\delta \to 0$  is a slow linear convergence<sup>32</sup> and hence one needs to use rather small  $\delta$ , which in turn requires a large number of *q*-points in the summation. The broadening of the energy levels obtained from the imaginary part of the self-energy is on the order of 100 meV or more. It is therefore questionable if the  $\delta \to 0$  limit is relevant at all. It is certainly more appropriate to self-consistently determine the renormalization and broadening of the energy levels. This can be achieved as follows. We note first that the terms  $\frac{1}{\omega - \varepsilon_{k+qm} \pm \omega_{q\nu} + i\delta}$  in eqn (6) represent the retarded Green's function of a bare electron  $G_{k+qm}^{(0)}(\omega \pm$ 

 $\omega_{a\nu}$ ), while eqn (6) is the self-energy in the so-called Migdal approximation. A more accurate approximation is the selfconsistent Migdal approximation where the bare Green's function  $G^{(0)}$  is replaced with the dressed Green's function G. Eqn (6) then takes the form

$$\Sigma_{kn}^{\text{Fan}}(\omega) = \frac{1}{N_q} \sum_{m,q\nu} \left| g_{nm,\nu}^{\text{Fan}}(\boldsymbol{k}, \boldsymbol{q}) \right|^2 \times \left[ (n_{q\nu}(T) + 1 - f_{k+qm}) G_{k+qm}(\omega - \omega_{q\nu}) + (n_{q\nu}(T) + f_{k+qm}) G_{k+qm}(\omega + \omega_{q\nu}) \right].$$

$$(9)$$

One can in principle determine the Green's function, the selfenergy, the spectral function and hence the energy level renormalization and broadening by self-consistently solving eqn (9) and the Dyson equation. However, this requires evaluation of all these quantities at wave vectors throughout the whole Brillouin zone in each step of the self-consistent procedure, which is a highly demanding computational task. A significant simplification that decouples different kn states can be made as follows. We first note that the Green's function in eqn (9) is given as

$$G_{k+qm}(\omega) = \frac{1}{\omega - \varepsilon_{k+qm} - \Sigma_{k+qm}(\omega)}.$$
 (10)

We then make a replacement  $\Sigma_{k+qm}(\omega) \rightarrow \Sigma_{kn}(\omega)$  in the previous equation (where  $\Sigma_{kn}(\omega) = \Sigma_{kn}^{\text{Fan}}(\omega) + \Sigma_{kn}^{\text{DW}}$ ). This replacement is justified by the fact that the dominant contribution to the sum in eqn (9) comes from the terms in the sum that have m = n and a small value of **q**. For such terms  $\Sigma_{k+qm}(\omega) \approx \Sigma_{kn}(\omega)$ . It is therefore appropriate to replace the self-energy for all terms in the sum with the self-energy of the dominant terms. The expression for  $\Sigma_{kn}^{\text{Fan}}$  then reads

$$\Sigma_{kn}^{\text{Fan}}(\omega) = \frac{1}{N_q} \sum_{m,q\nu} \left| g_{nm,\nu}^{\text{Fan}}(\mathbf{k}, \mathbf{q}) \right|^2 \times \left( \frac{n_{q\nu}(T) + 1 - f_{k+qm}}{\omega - \varepsilon_{k+qm} - \omega_{q\nu} - \Sigma_{kn}(\omega - \omega_{q\nu})} \right) + \frac{n_{q\nu}(T) + f_{k+qm}}{\omega - \varepsilon_{k+qm} + \omega_{q\nu} - \Sigma_{kn}(\omega + \omega_{q\nu})} \right).$$
(11)

It is important to note that eqn (11) does not contain the self-energies of the states other than kn, which is a consequence of the approximation used for  $\Sigma_{k+qm}(\omega)$ . The self-energy  $\Sigma_{kn}^{\text{Fan}}(\omega)$  can now be obtained using a self-consistent procedure as follows. One starts with an initial guess for  $\Sigma_{kn}(\omega)$  and evaluates  $\Sigma_{kn}^{\text{Fan}}(\omega)$  using eqn (11) and the total self-energy as the sum of the Fan and the Debye-Waller term. A new value of  $\Sigma_{kn}^{\text{Fan}}(\omega)$  is then calculated again using eqn (11) and the procedure is repeated until the convergence of  $\Sigma_{kn}^{\text{Fan}}(\omega)$  is reached. The spectral function is then obtained as

$$A_{kn}(\omega) = -\frac{1}{\pi} \operatorname{Im} \frac{1}{\omega - \varepsilon_{kn} - \Sigma_{kn}(\omega)}$$
 (12)

and the renormalized energy  $E_{kn}$  is obtained as the energy  $\omega_{max}$ at which the spectral function reaches a maximum. The spectral function  $A_{kn}(\omega)$  represents the probability density that an

electron of momentum k in band n has the energy  $\omega$ . We note that our procedure for evaluation of renormalized energies is similar in spirit to the procedure suggested in ref. 50 (Eq. 166 therein), where approximations that also lead to decoupling of different kn states were used. The difference between these procedures is that we consider the full frequency dependence of self-energies rather than the energy of the renormalized state and its broadening only.

In Section 3, we will present the results obtained using both of the mentioned approaches. The results obtained from eqn (8) with self-energies given by eqn (6) and (7) will be referred to as OTMS results, while the results obtained using egn (12) and self-consistent solution of egn (11) will be referred to as the self-consistent procedure (SCP) results.

We note that it is rather challenging to treat the electronphonon interaction in real materials beyond the approximations mentioned. These approximations all contain the assumption that the electron-phonon interaction is not too strong. Full nonperturbative treatment of electron-phonon interactions has so far only been performed for model Hamiltonians, such as the Holstein or Fröhlich model. In a recent study of the Holstein model<sup>52</sup> it was shown that for relatively weak electron-phonon coupling the spectral functions in the Migdal and self-consistent Migdal approximation are similar to the spectral functions obtained using more advanced approaches, such as the cumulant expansion method and the dynamical mean field theory. Moreover, self-consistent Migdal approximation performs overall only somewhat worse than the cumulant expansion method, which is not the case for the Migdal approximation that gives inaccurate results starting from moderate values of electronphonon coupling. Based on the knowledge gained from the Holstein model, we can infer about the accuracy of the OTMS and SCP results for real perovskite materials. It is expected that the SCP results which are based on the self-consistent Migdal approximation should in principle be more accurate than the OTMS results which are based on the Migdal approximation. On the other hand, it will be shown in Section 3 that OTMS and SCP results are not too different. This suggests that we are in the regime where electron-phonon coupling is relatively weak, where it is appropriate to apply either the Migdal or the selfconsistent Migdal approximation.

We also note that in both the OTMS and SCP approach, as typically done in the literature, 50 we were evaluating only the diagonal (intraband) self-energies  $\Sigma_{kn}(\omega)$  and not the offdiagonal (interband) self-energies  $\Sigma_{knm}(\omega)$  (with  $n \neq m$ ). In the case of the OTMS approach one is actually interested in diagonal self-energies only because they directly determine the band energy renormalization, see eqn (8). On the other hand, introduction of off-diagonal self-energies in the SCP approach would strongly increase the computational burden of the whole procedure. On physical grounds, it should be noted that band energy renormalization due to interband electron-phonon scattering processes is already described by the diagonal self-energies [via the  $m \neq n$  terms in the sum in eqn (6)]. Hence, inclusion of non-diagonal self-energies would represent only a higher order effect.

#### 2.2. The self-consistent phonon method

Since the standard approach based on the use of harmonic approximation and DFPT is not sufficient to describe phonons in cubic CsPbX<sub>3</sub> materials, a more sophisticated approach is needed. We therefore use the self-consistent phonon method following the methodology and the implementation of ref. 53. In this section, we briefly review the main ideas of the method and its implementation.

In the Born-Oppenheimer approximation, the dynamics of lattice ions is described by the Hamiltonian H = T + U, where T is their kinetic energy, while U is the potential energy which is a function of the displacements from the equilibrium position. The potential energy can be expanded as  $U = U_0 + U_2 + U_3 + U_4 + U_4$ ..., where the term  $U_n$  is of n-th order with respect to atomic displacements and the term  $U_1$  is missing because it contains forces which are zero in equilibrium. Keeping the terms  $U_0$  and  $U_2$  only is the standard harmonic approximation. In this case, phonon frequencies are obtained from diagonalization of the corresponding dynamical matrix.

To obtain the phonon frequencies in a general case when the terms beyond  $U_2$  are included, one can make use of many body Green's function theory. The Hamiltonian is divided into  $H = H_0 + H_1$  where  $H_0 = T + U_0 + U_2$  is the harmonic part of the Hamiltonian whose solution is known, while the anharmonic terms  $H_1 = U_3 + U_4 + \dots$  constitute the interaction part. The phonon Green's function  $G_0$  for the Hamiltonian  $H_0$  is known, while the Dyson equation relates  $G_0$ , the phonon Green's function G of the Hamiltonian H and the self-energy  $\Sigma$ . The Dyson equation has to be complemented with the equation for selfenergy. The self-energy is in principle given by a diagrammatic expansion involving an infinite number of Feynman diagrams.

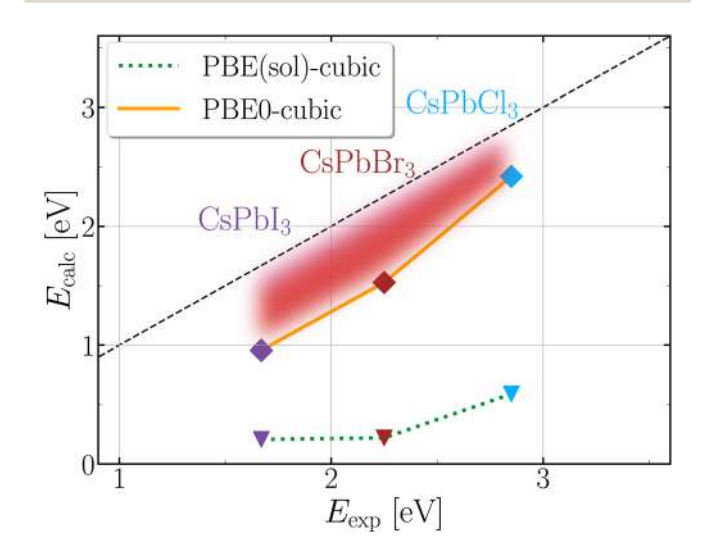


Fig. 1 Comparison of experimental and theoretical results for the electronic gap for  $CsPbX_3$  (X = Cl, Br or I) calculated without taking temperature effects into account. The line x = y represents the experimental results for the lowest temperature of the cubic structure. The symbols denote calculated values for the cubic structure using the PBE (PBEsol) functional for CsPbI3 (CsPbCl3 and CsPbBr3) (inverted triangles) and PBE0 functional modified to satisfy the Koopmans condition (diamonds)

In practice one selects only the most relevant diagrams for the problem at hand. To obtain the renormalized phonon frequencies, it turns out that the most relevant diagram is the loop diagram originating from the quartic term  $U_4$  (shown in Fig. 1(a) in ref. 53). The Green's function and the self-energy can then be found self-consistently and the renormalized phonon frequency is determined from the pole of the Green's function.

To perform the calculation within the SCPH method, one also has to obtain all relevant force constants that appear in the  $U_n$ terms in the expansion of U. The second order force constants are obtained from supercell density functional theory calculations and the finite displacement method. While the finite displacement method can in principle be used to obtain higher order force constants, a different strategy yields more stable results for the force constants. Namely, finite-temperature ab-initio molecular dynamics calculations are performed to obtain various atomic configurations and the corresponding total energy and forces in these configurations. The force constants that appear in anharmonic terms in *U* are then fitted to the data obtained, where great care has to be taken to avoid overfitting the data. Details of the full calculation protocol are reported in Section 3.4.

#### Results and calculation details

#### 3.1. Density functional theory calculations with semilocal functionals

As a first step, we performed density functional theory calculations of the electronic structure of the CsPbX<sub>3</sub> materials using the semilocal PBEsol54 functional in the case of CsPbCl3 and CsPbBr<sub>3</sub>, while the PBE functional<sup>55</sup> was used in the case of CsPbI<sub>3</sub>. Calculations were performed using the plane-wave code Quantum Espresso. 56,57 Norm-conserving fully relativistic pseudopotentials<sup>58,59</sup> were used to treat the effect of core electrons. The effects of spin-orbit interaction were included. The wave functions were represented on a  $4 \times 4 \times 4$  reciprocal space k-point grid with a kinetic energy cutoff of 50 Ry for CsPbCl<sub>3</sub> and CsPbBr<sub>3</sub> and a cutoff of 40 Ry for CsPbI<sub>3</sub>. We note that a different functional was used for CsPbI<sub>3</sub> because the gap obtained using the PBEsol functional at the optimized lattice constant obtained from this functional is nearly zero, which prevents the use of this functional in further DFPT calculations.

The optimized lattice constants for the cubic structure obtained from the calculations are respectively 10.6  $a_0$ , 11.1  $a_0$ and 12.1  $a_0$  (in units of first Bohr radius  $a_0$  for CsPbCl<sub>3</sub>, CsPbBr<sub>3</sub> and CsPbI<sub>3</sub>). We note that the lattice constants obtained for CsPbCl3 and CsPbBr3 are in excellent agreement with the experimental lattice constant at the lowest temperature where the material exhibits a cubic structure (which are 10.59  $a_0$  at 320 K for CsPbCl<sub>3</sub> and 11.10  $a_0$  at 403 K for CsPbBr<sub>3</sub>, see ref. 42). This agreement is reasonable in the case of CsPbI<sub>3</sub> (experimental lattice constant is 11.67  $a_0$  at 300 K, see ref. 60) and would be better if the PBEsol functional, which gives the lattice constant of 11.8  $a_0$ , was used. However, as noted before, the use of PBEsol functional for CsPbI3 closes the gap of the material and hence this functional was not used for CsPbI<sub>3</sub>. While the agreements obtained are somewhat fortuitous because standard DFT calculations are performed at zero temperature, the lattice constants obtained were used in further calculations because they are in good agreement with experimental lattice constants. The direct band gaps at the R-point obtained for CsPbCl3, CsPbBr3 and CsPbI<sub>3</sub> are respectively 0.59 eV, 0.22 eV and 0.21 eV. These gaps are well below the experimental band gaps, see Fig. 1. This is expected because it is well known that semilocal functionals underestimate the band gap.61

We also performed calculations for the orthorhombic structure of the CsPbX<sub>3</sub> material that is stable at zero temperature. The coordinates of the initial structure were taken from The Materials Project website<sup>62</sup> as structures numbered 675 524, 567 629, and 1 120 768 for CsPbCl<sub>3</sub>, CsPbBr<sub>3</sub> and CsPbI<sub>3</sub>, respectively, and were further relaxed (cif files for the initial and relaxed structures are included in the ESI†). The CsPbCl3 orthorhombic structure corresponds to space group number 38 (Amm2) with 10 atoms per primitive cell, while CsPbBr<sub>3</sub> and CsPbI<sub>3</sub> orthorhombic structures both correspond to space group number 62 (Pmna) with 20 atoms per primitive cell. The same density functionals, k-point grid dimension, and the plane wave kinetic energy cutoff were used as in the case of the cubic structure. We used the PBEsol functional for optimization of atomic coordinates and dimensions of the unit cell for all three materials (since the gap of orthorhombic CsPbI3 does not close when the PBEsol functional is used in the calculation). The calculations were performed using the Quantum Espresso code56,57 with variable cell relaxation option. The band gaps obtained for orthorhombic CsPbCl<sub>3</sub>, CsPbBr<sub>3</sub> and CsPbI<sub>3</sub> are respectively 1.1 eV, 0.83 eV and 0.62 eV.

#### 3.2. Hybrid functional calculations

To overcome the band gap problem of semilocal functionals, we performed the electronic structure calculation using a hybrid functional. In particular, we make use of the PBE0 functional<sup>63,64</sup> whose parameter  $\alpha$  is chosen to satisfy the Koopmans condition. We used the values of α for CsPbX<sub>3</sub> materials that were calculated in ref. 65. Hybrid functional calculations were also performed using the Quantum Espresso code. 56,57,66 The calculation parameters common to standard semilocal DFT calculation were 4 reciprocal q-points grid was used to sample the Fock operator and the Gygi-Baldereschi method<sup>67</sup> was used to treat the singularity at  $q \to 0$ . For orthorhombic structures that have a larger unit cell than cubic structures,  $3 \times 3 \times 2$  k- and q-points grids were used in the case of CsPbBr3 and CsPbI3, while we used 4  $\times$  $4 \times 4$  k- and q-points grids for CsPbCl<sub>3</sub>.

In hybrid functional calculations, we obtain the values of 2.4 eV, 1.5 eV and 0.96 eV for the band gap of cubic CsPbCl<sub>3</sub>, CsPbBr3 and CsPbI3. These values are closer to experimental values than the values obtained from semilocal functionals. However, these values are still smaller than the experimental band gaps, see Fig. 1. This result indicates that temperature effects might play a significant role and that it is important to investigate them.

In the case of orthorhombic structures, we obtain band gaps of 3.0 eV, 2.4 eV and 1.5 eV, respectively for CsPbCl<sub>3</sub>, CsPbBr<sub>3</sub>

**Paper** 

and CsPbI3. These results are in good agreement with experimental gaps of the low-temperature orthorhombic structures, which are 3.056 eV for CsPbCl<sub>3</sub> (ref. 68), 2.25 eV for CsPbBr<sub>3</sub> (ref. 69) and 1.72 eV for CsPbI<sub>3</sub> (ref. 70).

#### 3.3. Density functional perturbation theory calculations of the phonon band structure

To take into account the effect of temperature on the electronic band structure, it is necessary to calculate the phonon frequencies and eigenvectors and the electron-phonon coupling constants. For this reason, we perform DFPT calculations of phonons in harmonic approximation. The same density functional, kinetic energy cutoff and the reciprocal space k-point grid were used as in DFT calculations. The calculations were performed using the ABINIT code.71-74

The phonon band structures obtained from calculations for cubic CsPbX<sub>3</sub> materials are presented in Fig. 2 (dashed line), where phonons with imaginary frequencies are presented using negative values. Since the cubic structure is not stable at zero temperature, there is a significant number of phonon modes with imaginary frequencies. It is therefore a challenge to include such modes in the calculation of phonon-induced band renormalization.

#### 3.4. Calculation of phonon band structure within the self-consistent phonon method

Standard DFPT calculations of the phonon band structure assume zero temperature and the harmonic approximation. As discussed in Section 3.3, this leads to phonon modes with imaginary frequencies for the cubic structure. To overcome this issue, one has to take into account the anharmonic effects and the effects of temperature. This can be naturally accomplished using the self-consistent phonon method. 53,75

The calculations based on the SCPH method were performed using the following protocol. The calculations were performed using the ALAMODE code, 53,76 while DFT calculations and ab-initio molecular dynamics simulations were performed using the Quantum Espresso code. 56,57 One first has to obtain all relevant force constants. (i) Harmonic force constants were obtained by performing the DFT calculation of  $2 \times 2 \times 2$ cubic supercells, where a shifted  $4 \times 4 \times 4$  k-point grid was employed. Other parameters of the DFT calculation are the same as in Section 3.1. An atom is displaced by 0.01 Å in a certain direction and new atomic forces are calculated. The harmonic force constants are then obtained from these forces using a least squares fit implemented in the ALAMODE code. (ii) To obtain anharmonic force constants, we first generate representative atomic structures which will be used for evaluation of forces and subsequent force constant fitting. We perform 2000 steps of NVT ab-initio molecular dynamics at a temperature of 500 K with a timestep of 2 fs for a 2  $\times$  2  $\times$  2 cubic supercell. To gain computational speed in this calculation we reduce the kinetic energy cut-off to 30 Ry and we use the k-point grid consisting of the  $\Gamma$  point only. This is justified in this place, since the goal is only to obtain configurations where atoms are displaced from their equilibrium positions, rather than to extract physical quantities from the molecular dynamics

simulation. We then select 30 snapshots from the simulation which are equally spaced from timestep 500 to timestep 2000. (iii) For the snapshots obtained, we additionally displace each atom by up to 0.1 Å in each direction. For these 30 snapshots, we accurately compute the atomic forces from DFT by using 50 Ry kinetic energy cutoff and a shifted  $4 \times 4 \times 4$  k-point grid. (iv) With the forces obtained we perform fitting of the force constants using the adaptive LASSO method, following ref. 53 and 77. In the fitting, we put a restriction that fourth order force constants are zero beyond third neighbor atoms, that the fifth and sixth order constants are nonzero for nearest neighbors only and that higher order constants are equal to zero. (v) The force constants obtained in the previous step are used as an input for the SCPH method calculation. In the SCPH method calculation, we neglect the off-diagonal elements of the self-energy and use a  $4 \times 4 \times 4$  grid to represent the self-energy in reciprocal space.

The phonon band structure obtained from the SCPH method is presented in Fig. 2. We obtain phonon frequencies that are non-negative throughout the whole Brillouin zone. We also find that with an increase of temperature, a small but non negligible shift in frequencies is present. These shifts are negative for the three highest bands and positive for the rest. We will see in Section 3.5 that these shifts are large enough to have a significant contribution to the renormalization of electronic bands.

#### 3.5. Band energy renormalization calculations using the OTMS approach

In this section, we present the results for band energy renormalization calculations of cubic CsPbX3 materials obtained using the OTMS approach. The calculations, in this and in the following section, were performed using our own code which takes DFPT results from the ABINIT code. 71 These results include variations of the Kohn-Sham potential with respect to ionic displacements and the interatomic force constants, that are then used to calculate first and second order matrix elements of electron-phonon interaction. In all band energy renormalization calculations bare band energies that appear in egn (6) and (7) were taken from DFT calculations reported in Section 3.1.

To make sure that the results obtained are reliable one has to take enough q-points in the summations in eqn (6) and (7) and one has to check the sensitivity of the results to the value of the parameter  $\delta$  in eqn (6). It has been shown in ref. 32 that the band energy renormalization for polar materials converges as

 $\frac{1}{N_q}$  with the number of points  $N_q$  and that a Lorentzian type convergence for CBM and VBM energies of polar materials is obtained while decreasing  $\delta$ .

In ref. 22 phonon modes obtained within the harmonic approximation were used, however, the phonon modes with imaginary frequencies were simply disregarded. In this approach it remains unclear whether one should disregard only the phonons at certain q-points where their frequency becomes imaginary or one should disregard the whole phonon mode that produces an imaginary frequency in at least one

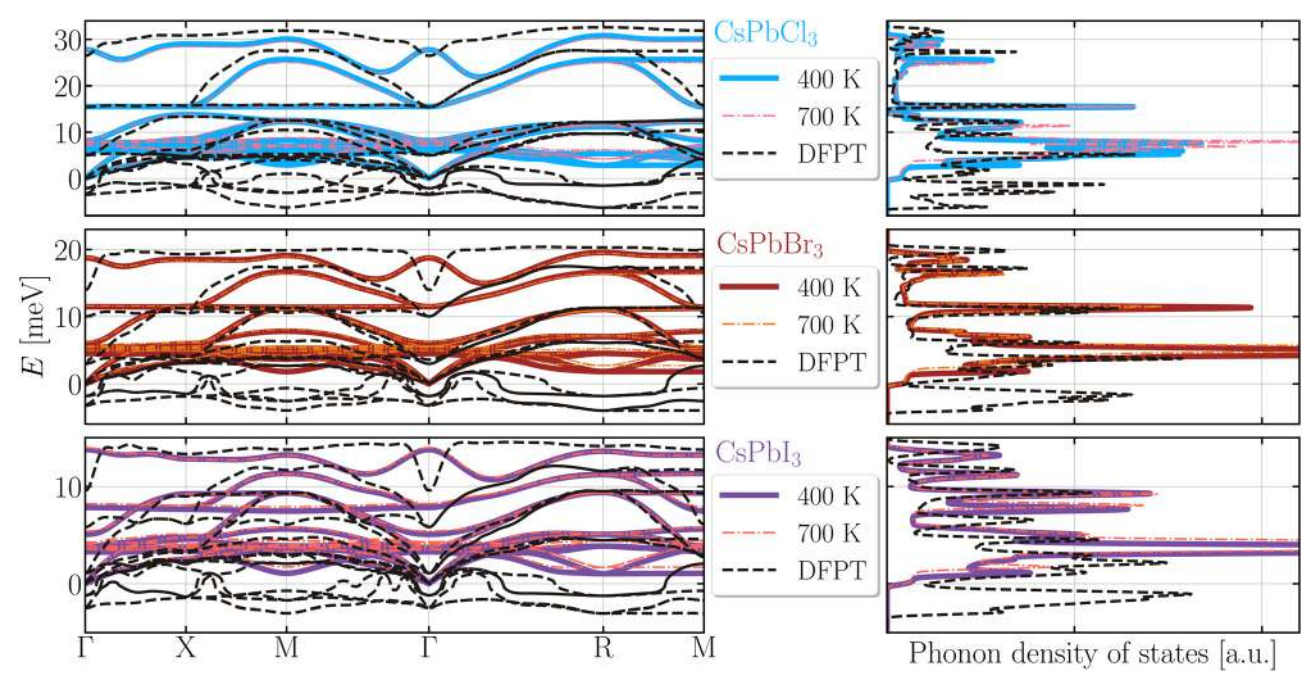


Fig. 2 Phonon dispersion (left column) and phonon density of states (in arbitrary units) for CsPbX<sub>3</sub> (X = Cl, Br or I, in rows from top to bottom) obtained using the SCPH method at T = 400 K (solid line) and T = 700 K (dot-dashed line), as well as using DFPT with harmonic approximation (dashed line).

point in the Brillouin zone. To understand whether the approach where imaginary phonon frequencies are discarded can provide reasonably good results, we performed the convergence tests with respect to  $N_q$  and  $\delta$  in three cases: (i) assuming phonon frequencies from DFPT and disregarding the contribution from phonons with imaginary frequencies; (ii) assuming phonon frequencies from DFPT and disregarding the contribution from the whole phonon bands that exhibit imaginary frequencies at any q-point; (iii) assuming phonon frequencies obtained from the SCPH method. These three cases will be referred to as cases (i), (ii) and (iii) in what follows.

In Fig. 3 we present the results for band gap renormalization obtained using the OTMS approach in each of these cases. We see that in case (i) the behavior with respect to  $N_q$  is not convergent and one obtains unphysically large band gap renormalizations. In this case several phonon bands cross zero energy at several different points in the Brillouin zone (see the left column in Fig. 2), which leads to divergence of Fan matrix elements due to the  $\omega_{q\nu}$  term in the denominator, see eqn (5). The convergence is better in case (ii) when such phonon bands are simply disregarded, however one obtains band gap renormalization which is underestimated with respect to case (iii). In case (iii), we obtain convergence with respect to  $\delta$  and  $N_q$ .

In Fig. 4 we decompose the CBM and VBM renormalization into contributions from phonons of different energies. Most of the contributions come from the region where the density of phonon states is the highest and these contributions come mostly from lower bands. Lower energy phonons also tend to have larger electron-phonon coupling matrix elements due to the  $\omega_{a\nu}$  term in the denominator in eqn (5). This fact also contributes to prevalent contribution of lower energy phonons to band energy renormalization. Since most of these lower energy phonons turn into imaginary frequency phonons within the DFPT calculation, the results obtained in case (ii) are underestimated in comparison to the results in case (iii). We also analyzed the contributions of the first order Fan and second order Debye-Waller terms in eqn (8) to band energy renormalization. In line with previous literature results for other materials, 29,78 we find that these two terms have opposite signs and that both of these terms have significant absolute values, see Fig. S22 in the ESI.† For these reasons, accurate calculation of each of these terms is necessary to obtain reliable final results for band energy renormalization.

Next, we discuss the linearity of the temperature dependence of the band gap renormalization. One can notice from eqn (8) [with self-energies given by eqn (6) and (7)] that the temperature dependence originates only from the Bose term in these equations. When phonon energies are small the temperature dependence of the Bose term is linear. As a consequence, the temperature dependence of band energy renormalization is also linear in case (ii), as can be seen in Fig. 4. On the other hand, in case (iii) the phonon frequencies also depend on temperature and the temperature dependence of the band gap is determined by the ratio of the Bose term (which contains temperature dependent phonon frequency) and the phonon frequency [which comes from the Fan matrix element, see eqn (5) and (6)]. The Bose term increases the gap with temperature as in case (ii), however, most of the temperature dependent frequencies (especially the ones where the density of phonon states is the largest) increase with temperature. They then tend to decrease the renormalization, which leads to nonlinear dependence in case (iii), as seen in Fig. 4.

Our final result for temperature dependence of the band gap of the investigated materials using the OTMS approach is among the results presented in Fig. 5. For the reasons

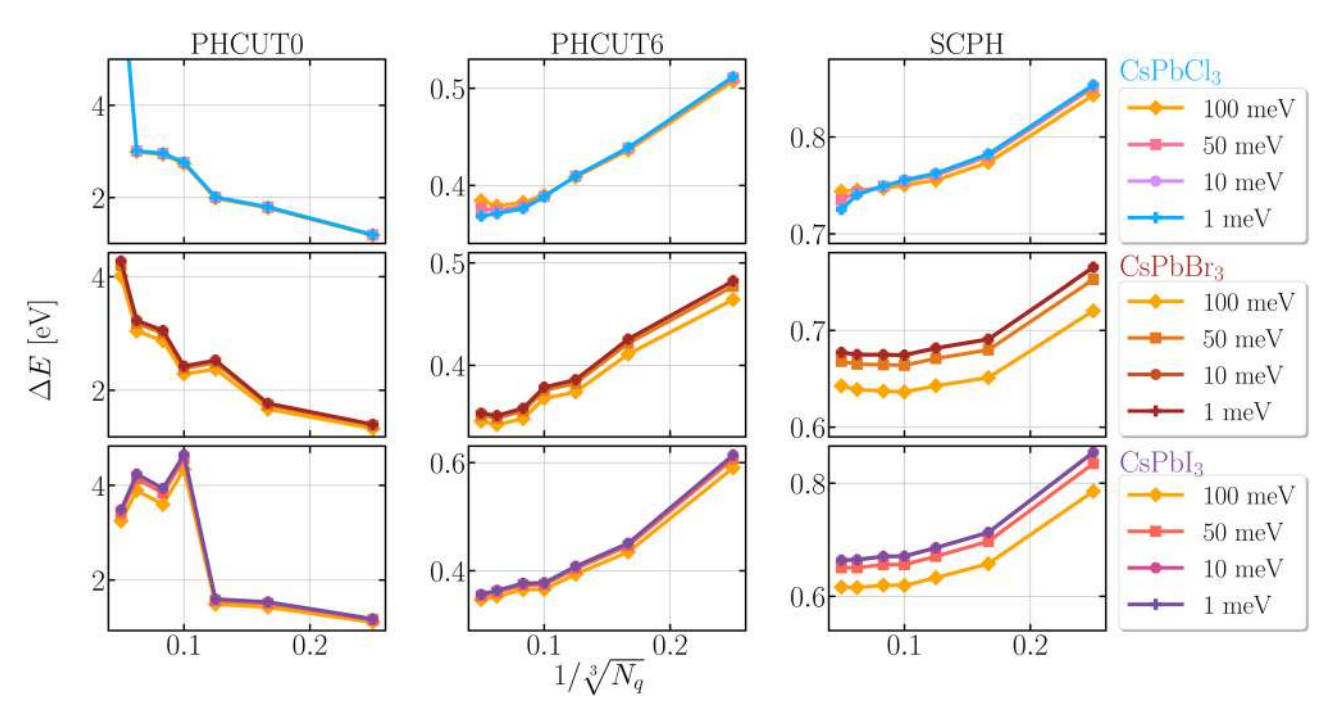


Fig. 3 Dependence of band gap renormalization obtained using the OTMS approach on the number of q-points  $N_q$  and on the small parameter  $\delta$ (whose value is specified in the legend) for CsPbX<sub>3</sub> (X = Cl, Br or I, in rows from top to bottom) materials at T = 400 K. The column labeled as PHCUT0 denotes the result obtained assuming phonon frequencies from DFPT and disregarding the contribution from phonons with imaginary frequencies [case (i) discussed in the text], while the column labeled as PHCUT6 denotes the results obtained assuming phonon frequencies from DFPT and disregarding the contribution from the whole bands that exhibit imaginary frequencies at any q-point [case (ii) in the text]. The column labeled as SCPH denotes the result obtained by taking phonon frequencies from the SCPH method [case (iii) in the text].

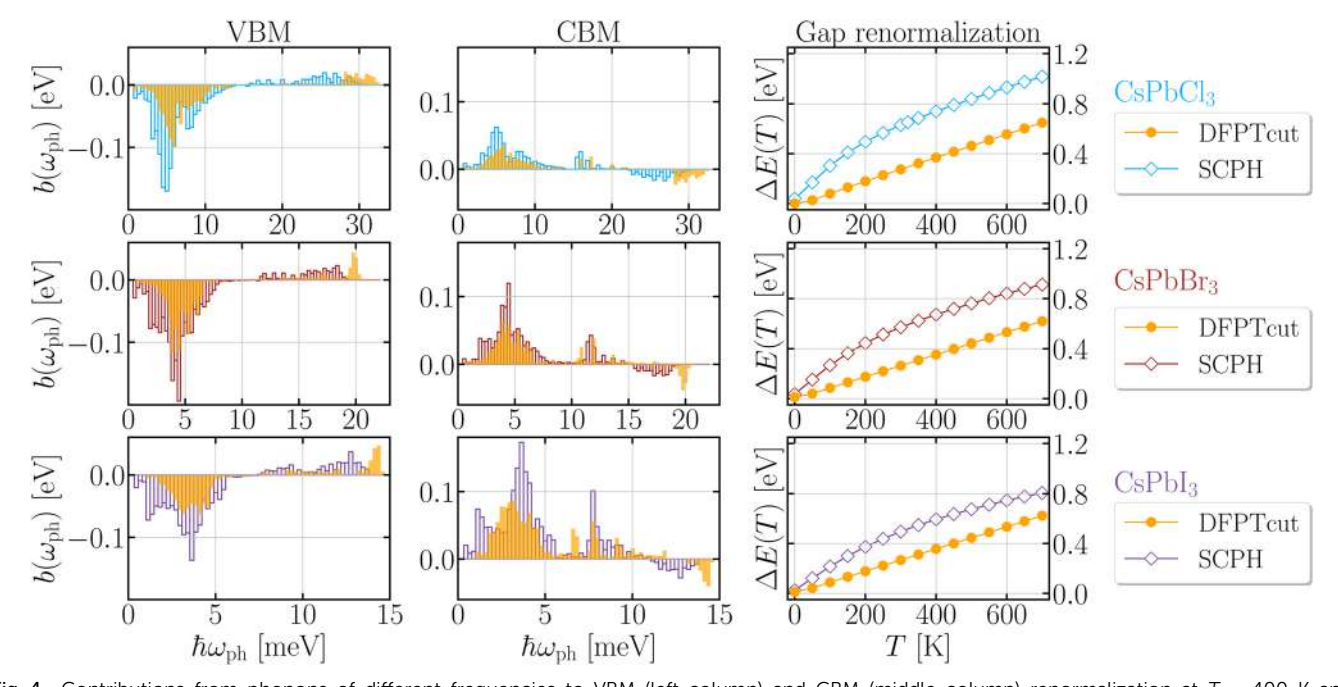


Fig. 4 Contributions from phonons of different frequencies to VBM (left column) and CBM (middle column) renormalization at T = 400 K and temperature dependent gap renormalization (right column) for  $CsPbX_3$  (X = Cl, Br or I, in rows from top to bottom) obtained using the OTMS approach. The results in case (ii) are shown as filled bins, while the results in case (iii) are shown as transparent bins. The value of each bin  $b(\omega_i)$  represents the contribution of all phonons with frequencies from the range  $(\omega_i - \Delta\omega/2, \omega_i + \Delta\omega/2)$  to band energy renormalization, so that  $\Delta E_{k\alpha} = \Sigma_i b(\omega_i)$ . Filled circles in the right column correspond to case (ii), while empty deltoids correspond to case (iii).

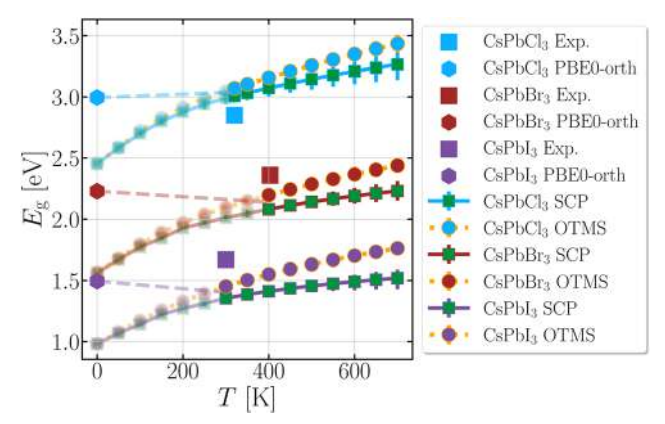


Fig. 5 Temperature dependence of the calculated band gap of CsPbX<sub>3</sub> materials (X = Cl, Br or I, from top to bottom). The calculated band gap of orthorhombic structures at zero temperature is represented by hexagons. while the band gaps of the cubic structure calculated using the SCP (OTMS) approach are represented by full (dotted) lines and two color squares (circles). Experimental results are represented by single color squares with the values of 2.85 eV (ref. 79), 2.36 eV (ref. 80), and 1.67 eV (ref. 81) respectively, at temperatures of 320 K, 403 K and 300 K, respectively, for CsPbCl<sub>3</sub>, CsPbBr<sub>3</sub> and CsPbl<sub>3</sub>, respectively. Dashed lines are used as a guide to the eye to connect the zero temperature result for the band gap of the orthorhombic structure with the result at the lowest temperature where the material exhibits a cubic structure.

previously discussed, these results and all subsequent results were obtained by taking the phonon frequencies obtained from the calculation based on the SCPH method. In all calculations reported in this and the next section renormalized band energies were obtained by adding the phonon-induced renormalization to the band energies calculated using the hybrid functional as described in Section 3.2. The results at temperatures lower than the temperatures where the cubic structure exists are blurred.

The OTMS approach can be used in principle to determine the renormalization of bands other than the CBM and the VBM. As discussed in the introduction and Section 2.1, band renormalization for other bands exhibits a slow linear convergence with respect to  $\delta$  when  $\delta \rightarrow 0$  in contrast to Lorentzian convergence of CBM and VBM. As a consequence, one has to go to rather small values of  $\delta$  to reach convergence. However, for small values of  $\delta$ , large values of  $N_a$  are needed, which introduces a large computational burden. We illustrate this behavior in Fig. S1, Fig. S9 and Fig. S14 in the ESI,† for the cases of CsPbCl<sub>3</sub>, CsPbBr<sub>3</sub>, and CsPbI<sub>3</sub>, respectively. For larger values of  $\delta$  (100 meV and 50 meV in the figure) good convergence with respect to  $N_a$  is achieved but the result still depends on  $\delta$  and one therefore needs to go to smaller  $\delta$  to achieve convergence with respect to  $\delta$ . However, for smaller values of  $\delta$  (10 meV and 1 meV), convergence with respect to  $N_q$  could not be achieved with grids up to 20  $\times$  20  $\times$  20. As also discussed in the introduction and Section 2.1, it is questionable whether the limit  $\delta \rightarrow 0$  of the energy level broadening parameter gives accurate results given the fact that the energy levels of higher bands can exhibit significant broadening. For all these reasons, it is more desirable to self-consistently determine the energy level broadening. These results are the subject of Section 3.6.

#### 3.6. Band energy renormalization calculations using the SCP approach

We now present the results for band energy renormalization obtained using the SCP approach. The frequency dependence of the self-energy and the spectral function for several bands at the R point in the case of the CsPbBr<sub>3</sub> material at T = 400 K is presented in Fig. 6 (the same results for CsPbCl<sub>3</sub> and CsPbI<sub>3</sub> are presented respectively in Fig. S4 and S17 in the ESI†). We denote the bands in ascending order of energies at the R point as VBM4  $(2\times)$ , VBM3  $(4\times)$ , VBM2  $(2\times)$ , VBM1  $(4\times)$ , VBM  $(2\times)$ , CBM  $(2\times)$ , CBM1 (4 $\times$ ), CBM2 (2 $\times$ ), CBM3 (2 $\times$ ), and CBM4 (4 $\times$ ), where the numbers in brackets denote their degeneracy. The spectral functions of the CBM and VBM are relatively narrow and symmetric, while the spectral functions of other bands (CBM1 and VBM1 in Fig. 6 and CBM2-4 and VBM2-4 in Fig. S10 and S12 in the ESI† in the case of CsPbBr<sub>3</sub>, see also Fig. S2, S4 and S6 (ESI†) for CsPbCl<sub>3</sub>, as well as Fig. S15, S17 and S19 (ESI†) for the CsPbI<sub>3</sub> material) are wider and somewhat asymmetric. This result confirms that it was necessary to go beyond the OTMS approach in the  $\delta \to 0$  limit to obtain accurate results for bands other than the CBM and VBM. There is even a difference between the OTMS and SCP result for CBM and VBM which leads to a band gap difference between the two approaches on the order of 100 meV at T = 400 K (see Section 3.7 for more details).

In Fig. 7 we demonstrate that convergence with respect to  $N_a$ was achieved with a  $20 \times 20 \times 20$  grid. Convergence is achieved both for the real part of self-energy that corresponds to band energy renormalization and for the imaginary part of the selfenergy that is related to energy level broadening. As expected, it is easier to reach convergence for energy levels that exhibit larger broadening, that is, for states other than the CBM and VBM (Fig. 7 and Fig. S11 and S13 in the ESI,† see also Fig. S3, S5 and S7 (ESI†) for the CsPbCl<sub>3</sub> material, as well as Fig. S16, S18 and S20 (ESI†) for the CsPbI3 material). The CBM and VBM states exhibit the lowest broadening due to the fact that single phonon emission processes from these states are not possible. Hence the total scattering rate from these states, which is related to energy level broadening, is determined by phonon absorption processes only. On the other hand, for bands higher than the CBM (lower than the VBM), there is always a nearby other band below (above) it to which phonon emission is also possible. Hence, these states exhibit higher electron-phonon scattering rates than the CBM and VBM, which leads to larger broadening of these states.

The final results for temperature dependence of band energies and the imaginary part of self-energies (that are related to energy level broadening) at the R point for the CsPbBr3 material are presented in Fig. 8. The same results for CsPbCl<sub>3</sub> and CsPbI<sub>3</sub> are presented in Fig. S8 and S21, respectively, in the ESI.† The results indicate that the temperature dependence of band energies is most pronounced for the CBM and the VBM and that it is much weaker for the other bands. The energy level broadenings increase as the temperature increases and this dependence is nearly linear for most bands.

The temperature dependence of the band gap calculated within the SCP approach is presented in Fig. 5. The results

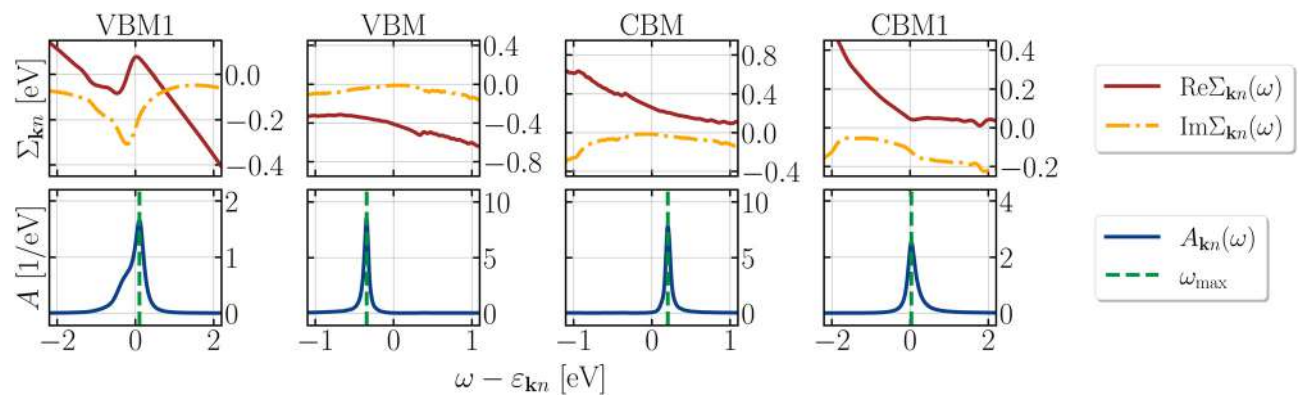


Fig. 6 The frequency dependence of the self-energy and the spectral function for bands VBM1, VBM, CBM and CBM1 at the R point in the case of the CsPbBr<sub>3</sub> material at T = 400 K.

suggest that the gap renormalization and the band gap are somewhat smaller in the SCP approach than in the case of the OTMS approach. The largest difference between the two approaches is at the highest temperatures. This difference originates from the fact that the spectral function within the SCP approach takes a relatively broad asymmetric shape at these temperatures, while the OTMS approach inherently assumes a narrow symmetric Lorentzian spectral function. A comparison of the temperature dependence of the band gap within the SCP approach with experiments will be discussed in Section 3.7.

To gain insight into the effect of temperature on band energies throughout the Brillouin zone, we also performed SCP calculations of the spectral function and band energy renormalization at points  $\Gamma$ , X and M in the Brillouin zone for the three investigated materials. The results are presented in Fig. S23–S85 in the ESI.† All energy levels at X and M points are twofold degenerate, while the degeneracy of the bands at  $\Gamma$ is as follows: VBM4 (4 $\times$ ), VBM3 (2 $\times$ ), VBM2 (4 $\times$ ), VBM1 (2 $\times$ ), VBM  $(4\times)$ , CBM  $(2\times)$ , CBM1  $(4\times)$ , CBM2  $(2\times)$ , CBM3  $(2\times)$ , and CBM4  $(4\times)$ . We can see (Fig. S29, S36, S43, S50, S57, S64, S71, S78, and S85 in the ESI†) that in most cases the real and the imaginary part of the self-energy are smooth and continuous when the temperature changes. The exceptions are VBM2 for  $CsPbCl_3$  between T = 50 K and T = 100 K, and VBM1 for  $CsPbBr_3$ 

and CsPbI<sub>3</sub> between T = 550 K and T = 600 K, all three at the X point (Fig. S50, S57, and S64 in the ESI,† respectively). In these cases, the spectral function has two competing maxima (see Fig. S87-S89 in the ESI†) that are well inside the range of its half-width and the change in temperature changes the dominant maximum. It should be noted that for all of the examined points, the changes in state energies are such that the band gap remains determined by the R point VBM and CBM. However, an increase in the temperature can change the ordering of the bands: at certain points in the Brillouin zone some neighbouring bands below (above) the VBM1 (CBM1) will swap places with respect to their order obtained from the PBE0 functional calculations. Nevertheless, for simplicity, we label the bands based on their ordering obtained from zero temperature PBE0 functional calculations. When it comes to energy level broadening, it turns out that it is lowest for the VBM and CBM bands (with the imaginary part of the self-energy well below 100 meV for these states and significantly above 100 meV for the other states), as in the case of the R point. The CBM and VBM states at these points are well separated in energy from the other bands (see the material band structures in Fig. S86 in the ESI†) which restricts the phase space for electron scattering. The exception to this behaviour is the VBM state at the  $\Gamma$  point which is rather broad. In this case, there are several bands that

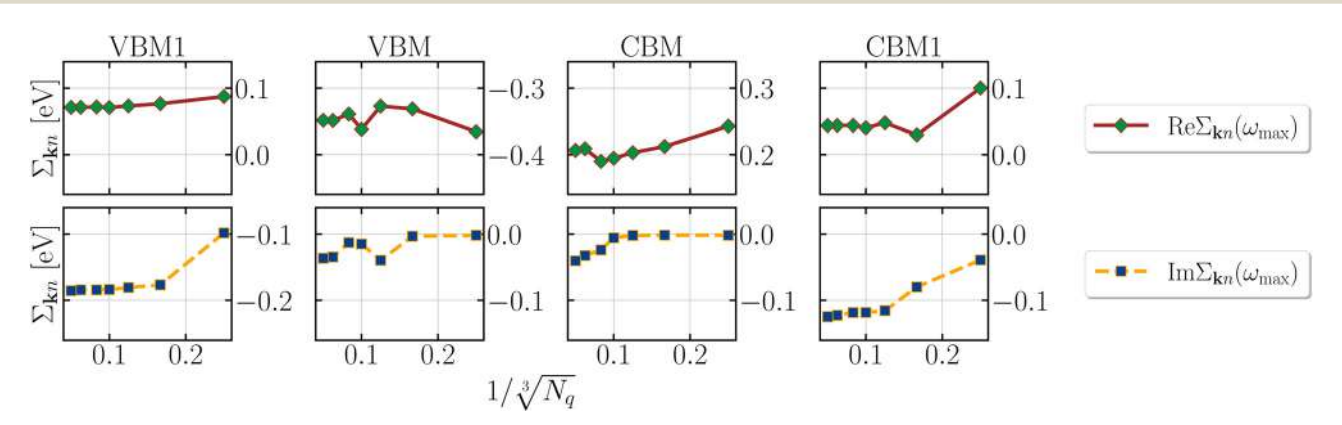


Fig. 7 The dependence of the real and imaginary part of self-energy at the renormalized energy on the size of the q-points grid. The results are presented for the CsPbBr<sub>3</sub> material at T = 400 K for bands VBM1, VBM, CBM and CBM1 at the R point.

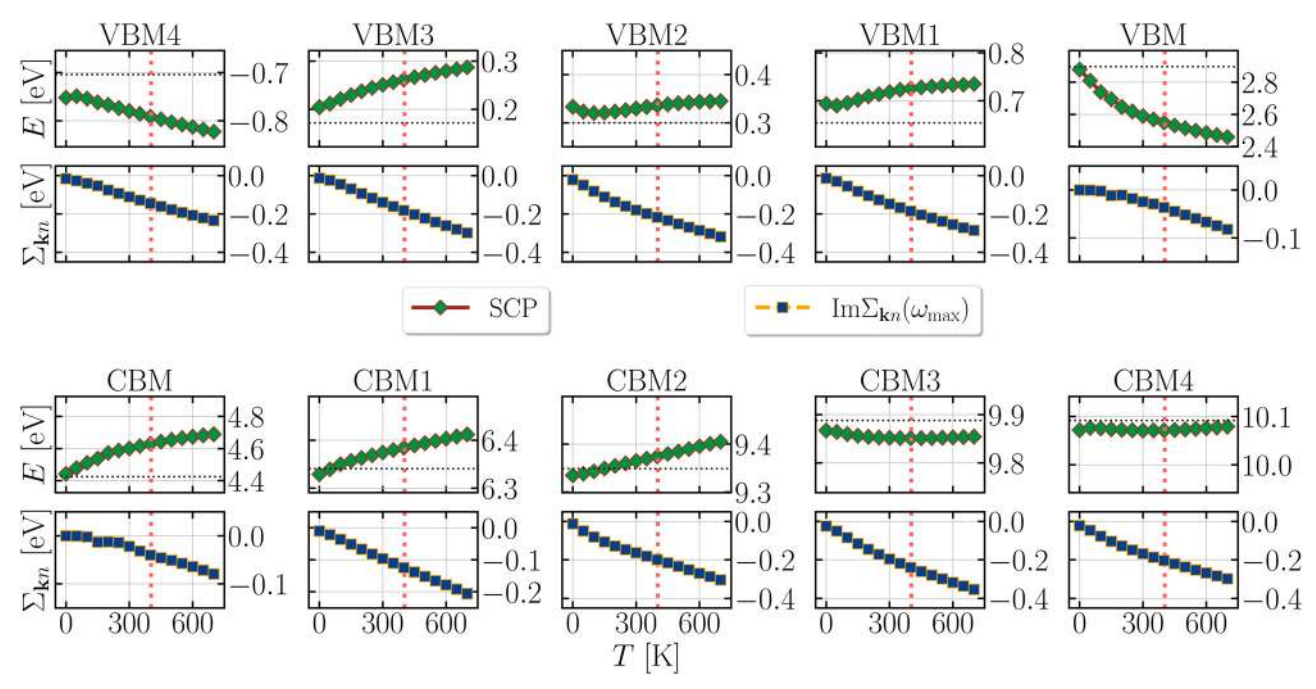


Fig. 8 Temperature dependence of the band energy and the imaginary part of the self-energy for VBM and VBMx (CBM and CBMx) bands (where x = 1, 2, 3, 4) calculated using the SCP approach. The results are shown for CsPbBr<sub>3</sub> at the R point. Vertical and horizontal dotted lines represent the temperature of the phase transition to cubic structure  $T_c = 403$  K and band energy from PBEO calculations, respectively.

are close in energy to the VBM state at  $\Gamma$ . The hole can scatter to these bands which contributes to the increase of energy level broadening.

#### 3.7. Comparison of temperature dependence of the band gap with experiments

In this section, we compare the results for the band gap and its temperature dependence with available experimental results from the literature.

In the case of CsPbBr<sub>3</sub> we obtain the band gap of 2.08 eV and 2.20 eV from SCP and OTMS, respectively, at a temperature of 400 K. This result is close to the experimental value of 2.36 eV from ref. 80, obtained at 403 K. Our calculation gives the band gap of CsPbCl<sub>3</sub> of 3.01 eV and 3.07 eV from SCP and OTMS, respectively, at a temperature of 320 K. This result is in good agreement with experimental value of 2.85 eV from ref. 79. For the CsPbI<sub>3</sub> material we obtain the band gaps of 1.35 eV and 1.45 eV from SCP and OTMS, respectively, at a temperature of 300 K, which is in reasonable agreement with experimental values of 1.67 eV (ref. 81) and 1.73 eV (ref. 82).

Next, we discuss the slope of the temperature dependence of the band gap. In the range of temperatures where the material is in the cubic form, the calculated temperature dependence is nearly linear. Therefore, for the purpose of comparison with experiments, it is sufficient to discuss its slope. In the case of

CsPbBr3, we obtain the slope 
$$\left(\frac{\mathrm{d}E_\mathrm{g}}{\mathrm{d}T}\right)_\mathrm{ph}$$
 of 0.50 meV  $\mathrm{K}^{-1}$  and

0.80 meV K<sup>-1</sup> from SCP and OTMS, respectively, in the temperature range from 400 K to 700 K. For CsPbCl<sub>3</sub>, the calculation yields the slope of 0.68 meV K<sup>-1</sup> and 0.96 meV K<sup>-1</sup> from SCP and

OTMS, respectively, in the temperature range from 320 K to 700 K. Finally, for CsPbI<sub>3</sub> we obtain the slope  $\left(\frac{dE_g}{dT}\right)_{ph}$  of 0.41 meV K<sup>-1</sup> and 0.77 meV K<sup>-1</sup> from SCP and OTMS, respectively, in the temperature range from 300 K to 700 K.

To compare the slope of the temperature dependence to experiments, one also has to take into account the effect of thermal expansion, which is not included in the calculation with a fixed lattice constant. The slope of the temperature dependence of the band gap from the effect of thermal expansion is given as

$$\left(\frac{\mathrm{d}E_{\mathrm{g}}}{\mathrm{d}T}\right)_{\mathrm{TE}} = \left(\frac{\mathrm{d}E_{\mathrm{g}}}{\mathrm{d}a}\right) \left(\frac{\mathrm{d}a}{\mathrm{d}T}\right),\tag{13}$$

where  $\frac{dE_g}{da}$  is the slope of the dependence of the band gap on the lattice constant and  $\frac{da}{dT}$  is the slope of the temperature

dependence of the lattice constant, which is related to linear thermal expansion coefficient as

$$\alpha = \frac{1}{a} \frac{\mathrm{d}a}{\mathrm{d}T}.\tag{14}$$

We estimate  $\frac{\mathrm{d}E_{\mathrm{g}}}{\mathrm{d}a}$  by calculating the gap dependence of the lattice constant using DFT with the same semilocal functional used in Section 3.1. We obtain respectively the values of 2.1, 2.4 and 1.1 eV  $\mathring{A}^{-1}$  for CsPbBr3, CsPbCl3 and CsPbI3. Literature values of linear thermal expansion coefficients are respectively  $0.26 \times 10^{-4} \text{ K}^{-1}$ ,  $(0.22-0.30) \times 10^{-4} \text{ K}^{-1}$  and  $(0.39-0.40) \times$  $10^{-4}$  K<sup>-1</sup> for CsPbBr<sub>3</sub>, CsPbCl<sub>3</sub> and CsPbI<sub>3</sub> (ref. 83). From eqn (13) and (14) we then obtain that  $(dE_g/dT)_{TE}$  is respectively

equal to 0.32 meV  $\rm K^{-1}$ , 0.35 meV  $\rm K^{-1}$  and 0.29 meV  $\rm K^{-1}$  for CsPbBr<sub>3</sub>, CsPbCl<sub>3</sub> and CsPbI<sub>3</sub>. The results suggest that the contribution from thermal expansion is smaller than the contribution from phonon-induced band gap renormalization for all the materials studied.

The total slope of the temperature dependence of the band gap can be estimated by adding contributions from phononinduced band gap renormalization and from thermal expansion

$$\frac{\mathrm{d}E_g}{\mathrm{d}T} = \left(\frac{\mathrm{d}E_g}{\mathrm{d}T}\right)_{\mathrm{TE}} + \left(\frac{\mathrm{d}E_g}{\mathrm{d}T}\right)_{\mathrm{ph}}.$$
 (15)

We then obtain  $\frac{\mathrm{d}E_g}{\mathrm{d}T}$  of 0.81 meV K<sup>-1</sup> (1.12 meV K<sup>-1</sup>), 1.02 meV K<sup>-1</sup> (1.31 meV K<sup>-1</sup>), and 0.70 meV K<sup>-1</sup> (1.06 meV K<sup>-1</sup>) from SCP (OTMS) results, respectively, for CsPbBr<sub>3</sub>, CsPbCl<sub>3</sub> and CsPbI<sub>3</sub>.

Experimental data for the temperature dependence of the band gap of the cubic structure and its slope are relatively scarce. In ref. 84 the slope of (0.85  $\pm$  0.05) meV K<sup>-1</sup> was reported for CsPbI3 based on the measurements in the temperature range from 570 K to 620 K. This value is in the range between our results from SCP and OTMS for the same material. The slope of 0.341 meV K<sup>-1</sup> was reported for CsPbBr<sub>3</sub> in ref. 27 in the temperature range from 380 K to 435 K where the material exhibits a phase transition from tetragonal to cubic structure. This slope is significantly smaller than our estimated slope. It is however questionable if the comparison of these slopes is meaningful given the fact that experimental data cover only a very small initial part of the temperature range where the material is cubic. For the CsPbCl<sub>3</sub> material, we are not aware of any literature data with temperature dependence of the band gap in the cubic phase. Overall, further experimental measurements of the temperature dependence of the band gap in a broader temperature range in the cubic phase are certainly desirable.

Finally, we briefly discuss the temperature dependence of the band gap at lower temperatures when the materials exhibit an orthorhombic or a tetragonal structure. Experimental results at these temperatures generally indicate that temperature dependence of the band gap is rather weak. For example, it was reported in ref. 70 that the band gap of CsPbBr<sub>3</sub> (CsPbI<sub>3</sub>) increases by about 60 meV (80 meV) from 0 K to 300 K. In ref. 79 a similar result was obtained for CsPbBr<sub>3</sub>, while in the case of CsPbCl<sub>3</sub> the changes in the band gap in this temperature range were smaller than 20 meV. In ref. 85-87, a comparably weak temperature dependence of the gap was observed for nanocrystals based on CsPbX3 materials in the same temperature range. For all three materials, the band gap at zero temperature is only slightly (by less than 100 meV) lower or even slightly larger than at the lowest temperature where the materials exhibit a cubic structure, see the reference to the values of experimental band gaps at the end of Section 3.2 for the orthorhombic structure and the beginning of this section for the cubic structure. Our calculations of the band gap of the orthorhombic structure at zero temperature and of the cubic structure are in line with such behavior (see the dashed lines in Fig. 5). Since the orthorhombic and tetragonal structure have a larger unit cell than the cubic structure, we did not perform temperature dependent electronic structure calculations of these structures due to larger computational cost and the fact that experimental results indicate a rather weak temperature dependence in this range of temperatures.

#### 4 Discussion and conclusions

Next, we discuss previous computational studies where the effects of temperature on the electronic structure of halide perovskites were investigated. In ref. 23, the effects of temperature were included by performing finite temperature ab-initio molecular dynamics with a sufficiently large supercell and by calculating the average band gap change from many molecular dynamics snapshots. Excellent agreement with experimental band gaps of cubic inorganic halide perovskites at the lowest temperature where the material exhibits a cubic structure was obtained. On the computational side, this approach is rather demanding as it would require a separate molecular dynamics simulation at each temperature to obtain the temperature dependence of the band gap. This approach inherently assumes classical phonons which is likely good approximation at room temperature because the dominant phonon modes that determine electronic structure renormalization have energies which are significantly smaller than thermal energy  $k_{\rm B}T$  at room temperature. In ref. 45 and 88 the effects of temperature were also included by taking an average over many different configurations with atoms displaced from their equilibrium positions. In ref. 24 and 25 the authors exploited the special displacements method89,90 which enables calculation of the band gap at a given temperature from a single calculation of a large supercell with atoms displaced from their equilibrium positions in accordance with a particular pattern. In ref. 22, Allen-Heine-Cardona theory, the finite difference approach, as well as the approach with an average over many different atomic configurations sampled using a Monte Carlo approach were used to study the temperature dependence of the band gap of cubic methylammonium lead iodide perovskite. However, the Allen-Heine-Cardona theory was applied by simply excluding imaginary phonon modes, while we find that this procedure does not give reliable results in the case of the inorganic halide perovskites that we investigated.

We finally note several advantages, as well as shortcomings, of the approach based on the Allen–Heine–Cardona theory over other approaches. To obtain temperature dependence of the electronic structure, the most demanding steps of the procedure – DFPT calculations and extraction of force constants for application of the SCPH method – need to be performed only once, that is, they do not have to be repeated for each temperature. On the other hand, in all approaches based on atomic displacements (sampled either from molecular dynamics, Monte Carlo or using the special displacements) the whole computational procedure has to be repeated at each temperature. Within the Allen–Heine–Cardona approach it is straightforward to obtain

renormalization of states other than the CBM or VBM, while in the methods based on supercell calculations this is either impossible or one has to exploit a certain type of unfolding procedure, such as the one used in ref. 89. It should be mentioned that the approach based on the Allen-Heine-Cardona theory certainly has its limitations. Being based on expansion up to second order terms with respect to atomic displacements, it is not expected to be highly accurate in conditions when this expansion is not sufficient. On the other hand, the approaches based on atomic displacements usually do not have such a limitation.

In conclusion, we performed ab-initio calculations of the temperature dependent electronic structure of inorganic halide perovskite materials CsPbX<sub>3</sub>. The challenge that comes from the fact that cubic structure is not stable at zero temperature and that one obtains phonon modes with imaginary frequencies in a standard DFPT calculation was overcome by using the SCPH method that gives the phonon spectrum with real non-negative frequencies. The challenge of obtaining the energies of bands other than the CBM and the VBM in the calculations based on the Allen-Heine-Cardona theory was addressed by exploiting a selfconsistent procedure for evaluation of relevant self-energies and spectral functions. We obtain the band gaps at the lowest temperature where the materials exhibit a cubic structure in good agreement with experiments. We also find good agreement of calculated and experimental temperature dependence of the band gap for the CsPbI<sub>3</sub> material where reliable experimental data are available in the literature. Our results also suggest that the band gaps at the lowest temperature where the materials exhibit a cubic structure are similar to the band gaps at zero temperature where the materials exhibit an orthorhombic structure. This finding is consistent with experimental data that suggest a rather weak temperature dependence at lower temperatures where the materials exhibit an orthorhombic or a tetragonal structure. Finally, we find that the temperature dependence of band energies at the Rpoint is most pronounced for the CBM and the VBM, while it is less pronounced for higher and lower bands.

#### Conflicts of interest

There are no conflicts of interest to declare.

#### Acknowledgements

We acknowledge funding provided by the Institute of Physics Belgrade, through the grant by the Ministry of Science, Technological Development and Innovation of the Republic of Serbia. Numerical computations were performed on the PARADOX-IV supercomputing facility at the Scientific Computing Laboratory, National Center of Excellence for the Study of Complex Systems, Institute of Physics Belgrade.

#### References

1 M. M. Lee, J. Teuscher, T. Miyasaka, T. N. Murakami and H. J. Snaith, Science, 2012, 338, 643-647.

- 2 M. Liu, M. B. Johnston and H. J. Snaith, Nature, 2013, 501, 395-398.
- 3 A. K. Jena, A. Kulkarni and T. Miyasaka, Chem. Rev., 2019, **119**, 3036-3103.
- 4 M. Aldamasy, Z. Iqbal, G. Li, J. Pascual, F. Alharthi, A. Abate and M. Li, Phys. Chem. Chem. Phys., 2021, 23, 23413-23427.
- 5 L. Lei, Q. Dong, K. Gundogdu and F. So, Adv. Funct. Mater., 2021, 31, 2010144.
- 6 X.-K. Liu, W. Xu, S. Bai, Y. Jin, J. Wang, R. H. Friend and F. Gao, Nat. Mater., 2021, 20, 10-21.
- 7 K. Xing, S. Cao, X. Yuan, R. Zeng, H. Li, B. Zou and J. Zhao, Phys. Chem. Chem. Phys., 2021, 23, 17113-17128.
- 8 M. Ahmadi, T. Wu and B. Hu, Adv. Mater., 2017, 29, 1605242.
- 9 T. M. H. Nguyen, S. Kim and C. W. Bark, J. Mater. Chem. A, 2021, 9, 1269-1276.
- 10 H. Wei and J. Huang, Nat. Commun., 2019, 10, 1066.
- 11 S. Svanström, A. García Fernández, T. Sloboda, T. J. Jacobsson, H. Rensmo and U. B. Cappel, Phys. Chem. Chem. Phys., 2021, 23, 12479-12489.
- 12 H. Xie, S. Hao, J. Bao, T. J. Slade, G. J. Snyder, C. Wolverton and M. G. Kanatzidis, J. Am. Chem. Soc., 2020, 142, 9553-9563
- 13 X. Liu, J. Qiu, Q. Huang, X. Chen, J. Yu and J. Bao, Phys. Chem. Chem. Phys., 2023, 25, 11620-11629.
- 14 L. D. Whalley, J. M. Frost, Y.-K. Jung and A. Walsh, J. Chem. Phys., 2017, 146, 220901.
- 15 W.-J. Yin, J.-H. Yang, J. Kand, Y. Yan and S.-H. Wei, J. Mater. Chem. A, 2015, 3, 8926-8942.
- 16 J. Even, L. Pedesseau, C. Katan, M. Kepenekian, J.-S. Lauret, D. Sapori and E. Deleporte, J. Phys. Chem. C, 2015, 119, 10161-10177.
- 17 F. Brivio, K. T. Butler, A. Walsh and M. van Schilfgaarde, Phys. Rev. B: Condens. Matter Mater. Phys., 2014, 89, 155204.
- 18 A. Amat, E. Mosconi, E. Ronca, C. Quarti, P. Umari, M. K. Nazeeruddin, M. Grätzel and F. De Angelis, Nano Lett., 2014, 14, 3608-3616.
- 19 P. Umari, E. Mosconi and F. De Angelis, Sci. Rep., 2014, 4, 4467.
- 20 M. H. Du, J. Mater. Chem. A, 2014, 2, 9091-9098.
- 21 J. Feng and B. Xiao, J. Phys. Chem. Lett., 2014, 5, 1278–1282.
- 22 W. A. Saidi, S. Poncé and B. Monserrat, J. Phys. Chem. Lett., 2016, 7, 5247-5252.
- 23 J. Wiktor, U. Rothlisberger and A. Pasquarello, J. Phys. Chem. Lett., 2017, 8, 5507-5512.
- 24 H. Wang, A. Tal, T. Bischoff, P. Gono and A. Pasquarello, npj Comput. Mater., 2022, 8, 237.
- 25 J. Ning, L. Zheng, W. Lei, S. Wang, J. Xi and J. Yang, Phys. Chem. Chem. Phys., 2022, 24, 16003-16010.
- 26 A. Francisco-López, B. Charles, O. J. Weber, M. I. Alonso, M. Garriga, M. Campoy-Quiles, M. T. Weller and A. R. Goñi, J. Phys. Chem. Lett., 2019, 10, 2971-2977.
- 27 G. Mannino, I. Deretzis, E. Smecca, A. La Magna, A. Alberti, D. Ceratti and D. Cahen, J. Phys. Chem. Lett., 2020, 11, 2490-2496.
- 28 M. Mladenovic and N. Vukmirovic, Phys. Chem. Chem. Phys., 2018, 20, 25693-25700.

- 29 P. B. Allen and V. Heine, *J. Phys. C: Solid State Phys.*, 1976, **9**, 2305–2312.
- 30 P. B. Allen and M. Cardona, *Phys. Rev. B: Condens. Matter Mater. Phys.*, 1981, 23, 1495-1505.
- 31 P. B. Allen and M. Cardona, *Phys. Rev. B: Condens. Matter Mater. Phys.*, 1983, 27, 4760-4769.
- 32 S. Poncé, Y. Gillet, J. Laflamme Janssen, A. Marini, M. Verstraete and X. Gonze, *J. Chem. Phys.*, 2015, 143, 102813.
- 33 J. Park, W. A. Saidi, B. Chorpening and Y. Duan, *J. Phys. Chem. C*, 2021, **125**, 22231–22238.
- 34 F. Giustino, S. G. Louie and M. L. Cohen, *Phys. Rev. Lett.*, 2010, **105**, 265501.
- 35 A. Miglio, V. Brousseau-Couture, E. Godbout, G. Antonius, Y.-H. Chan, S. G. Louie, M. Côté, M. Giantomassi and X. Gonze, *npj Comput. Mater.*, 2020, **6**, 167.
- 36 R. D. King-Smith, R. J. Needs, V. Heine and M. J. Hodgson, *EPL*, 1989, **10**, 569–574.
- 37 S. Hirotsu, J. Harada, M. Iizumi and K. Gesi, J. Phys. Soc. Jpn., 1974, 37, 1393–1398.
- 38 S. Plesko, R. Kind and J. Roos, *J. Phys. Soc. Jpn.*, 1978, **45**, 553–557.
- 39 A. Marronnier, G. Roma, S. Boyer-Richard, L. Pedesseau, J.-M. Jancu, Y. Bonnassieux, C. Katan, C. C. Stoumpos, M. G. Kanatzidis and J. Even, ACS Nano, 2018, 12, 3477–3486.
- 40 R. X. Yang, J. M. Skelton, E. L. da Silva, J. M. Frost and A. Walsh, J. Phys. Chem. Lett., 2017, 8, 4720–4726.
- 41 D. Trots and S. Myagkota, J. Phys. Chem. Solids, 2008, 69, 2520-2526.
- 42 C. K. Møller, Nature, 1958, 182, 1436.
- 43 X. Zhou and Z. Zhang, AIP Adv., 2020, 10, 125015.
- 44 T. Tadano and W. A. Saidi, *Phys. Rev. Lett.*, 2022, 129, 185901.
- 45 C. E. Patrick, K. W. Jacobsen and K. S. Thygesen, *Phys. Rev. B: Condens. Matter Mater. Phys.*, 2015, **92**, 201205.
- 46 M. El Kurdi, G. Fishman, S. Sauvage and P. Boucaud, J. Appl. Phys., 2010, 107, 013710.
- 47 S. Boyer-Richard, F. Raouafi, A. Bondi, L. Pédesseau, C. Katan, J.-M. Jancu and J. Even, *Appl. Phys. Lett.*, 2011, 98, 251913.
- 48 Z. Song, W. Fan, C. S. Tan, Q. Wang, D. Nam, D. H. Zhang and G. Sun, *New J. Phys.*, 2019, **21**, 073037.
- 49 M. Jocic and N. Vukmirovic, Phys. Rev. B, 2020, 102, 085121.
- 50 F. Giustino, Rev. Mod. Phys., 2017, 89, 015003.
- 51 E. Cannuccia and A. Marini, Eur. Phys. J. B, 2012, 85, 320.
- 52 P. Mitric, V. Jankovic, N. Vukmirovic and D. Tanaskovic, *Phys. Rev. B*, 2023, **107**, 125165.
- 53 T. Tadano and S. Tsuneyuki, *Phys. Rev. B: Condens. Matter Mater. Phys.*, 2015, **92**, 054301.
- 54 J. P. Perdew, A. Ruzsinszky, G. I. Csonka, O. A. Vydrov, G. E. Scuseria, L. A. Constantin, X. Zhou and K. Burke, *Phys. Rev. Lett.*, 2008, **100**, 136406.
- 55 J. P. Perdew, K. Burke and M. Ernzerhof, *Phys. Rev. Lett.*, 1996, 77, 3865–3868.
- 56 P. Giannozzi, S. Baroni, N. Bonini, M. Calandra, R. Car, C. Cavazzoni, D. Ceresoli, G. L. Chiarotti, M. Cococcioni,

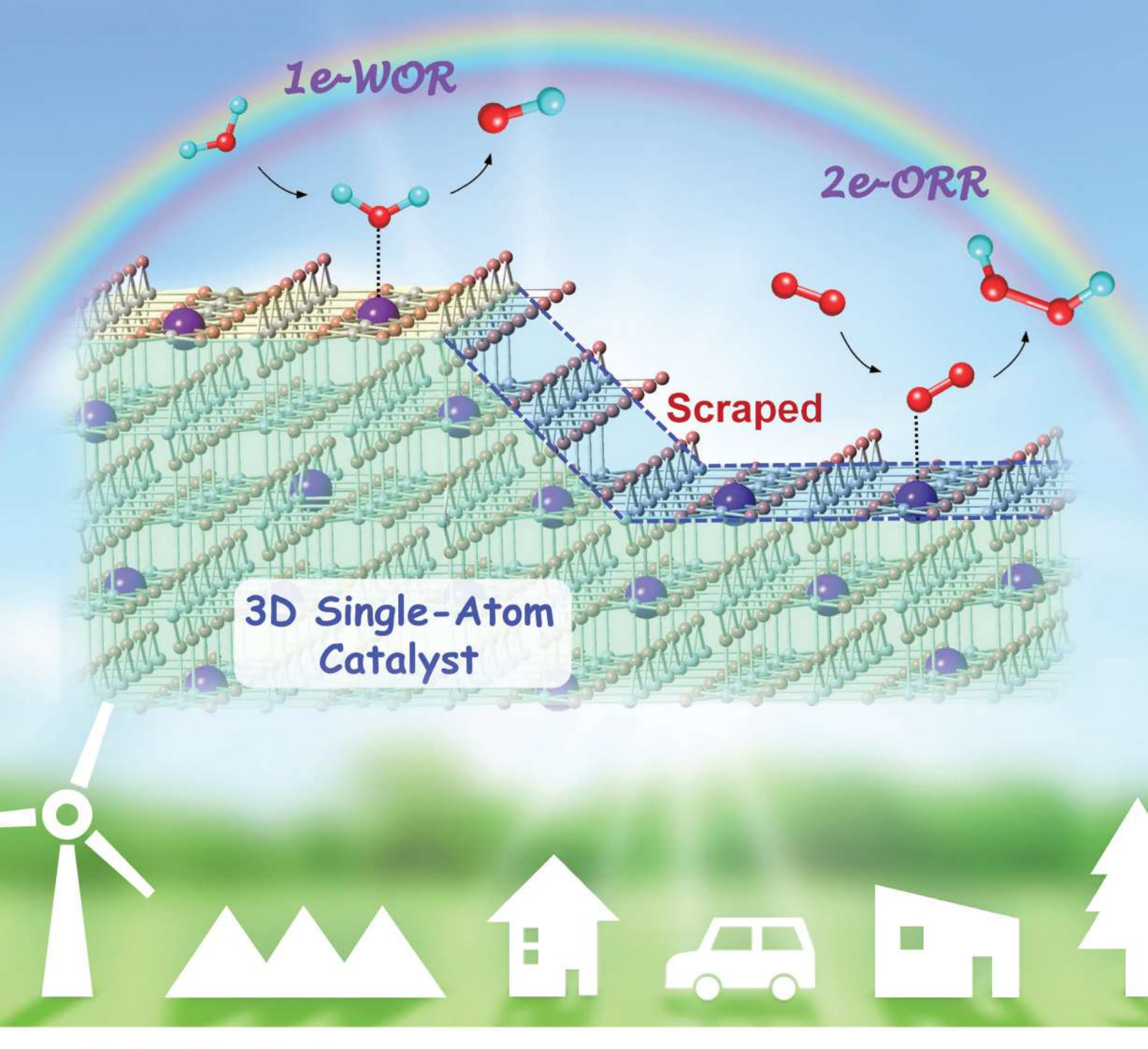
- I. Dabo, A. D. Corso, S. de Gironcoli, S. Fabris, G. Fratesi, R. Gebauer, U. Gerstmann, C. Gougoussis, A. Kokalj, M. Lazzeri, L. Martin-Samos, N. Marzari, F. Mauri, R. Mazzarello, S. Paolini, A. Pasquarello, L. Paulatto, C. Sbraccia, S. Scandolo, G. Sclauzero, A. P. Seitsonen, A. Smogunov, P. Umari and R. M. Wentzcovitch, *J. Phys.: Condens.Matter*, 2009, 21, 395502.
- 57 P. Giannozzi, O. Andreussi, T. Brumme, O. Bunau, M. B. Nardelli, M. Calandra, R. Car, C. Cavazzoni, D. Ceresoli, M. Cococcioni, N. Colonna, I. Carnimeo, A. D. Corso, S. de Gironcoli, P. Delugas, R. A. DiStasio, A. Ferretti, A. Floris, G. Fratesi, G. Fugallo, R. Gebauer, U. Gerstmann, F. Giustino, T. Gorni, J. Jia, M. Kawamura, H.-Y. Ko, A. Kokalj, E. Küçükbenli, M. Lazzeri, M. Marsili, N. Marzari, F. Mauri, N. L. Nguyen, H.-V. Nguyen, A. O. De-la Roza, L. Paulatto, S. Poncé, D. Rocca, R. Sabatini, B. Santra, M. Schlipf, A. P. Seitsonen, A. Smogunov, I. Timrov, T. Thonhauser, P. Umari, N. Vast, X. Wu and S. Baroni, J. Phys.: Condens. Matter, 2017, 29, 465901.
- 58 M. van Setten, M. Giantomassi, E. Bousquet, M. Verstraete, D. Hamann, X. Gonze and G.-M. Rignanese, *Comput. Phys. Commun.*, 2018, 226, 39–54.
- 59 D. R. Hamann, Phys. Rev. B: Condens. Matter Mater. Phys., 2013, 88, 085117.
- 60 G. E. Eperon, G. M. Paternò, R. J. Sutton, A. Zampetti, A. A. Haghighirad, F. Cacialli and H. J. Snaith, *J. Mater. Chem. A*, 2015, 3, 19688–19695.
- 61 J. P. Perdew, Int. J. Quantum Chem., 1985, 28, 497-523.
- 62 A. Jain, S. P. Ong, G. Hautier, W. Chen, W. D. Richards, S. Dacek, S. Cholia, D. Gunter, D. Skinner, G. Ceder and K. A. Persson, *APL Mater.*, 2013, 1, 011002.
- 63 J. P. Perdew, M. Ernzerhof and K. Burke, *J. Chem. Phys.*, 1996, **105**, 9982–9985.
- 64 C. Adamo and V. Barone, *J. Chem. Phys.*, 1999, **110**, 6158–6170.
- 65 T. Bischoff, J. Wiktor, W. Chen and A. Pasquarello, *Phys. Rev. Mater.*, 2019, 3, 123802.
- 66 L. Lin, J. Chem. Theory Comput., 2016, 12, 2242-2249.
- 67 F. Gygi and A. Baldereschi, *Phys. Rev. B: Condens. Matter Mater. Phys.*, 1986, **34**, 4405–4408.
- 68 M. Baranowski, P. Plochocka, R. Su, L. Legrand, T. Barisien, F. Bernardot, Q. Xiong, C. Testelin and M. Chamarro, *Photonics Res.*, 2020, 8, A50–A55.
- 69 Z. Liu, J. A. Peters, C. C. Stoumpos, M. Sebastian, B. W. Wessels, J. Im, A. J. Freeman and M. G. Kanatzidis, Hard X-Ray, Gamma-Ray, and Neutron Detector Physics XV, 2013, 88520A.
- 70 Z. Yang, A. Surrente, K. Galkowski, A. Miyata, O. Portugall, R. J. Sutton, A. A. Haghighirad, H. J. Snaith, D. K. Maude, P. Plochocka and R. J. Nicholas, ACS Energy Lett., 2017, 2, 1621–1627.
- 71 X. Gonze, B. Amadon, P.-M. Anglade, J.-M. Beuken, F. Bottin, P. Boulanger, F. Bruneval, D. Caliste, R. Caracas, M. Côté, T. Deutsch, L. Genovese, P. Ghosez, M. Giantomassi, S. Goedecker, D. Hamann, P. Hermet, F. Jollet, G. Jomard, S. Leroux, M. Mancini, S. Mazevet,

- M. Oliveira, G. Onida, Y. Pouillon, T. Rangel, G.-M. Rignanese, D. Sangalli, R. Shaltaf, M. Torrent. M. Verstraete, G. Zerah and J. Zwanziger, Comput. Phys. Commun., 2009, 180, 2582-2615.
- 72 X. Gonze, F. Jollet, F. Abreu Araujo, D. Adams, B. Amadon, T. Applencourt, C. Audouze, J.-M. Beuken, J. Bieder, A. Bokhanchuk, E. Bousquet, F. Bruneval, D. Caliste, M. Côté, F. Dahm, F. Da Pieve, M. Delaveau, M. Di Gennaro, B. Dorado, C. Espejo, G. Geneste, L. Genovese, A. Gerossier, M. Giantomassi, Y. Gillet, D. Hamann, L. He, G. Jomard, J. Laflamme Janssen, S. Le Roux, A. Levitt, A. Lherbier, F. Liu, I. Lukacevic, A. Martin, C. Martins, M. Oliveira, S. Poncé, Pouillon, T. Rangel, G.-M. Rignanese, A. Romero, B. Rousseau, O. Rubel, A. Shukri, M. Stankovski, M. Torrent, M. Van Setten, B. Van Troeve, M. Verstraete, D. Waroquiers, J. Wiktor, B. Xu, A. Zhou and J. Zwanziger, Comput. Phys. Commun., 2016, 205, 106-131.
- 73 X. Gonze, B. Amadon, G. Antonius, F. Arnardi, L. Baguet, J.-M. Beuken, J. Bieder, F. Bottin, J. Bouchet and E. Bousquet, et al., Comput. Phys. Commun., 2019, 248, 107042.
- 74 X. Gonze, B. Amadon, G. Antonius, F. Arnardi, L. Baguet, J.-M. Beuken, J. Bieder, F. Bottin, J. Bouchet, E. Bousquet, Brouwer, F. Bruneval, G. Brunin, T. Cavignac, J.-B. Charraud, W. Chen, M. Côté, S. Cottenier, J. Denier, G. Geneste, P. Ghosez, M. Giantomassi, Y. Gillet, O. Gingras, D. R. Hamann, G. Hautier, X. He, N. Helbig, N. Holzwarth, Y. Jia, F. Jollet, W. Lafargue-Dit-Hauret, K. Lejaeghere, M. A. L. Marques, A. Martin, C. Martins, H. P. C. Miranda, F. Naccarato, K. Persson, G. Petretto, V. Planes, Y. Pouillon, S. Prokhorenko, F. Ricci, G.-M. Rignanese, A. H. Romero, M. M. Schmitt, M. Torrent, M. J. van Setten, B. V. Troeye, M. J. Verstraete, G. Zérah and J. W. Zwanziger, Comput. Phys. Commun., 2020, 248, 107042.
- 75 N. R. Werthamer, Phys. Rev. B: Solid State, 1970, 1, 572–581.
- 76 T. Tadano, Y. Gohda and S. Tsuneyuki, J. Phys.: Condens.-Matter, 2014, 26, 225402.

- 77 F. Zhou, W. Nielson, Y. Xia and V. Ozolins, Phys. Rev. Lett., 2014, 113, 185501.
- 78 S. Poncé, G. Antonius, Y. Gillet, P. Boulanger, J. Laflamme Janssen, A. Marini, M. Côté and X. Gonze, Phys. Rev. B: Condens. Matter Mater. Phys., 2014, 90, 214304.
- 79 M. Sebastian, J. A. Peters, C. C. Stoumpos, J. Im, S. S. Kostina, Z. Liu, M. G. Kanatzidis, A. J. Freeman and B. W. Wessels, Phys. Rev. B: Condens. Matter Mater. Phys., 2015, 92, 235210.
- 80 J. B. Hoffman, A. L. Schleper and P. V. Kamat, J. Am. Chem. Soc., 2016, 138, 8603-8611.
- 81 C. C. Stoumpos, C. D. Malliakas and M. G. Kanatzidis, Inorg. Chem., 2013, 52, 9019-9038.
- 82 G. E. Eperon, S. D. Stranks, C. Menelaou, M. B. Johnston, L. M. Herz and H. J. Snaith, Energy Environ. Sci., 2014, 7, 982-988.
- 83 T. Haeger, R. Heiderhoff and T. Riedl, I. Mater. Chem. C, 2020, 8, 14289-14311.
- 84 R. J. Sutton, M. R. Filip, A. A. Haghighirad, N. Sakai, B. Wenger, F. Giustino and H. J. Snaith, ACS Energy Lett., 2018, 3, 1787-1794.
- 85 B. T. Diroll, H. Zhou and R. D. Schaller, Adv. Funct. Mater., 2018, 28, 1800945.
- 86 R. Saran, A. Heuer-Jungemann, A. G. Kanaras and R. J. Curry, Adv. Opt. Mater., 2017, 5, 1700231.
- 87 J. Yi, X. Ge, E. Liu, T. Cai, C. Zhao, S. Wen, H. Sanabria, O. Chen, A. M. Rao and J. Gao, Nanoscale Adv., 2020, 2, 4390-4394.
- 88 T. Lanigan-Atkins, X. He, M. J. Krogstad, D. M. Pajerowski, D. L. Abernathy, G. N. M. N. Xu, Z. Xu, D.-Y. Chung, M. G. Kanatzidis, S. Rosenkranz, R. Osborn and O. Delaire, Nat. Mater., 2021, 20, 977-983.
- 89 M. Zacharias and F. Giustino, Phys. Rev. Res., 2020, 2, 013357.
- 90 M. Zacharias and F. Giustino, Phys. Rev. B, 2016, 94, 075125.

# THE JOURNAL OF PHYSICAL CHEMICAL SOCIETY

August 18, 2022 Volume 126 Number 32 pubs.acs.org/JPCC





pubs.acs.org/JPCC Article

#### Electronic Properties of Silver-Bismuth Iodide Rudorffite **Nanoplatelets**

Danijela Danilović, Aleksandar R. Milosavljević,\* Pitambar Sapkota, Radovan Dojčilović, Dragana Tošić, Nenad Vukmirović, Milan Jocić, Vladimir Djoković, Sylwia Ptasinska, and Dušan K. Božanić\*



Cite This: J. Phys. Chem. C 2022, 126, 13739-13747



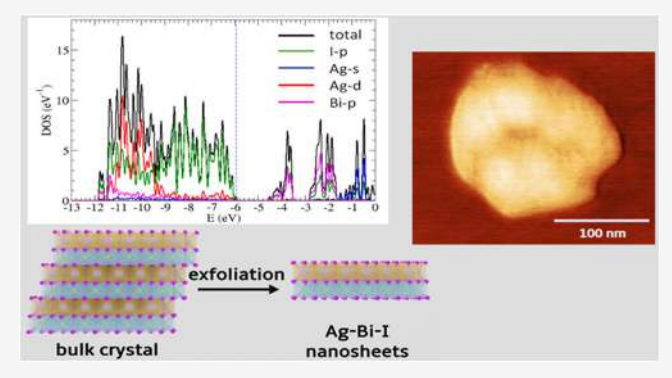
**ACCESS** I

Metrics & More

Article Recommendations

Supporting Information

ABSTRACT: Silver-bismuth iodide (Ag-Bi-I) rudorffites are chemically stable and non-toxic materials that can act as a possible lead-free replacement for methylammonium lead halides in optoelectronic applications. We report on a simple route for fabricating Ag-Bi-I colloidal nanoplatelets approximately 160 nm in lateral dimensions and 1-8 nm in thickness via exfoliation of Ag-Bi-I rudorffite powders in acetonitrile. The valence band electronic structure of isolated Ag-Bi-I nanoplatelets was investigated using synchrotron radiation to perform X-ray aerosol photoelectron spectroscopy (XAPS). The ionization energy of the material was found to be  $6.1 \pm 0.2$  eV with respect to the vacuum level. UV-vis absorption and photoluminescence spectroscopies of the Ag-Bi-I colloids showed that the optical properties of the



nanoplatelets originate from I 5p to Bi 6p and I 5p to I 5p transitions, which is further confirmed by density functional theory (DFT) calculations. Finally, calculations based on the DFT and  $\mathbf{k} \cdot \mathbf{p}$  theoretical methods showed that the quantum confinement effect is very weak in the system studied.

#### INTRODUCTION

Hybrid perovskite materials have attracted extensive research interest in recent years as they exhibit optical and semiconducting properties favorable for the fabrication of optoelectronic devices such as solar cells, light-emitting diodes, and photodetectors. 1-5 Among them, lead-based halide perovskites are the most studied systems since their application as absorbers in solar cells has resulted in the highest value of power conversion efficiency (PCE) of 25%.<sup>6,7</sup> The exceptional performance of this type of material arises from its large absorption coefficient, low effective masses, and high mobility of charge carriers. It has been proposed that these properties originate mainly from the partially oxidized Pb2+ state with 6s<sup>2</sup>6p<sup>0</sup> configuration. However, lead-based perovskite materials are unstable and easily degrade after exposure to high temperatures, electromagnetic radiation, moisture, and oxygen. 9-12 Our previous study also showed that low-energy electrons can affect the structural and chemical properties of methylammonium lead iodide (MAPbI<sub>3</sub>).<sup>13</sup> Furthermore, lead toxicity is a serious predicament for large-scale applications. 14 Thus, continuous research efforts are seeking to develop more stable and less toxic perovskite materials.

Transition metal cations, such as Bi<sup>3+</sup>, Sn<sup>2+</sup>, Ge<sup>2+</sup>, and Sb<sup>3+</sup> also have stable, partially oxidized states, with the same ns<sup>2</sup>np<sup>0</sup> configuration as the lead ion. Consequently, these elements could act as suitable replacements for lead in emergent solar cell absorber materials. Compared to tin-, germanium-, and antimony-based materials, bismuth-based halide perovskites appear to be the most chemically stable and the least toxic. Incorporating an Ag+ or Cu+ cation in the bismuth-halide lattice can lead to the formation of a new type of material with edge-shared  $[AX_6]$  and  $[BiX_6]$  octahedra (A = Ag, Cu, X = I,Br) named rudorffites. 15 These metal halides may appear in many compositions that vary depending on the number of occupied sites in the cation sublattice. Several methods for fabricating silver-bismuth iodide (Ag-Bi-I) have been proposed. 15-22 Most of these procedures were oriented toward the synthesis of bulk material. For example, Ag-Bi-I powders were produced by heating a mixture of the precursor powders at temperatures above 600 °C under vacuum, 15,18,23 while the thin films can be fabricated via spin-coating or dynamic hotcasting of precursor solutions in organic solvents. 16,21,24-26 In our previous study, we fabricated Ag<sub>3</sub>BiI<sub>6</sub> spherical nanoparticles in the form of aerosols and investigated their

Received: May 9, 2022 Revised: July 28, 2022 Published: August 9, 2022





electronic properties via synchrotron radiation X-ray aerosol photoelectron spectroscopy (XASP).<sup>27</sup>

The band structure of 2D perovskite materials may depend on the size of the particles and structural modification induced by various factors. 28-37 For example, Kanatzidis and coworkers<sup>28</sup> used organic spacer cations to create separation between adjacent layers in Ag-Bi-I particles. It was shown that the optical properties depended on the type of spacer cations used, i.e., the changes in the distances between the layers. Also, previous studies on layered semiconducting colloidal nanoparticles showed a strong effect of size reduction on their optical properties due to the confinement effect, 38-41 which initiated the same type of research in layered perovskite nanomaterials. It was observed that Pb- and Sn-based nanoplatelets also display a strong quantum confinement effect with optical properties that depend on the particle thickness, i.e., the number of layers. <sup>29–33</sup> Conversely, in the most-studied 2D lead-free systems  $Cs_2AgBiX_6$  (X = Cl, Br, or I), the quantum confinement is rather weak.<sup>34,36,42</sup> Pal et al.<sup>37</sup> also showed that Rb<sub>3</sub>Bi<sub>2</sub>I<sub>9</sub> 2D colloidal nanoparticles have the same band structure characteristics as their bulk counterparts.

In this work, we present a simple method for the preparation of colloidal 2D layered Ag—Bi—I rudorffite nanostructures based on the exfoliation of Ag—Bi—I powders. The study focused on the optical properties and valence band electronic structure of the resulting nanoplatelets. The valence band structure of isolated Ag—Bi—I nanoplatelets was studied using synchrotron radiation XASP. Obtained electronic spectra were discussed and interpreted with the results from density functional theory calculations.

#### **■ EXPERIMENTAL SECTION**

**Materials.** Bismuth(III) iodide (BiI<sub>3</sub>, purity: 99%), silver iodide (AgI, purity: 99%), and sodium citrate tribasic dihydrate  $(C_6H_5Na_3O_7\cdot 2H_2O)$  were purchased from Sigma Aldrich and used as received. Dimethyl sulfoxide (DMSO) and acetonitrile were used as solvents.

**Synthesis.** Ag–Bi–I nanopowder was prepared from 234 mg of AgI and 295 mg of BiI<sub>3</sub> powders (molar ratio of AgI/BiI<sub>3</sub> = 2:1) mixed and ground with a mortar until the mixture became light gray. The resulting powder was dissolved in 50 mL of DMSO (0.01 M). Subsequently, 10 mL of sodium citrate (0.3 M DMSO solution) was added to the solution as a stabilizing agent. The solution was stirred for 15 min, cast in a Petri dish, and heated to 120 °C in a vacuum oven to evaporate the solvent. The prepared nanopowders were characterized either in the dry state or dispersed in acetonitrile (0.6 mg/mL) to obtain the colloids. Photographs of the Ag–Bi–I powder and the Ag–Bi–I colloid are shown in Supporting Information Figure S1. For comparison with Ag–Bi–I, BiI<sub>3</sub> nanopowders and colloids were fabricated using the same procedure.

**Characterization.** X-ray diffraction (XRD) measurements of the samples deposited on an oriented Si wafer were performed using a Rigaku SmartLab system using Cu  $K_{\alpha}$  radiation (1.5406 Å, 30 mA, 40 kV) and operated in the  $2\theta$  range from 10 to  $50^{\circ}$ .

Scanning electron microscopy (SEM) analyses of powdered samples were performed with a JEOL JSM-6390 LV instrument using a 30 kV acceleration voltage. Before analysis, the samples were deposited onto an adhesive carbon tape and coated with a thin gold layer. Transmission electron microscopy (TEM) was carried out with a JEOL JEM-1400

operating at 120 kV. For the analyses, the colloidal samples were deposited onto a carbon-coated copper grid with 300 mesh and dried in vacuum.

Surface topography investigations were performed using a Quesant atomic force microscope (AFM). Colloids were deposited on freshly cleaved mica substrates by spin-coating (3500 rpm, 1 min) and investigated immediately. Measurements were made in AFM tapping mode at room temperature, using standard silicon probes Q-WM300 (force constant 40 N/m).

The UV—vis diffuse reflectance and absorption spectra of the nanopowders and dispersed colloid samples were measured with a Shimadzu UV-2600 (Shimadzu Corporation, Japan) spectrophotometer equipped with an integrating sphere (ISR-2600 Plus) over the 220—800 nm range. Photoluminescence spectra (PL) of the colloidal samples were recorded with a PerkinElmer LS45 fluorescence spectrophotometer.

Surface X-ray photoelectron spectroscopy (XPS) measurements were carried out on an ambient pressure SPECS Surface Nano Analysis GmbH X-ray photoelectron spectrometer with a monochromatic Al  $K_{\alpha}$  X-ray source (1486.6 eV). For the analysis, the acetonitrile dispersions were deposited onto a glass substrate following the procedure described in the literature by Sansom et al. High-resolution spectra were recorded with a pass energy of 20 eV, which gave a full width at half-maximum of  $\sim$ 0.5 eV for the Au  $4f_{7/2}$  peak. The binding energy was calibrated with respect to the Fermi level by adjusting the position of the adventitious C 1s peak to 284.8 eV.

X-ray aerosol photoelectron spectroscopy (XAPS) was performed at the PLEIADES beamline of the SOLEIL synchrotron using the Multi-Purpose Source Chamber (MPSC) and the Scienta hemispherical electron analyzer. A detailed description of the experimental setup is provided in our previous study.<sup>27</sup> For these measurements, the Ag-Bi-I aerosols were generated from acetonitrile dispersions of Ag-Bi-I nanoparticles using a TSI 3076 atomizer. Carried by 2.5 bar of Ar gas, the aerosols were transported through a metallic tube, heated to a temperature of  $\sim$ 80 °C, and then cooled to 0 °C via a cold trap to remove excess acetonitrile. Subsequently, the free aerosols were introduced through a pressure-limiting orifice (250  $\mu$ m in diameter) into an aerodynamic lens system and placed inside the differentially pumped stage of the MPSC. The aerodynamic lens focused the nanoparticle beam into the high-vacuum interaction region of the photoelectron spectrometer through a skimmer (1.5 mm diameter). The particle beam was ionized with 100 eV monochromatic synchrotron radiation. Gas-phase XPS spectra were recorded using a wideangle-lens VG-Scienta R4000 electron energy analyzer. The overall resolution of the valence electron spectra was about 170 meV. Spectra were calibrated relative to the vacuum level using the binding energy of  $3p_{3/2}$  Ar carrier gas at 15.76 eV<sup>1,43</sup> with an overall uncertainty of less than 0.2 eV.

Calculation Methods. Density Functional Theory Calculations with the PBE Functional. Density functional theory (DFT) calculations were performed by modeling the exchange-correlation functional using the Perdew–Burke–Ernzerhof (PBE) generalized gradient approximation (GGA). Norm-conserving fully relativistic pseudopotentials were used to model the effect of core electrons, and the effects of spin-orbit interaction were fully included. A Quantum Espresso code, which is based on the representation of wave functions in the basis of plane waves,

was used to perform these calculations. The kinetic energy cutoff for the plane-wave representation of wave functions was 50 Ry. Relaxation of lattice parameters and atomic coordinates were performed until the atomic forces were smaller than  $10^{-3}$  Ry/bohr.

Density Functional Theory Calculation with the Hybrid PBEO Functional. Since local and semilocal functionals in DFT (such as the PBE functional) do not result in accurate values of the band gap, <sup>49</sup> we also performed the calculation of bulk band structure using the hybrid PBE0 functional. 50,51 This functional modeled the correlation energy as the PBE correlation energy, while the exchange energy was modeled as the sum of threefourths of the PBE exchange energy and one-fourth of the Hartree-Fock exchange energy. It is known that the calculations with this functional yield band gap values that correlate significantly better with experimental band gaps of semiconducting materials than those carried out with the PBE functional (see for example refs 52 and 53). However, calculations based on the PBE0 functional are computationally significantly more demanding since they also request calculations of the Hartree-Fock exchange energy. For this reason, we used this functional only to perform bulk band structure calculations of a given bulk atomic structure. The calculation was performed using the Quantum Espresso code, where the adaptively compressed exchange operator approach for calculating exchange energy<sup>54</sup> is implemented.

 $\mathbf{k} \cdot \mathbf{p}$  Calculations of the Electronic Structure. To calculate larger nanoplatelets (quantum wells), we constructed the  $\mathbf{k} \cdot \mathbf{p}$  Hamiltonian following the approach presented in ref 55, where its parameters are determined by ab initio calculations (using either DFT/PBE or the hybrid PBE0 functional methods) of bulk material.  $\mathbf{k} \cdot \mathbf{p}$  calculations are numerically very cheap and can therefore easily be applied to larger nanoplatelets for which DFT/PBE calculation is computationally very demanding and hybrid functional calculation is practically impossible to perform. Additional details related to  $\mathbf{k} \cdot \mathbf{p}$  calculations are presented in the Supporting Information.

Determination of Absolute Positions of Bulk Energy Levels with Respect to Vacuum. DFT calculations with plane-wave basis and periodic boundary conditions do not yield the absolute value of the position of the energy levels with respect to vacuum. These positions were determined by performing the calculation of the interface of the material slab with vacuum as described in more detail in the Supporting Information. All the energies that we subsequently report are with vacuum as the zero energy.

#### ■ RESULTS AND DISCUSSION

**Characterization of the Ag–Bi–I Nanoplatelets.** The results of the X-ray diffraction measurements of the Ag–Bi–I powders are presented in Figure 1a. The XRD pattern of the sample shows diffraction maxima at  $2\theta$  angles of 12.7, 23.9, 25.1, 25.6, 29.2, 32.0, 41.4, 42.2, and 43.5°, which correspond to the CdCl<sub>2</sub>-type rhombohedral structure of a silver-rich Ag–Bi–I rudorffite system. <sup>15,19,56</sup> In addition, low-intensity peaks at 22.3, 23.7, 39.2, and 46.3° indicate a small contribution of the  $\gamma$ -AgI phase. <sup>20</sup> Similar diffraction patterns were observed in various other types of Ag–Bi–I structures, for example, Ag<sub>3</sub>BiI<sub>6</sub> nanoparticles produced in the gas phase from iodide precursors, <sup>27</sup> Ag–Bi–I nanoparticles fabricated from nitrate salts, <sup>57</sup> Ag–Bi–I thin films produced by the dynamic hotcasting method, <sup>21</sup> and Ag–Bi–I thin films produced on a TiO<sub>2</sub>/FTO/glass substrate. <sup>58</sup> The appearance of the AgI phase

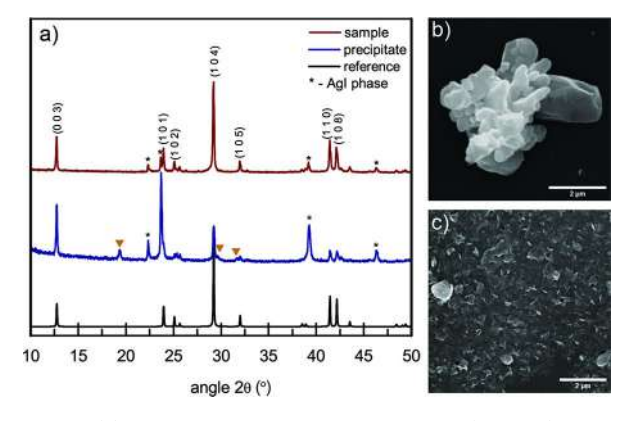


**Figure 1.** (a) XRD patterns of Ag–Bi–I powder (red line) and the precipitate sample obtained by drying Ag–Bi–I acetonitrile dispersion under ambient conditions (blue line). The black line represents the Ag<sub>3</sub>BiI<sub>6</sub> reference pattern. <sup>56</sup> The asterisks and triangles mark the  $2\theta$  angles corresponding to the diffraction maxima of the AgI phase <sup>20</sup> and the BiOI phase, <sup>58</sup> respectively. SEM images of (b) Ag–Bi–I powder and (c) precipitate samples.

in the sample is expected since in the Ag-rich Ag-Bi-I solids, the excess of Ag ions are delocalized and occupy the sites between the (Ag/Bi)I<sub>6</sub> octahedral layers. 19 The XRD measurements were performed on a precipitate of the Ag-Bi-I sample in order to check its structure after dispersion in acetonitrile. This sample is prepared by drying the colloid in the dark under ambient conditions. The XRD pattern of the precipitate (Figure 1a, blue line) shows that in addition to the increase in the AgI content, the sample retained its Ag-Bi-I phase. Changes in morphology were also investigated by SEM, and the images of two samples are shown in Figure 1b,c. These analyses showed that exfoliation of Ag-Bi-I sheets upon dispersion in acetonitrile takes place, which is consistent with an increase in the intensity of (0 0 3) diffraction maximum relative to the (1 0 4) peak in the diffractogram of the precipitate. In addition, the presence of the bismuth oxyiodide (BiOI) phase in the diffraction pattern can be seen, resulting from drying the sample in air. This result indicates that oxidation occurs at the outmost layers of the exfoliated

Further analyses of the size and morphology of the dispersed-phase Ag-Bi-I particles were carried out by transmission electron microscopy on the colloidal samples dried in a vacuum. Typical TEM images of the sample are presented in Supporting Information Figure S2. For comparison, the results for BiI<sub>3</sub> particles, prepared using the same procedure, are also given. The micrographs show that the Ag-Bi-I particles have a plate-like morphology with average lateral dimensions of ~160 nm. A similar morphology was also observed for BiI3 nanoparticles; however, their lateral dimensions were in the 40-60 nm range. The observed morphology is characteristic of binary metal iodides (such as Bil<sub>3</sub><sup>41,59</sup>) and occurs because of a relatively large difference in distance between cations in edge-sharing octahedra and the distance between cations in adjacent layers. In rudorffite  $Ag_{2-3x}Bi_xI_2$  (x = 0.33-0.60) ternary halides, Ag and Bi ions occupy similar edge-sharing octahedral sites (Ag/Bi)I<sub>6</sub><sup>15,19</sup> which results in the formation of the Ag-Bi-I nanoplatelets. The HRTEM/EDS mapping of Ag-Bi-I nanoplatelets (Supporting information Figure S2c) showed that the elements were uniformly distributed in the particles. The distribution of the thicknesses of the nanoplatelets was determined from their

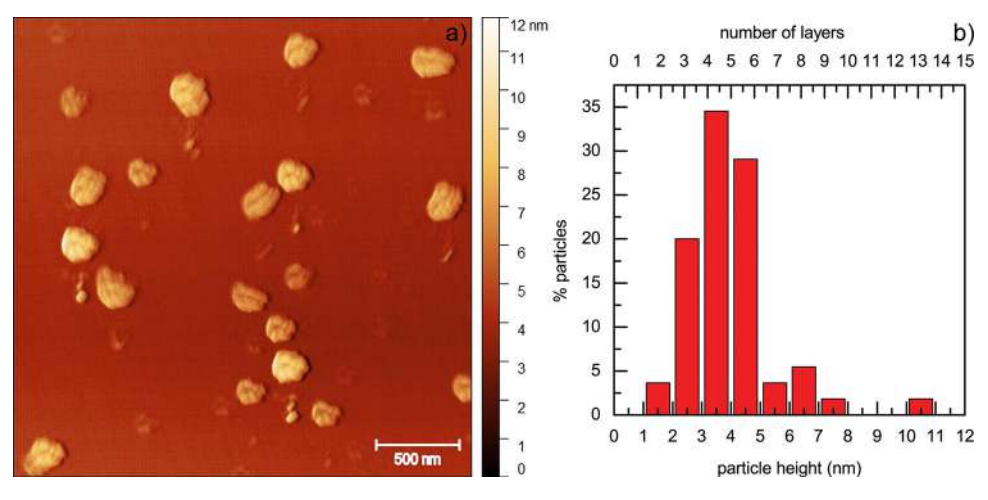


Figure 2. (a) AFM image of Ag-Bi-I nanoplatelets and (b) corresponding distribution of particles' heights. The number of Ag-Bi-I monolayers in the nanoplatelets was estimated assuming a monolayer thickness of 0.66 nm.

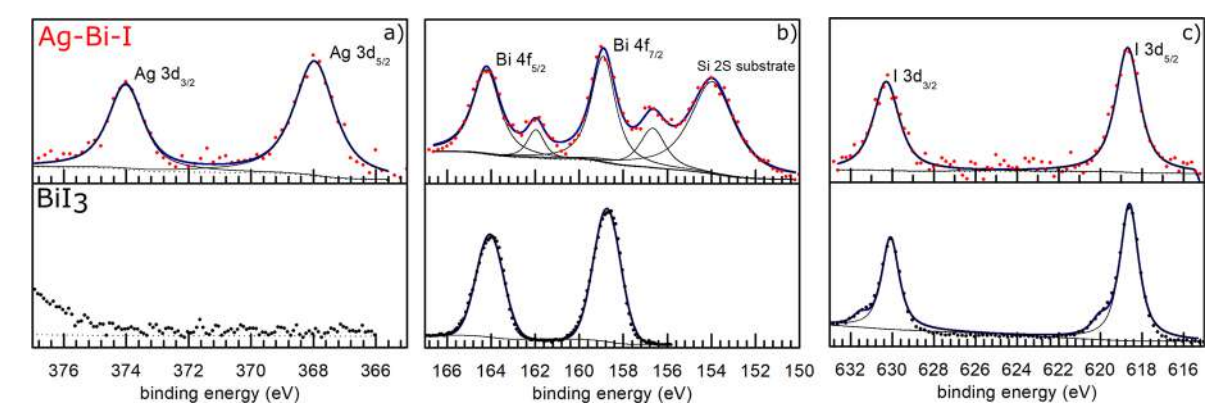


Figure 3. High-resolution XPS spectra of (a) Ag 3d, (b) Bi 4f, and (c) I 3d core levels of Ag-Bi-I (top) and BiI<sub>3</sub> (bottom) colloidal nanoplatelets.

height profiles obtained by AFM. The AFM image of the Ag—Bi—I sample and the particle height distribution are presented in Figure 2a,b, respectively, while the details of the height profile analyses are given in the Supporting Information (Figure S3). The average thickness of the nanoplatelets was found to be 3.9  $\pm$  0.2 nm. Taking into account that the thickness of the monolayer is ~0.66 nm, the nanoplatelets, on average, have six layers.

The chemical environment of the ions in the Ag-Bi-I nanoplatelets was investigated by surface X-ray photoelectron spectroscopy. High-resolution XPS spectra of the Ag 3d, Bi 4f, and I 3d core levels of the Ag-Bi-I nanoplatelets are presented in Figure 3. The survey scan of the sample is given in Supporting Information Figure S4. For comparison, the results for the BiI<sub>3</sub> sample are also shown. For the Ag-Bi-I sample, Ag  $3d_{3/2}$  and Ag  $3d_{5/2}$  levels are observed at 374.0 and 368.0 eV, respectively (Figure 3a). These values match the binding energies obtained for Ag 3d levels in AgI.<sup>60</sup> For Bi, 4f levels (Figure 3b) are assigned to peaks at 164.2 and 158.9 eV, corresponding to Bi  $4f_{5/2}$  and Bi  $4f_{7/2}$  levels. The spectrum shows additional peaks at lower binding energies that are not present for the BiI<sub>3</sub> sample. These features were previously reported for the Ag-Bi-I films prepared by thermal evaporation<sup>61</sup> as well as for the oriented BiI<sub>3</sub> single crystals in contact with Pd and Pt.62 The peaks were assigned to bismuth ions that are not in a complete 6I+ coordination and therefore approach binding energies characteristic for metallic

bismuth. The binding energies of I  $3d_{3/2}$  and I  $3d_{5/2}$  levels are observed at 630.3 and 618.7 eV (Figure 3c). It should be noticed that the I 3d levels in the Ag-Bi-I sample are slightly broader than in the BiI<sub>3</sub> sample, suggesting possible effects of changes in the chemical environment. The XPS results suggest that a redox solid-state reaction between Ag and BiI<sub>3</sub> is taking place in the system, resulting in the formation of Ag-Bi-I and AgI phases, as well as metallic Bi (which can proceed to the formation of BiOI in the presence of oxygen), noticed in the XRD pattern (Figure 1). A similar redox reaction was observed at the interfaces between Ag and Bi<sub>2</sub>Se<sub>3</sub> single crystals.<sup>63</sup>

Electronic Properties of the Ag-Bi-I Nanoplatelets. To study the electronic properties of Ag-Bi-I nanoplatelets in the valence region, we used a similar approach as in our previous study of MAPbBr<sub>3</sub> nanoparticles. Two complementary X-ray photoemission spectroscopy techniques were employed. For XPS measurements, the colloids were deposited onto a Si substrate. The XAPS measurements were carried out on isolated Ag-Bi-I particles, where synchrotron radiation was used as the X-ray source.

The photoemission spectrum of Ag–Bi–I nanoplatelets obtained by the XAPS technique is presented in Figure 4, while the corresponding spectrum of the BiI<sub>3</sub> sample is given in the Supporting Information (Figure S5a). Contrary to XPS measurements, where the band energies are referenced with respect to the Fermi level ( $E_{\rm F}$ ), all energies in the XAPS technique are measured with respect to the vacuum level ( $E_{\rm 0}$ ).  $^{1}$ 

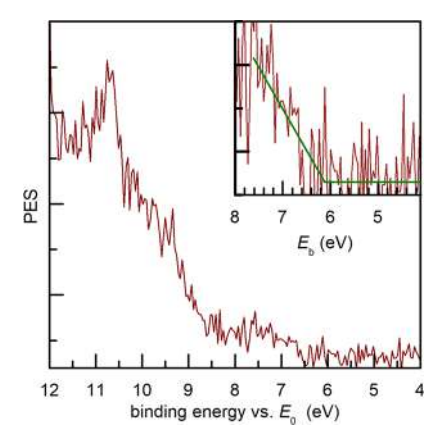


**Figure 4.** Valence region photoemission spectrum of Ag-Bi-I nanoplatelets measured by XAPS using 100 eV photon energy. The inset shows the zoom-in region around the ionization energy value.

The ionization energy of Ag-Bi-I nanoplatelets determined by XAPS is 6.1  $\pm$  0.2 eV relative to  $E_0$ . This is in good agreement with the ionization energies reported for 3D Ag<sub>3</sub>BiI<sub>6</sub> aerosol particles<sup>27</sup> and Ag<sub>3</sub>BiI<sub>6</sub> thin films<sup>58</sup> as well as those reported for rhombohedral  $Ag_{0.65}Bi_{0.45}I_2$  materials. <sup>19</sup> This indicates a negligible influence of the size and morphology of Ag-Bi-I particles on the position of the valence band maxima. The ionization energy is also in good agreement with our calculated value of -5.95 eV for the valence band maximum. The ionization energy obtained by surface XPS was  $1.4 \pm 0.2$ eV relative to  $E_{\rm F}$  (Supporting Information Figure S5b). By comparing the values of the ionization energies obtained by these two techniques, the estimated value of the work function  $(\phi)$  of Ag-Bi-I nanoplatelets was found to be 4.7 eV. It should be noted, however, that in the XAPS of isolated nanoparticles, the near-surface vacuum level cannot be perfectly defined, which results in additional uncertainty in the determination of the ionization energy.<sup>64,65</sup>

The optical properties of the Ag-Bi-I powder and the colloidal dispersion in acetonitrile are presented in Figure 5. The diffuse reflectance spectrum of the Ag-Bi-I powder samples (dashed black line) displays an onset of absorption at 732 nm ( $\sim$ 1.7 eV), which is a typical value for the band gap of Ag-Bi-I thin films and powder samples. <sup>15,21,23</sup> After exfoliation, the UV-vis absorption spectrum of the Ag-Bi-I

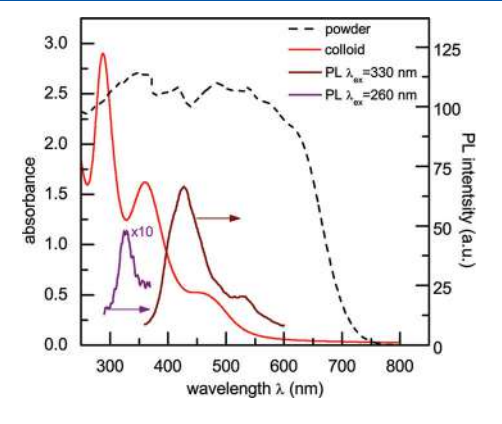


**Figure 5.** UV—vis absorption (red line) and photoluminescence (PL) (purple and brown lines) spectra of Ag—Bi—I nanoplatelets dispersed in acetonitrile and the diffuse reflectance spectrum of Ag—Bi—I powders (dashed black line).

colloid (solid red line) shows three bands at 288 nm (4.30 eV), 360 nm (3.44 eV), and 457 nm (2.71 eV). The bands in the spectra of the Ag-Bi-I colloid originate mainly from I 5p to Bi 6p and I 5p to I 5p transitions in  $(BiI_6)^{3-}$  octahedra. It should be noted that the absorption spectra obtained for BiI<sub>3</sub> powder and its dispersion in acetonitrile are similar to those obtained for corresponding Ag-Bi-I samples (Supporting Information Figure S7). The absorption spectrum of the BiI<sub>3</sub> powder (Figure S7) exhibited a slightly lower band gap value, which is in accordance with the results presented in the literature.<sup>61</sup> On the other hand, the absorption spectrum of the BiI<sub>3</sub> dispersion has similar features as the spectrum of the Ag-Bi-I colloid, although the absorption peaks appear at slightly different energies. It seems that the changes induced by the additional element in the structure affect I 5p to Bi 6p and I 5p to I 5p transitions to a certain extent. A recent study by Kanatzidis et al.<sup>28</sup> may support this conclusion. They showed that the optical properties of 2D Ag-Bi-I layered materials significantly depend on both the distance between the layers and the arrangement and orientation of (AgI<sub>6</sub>)<sup>5-</sup> and (BiI<sub>6</sub>)<sup>3-</sup> octahedra.

Recently, Premkumar et al. synthesized Ag-Bi-I quantum dots and noticed that they exhibited blueshifted absorption with respect to the bulk material.<sup>66</sup> The observed shift is attributed to the size confinement effect. However, because the effective masses of the charge carriers in Ag-Bi-I material are relatively large,<sup>58</sup> it can be expected that the quantum confinement effects in the Ag-Bi-I nanoplatelets are relatively weak. Indeed, our calculations (see Figure 7 below) showed that the nanoplatelet band gap changes by only about 50 meV in the range of thicknesses from 2 to 5 nm. This suggests that the three peaks at 2.71, 3.44, and 4.30 eV are the internal transitions already present in the bulk sample as well, which become more pronounced after exfoliation. To check this, we made a rough calculation of the optical absorption for the bulk Ag-Bi-I (see Supporting Information Figure S6). The theoretical absorption curve in Figure S6 exhibits a similar trend as the experimental absorption spectrum of Ag-Bi-I colloid in the UV-vis range.

The photoluminescence spectra of the Ag-Bi-I nano-platelets dispersed in acetonitrile, recorded with 260 nm (purple solid line) and 330 nm (brown solid line) excitations, are also presented in Figure 5. The emission bands at around 326, 430, and 530 nm are Stokes-shifted with respect to the band observed in the absorption spectrum. The excitation of the colloids by the light of different wavelengths did not affect the position of the emission bands (Supporting Information Figure S8). Notably, the emission at the photon energy of the band gap was not detected in either powder or colloid samples.

DFT was used to calculate the electronic structure of Ag—Bi—I nanoplatelets. The calculations of the electronic structure of the platelets with larger lateral dimensions were performed by the  $\mathbf{k}\cdot\mathbf{p}$  method, and the Hamiltonian parameterization was carried out using the results obtained by the DFT. As a model for the atomic structure of the Ag—Bi—I material, we used the rhombohedral AgBiI<sub>4</sub> configuration. The details about its atomic structure, corresponding lattice parameters, and atomic positions are given in the Supporting Information.

The electronic band structure of bulk  $AgBiI_4$  obtained from DFT/PBE calculations is presented in Figure 6a. A direct band gap can be observed at the  $Y_2$  point in the Brillouin zone with a band gap energy of 0.33 eV was found. As expected, the DFT/PBE calculation yields a significantly lower value of the band

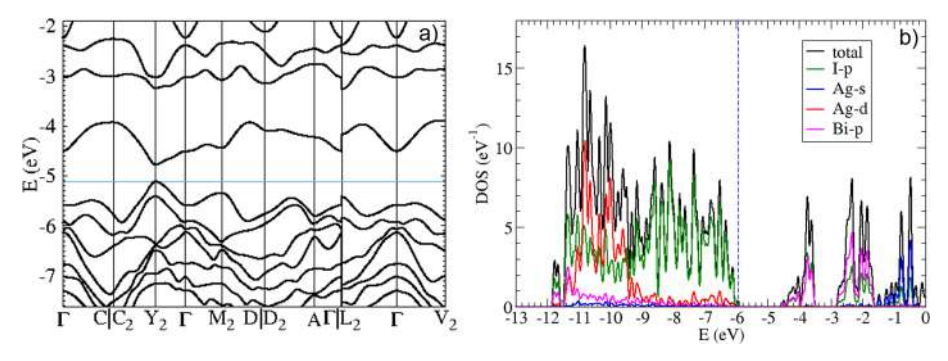


Figure 6. (a) Electronic band structure of AgBiI<sub>4</sub> obtained from DFT/PBE calculations. The blue horizontal line represents the valence band maximum energy. The choice of the path in the Brillouin zone was made using the SeeK-path tool.<sup>67</sup> (b) Density of electronic states (total density of states and orbital projected density of states) of AgBiI<sub>4</sub> obtained from hybrid PBE0 functional calculations. The vertical dashed line denotes the energy of the valence band maximum. The reported energy values in figures (a) and (b) are given with respect to the vacuum level.

gap than the energy value established in the experiment. For this reason, an additional approach was considered, and the calculation was performed using the hybrid PBE0 functional. In this calculation, the band gap energy of 1.3 eV was obtained, which is much closer to the experimental result of 1.7 eV. The calculated densities of electronic states are presented in Figure 6b. The results suggest that the highest states in the valence band (in the energy interval of  $\sim$ 3 eV below the valence band maximum) originate from p-orbitals of the I atom, while the lowest states in the conduction band (in the energy interval of  $\sim$ 2.5 eV above the conduction band minimum) originate from p-orbitals of the Bi and I atoms. This result is in agreement with the previous reports<sup>23,28</sup> and supports the claim that the optical transitions in Ag—Bi—I are dominated by I Sp to Bi 6p and by I Sp to I Sp transitions in the (BiI<sub>6</sub>)<sup>3-</sup>.

Since the lateral dimensions of the Ag–Bi–I nanoplatelets are much larger than vertical dimensions (Figure 2), they were modeled as quantum wells infinite in the xy plane with width L in the z-direction. The procedure for constructing their atomic structure is presented in the Supporting Information. Three different methods were employed to calculate the electronic structure of AgBiI<sub>4</sub> quantum wells: (i) DFT/PBE; (ii)  $\mathbf{k} \cdot \mathbf{p}$  method with parameterization based on DFT/PBE calculations of bulk AgBiI<sub>4</sub>; (iii)  $\mathbf{k} \cdot \mathbf{p}$  calculations with parameterization based on hybrid PBE0 functional calculations of bulk AgBiI<sub>4</sub>.

The results obtained by using method (i) are presented in the Supporting Information. This method cannot give accurate values of the band gap, but it is still useful for gaining insight into the overall role of quantum confinement effects. The results indicate that these effects are quite weak. In the range of well widths of 2 to 5 nm (corresponding to the range of the heights of the nanoplatelets that were observed), the band gap changes for about 50 meV only (see Figure S12 in the Supporting Information). The comparison of the band structures of quantum wells with different widths (Figures S13 and S14 in the Supporting Information) also suggests that the electronic structure is only weakly dependent on the well width. Therefore, within a reasonably good approximation, it follows that the electronic structure of the nanoplatelet is rather similar to the electronic structure of the bulk material.

The calculations using method (ii) were used to confirm that the  $\mathbf{k} \cdot \mathbf{p}$  method is reliable for the calculation of electronic states in quantum wells. Details of this calculation are reported in the Supporting Information. The results suggest that  $\mathbf{k} \cdot \mathbf{p}$ 

and DFT/PBE yield essentially the same results for well widths above 2 nm, which implies that  $\mathbf{k} \cdot \mathbf{p}$  can be safely used then.

Finally, method (iii) was employed to calculate the band gap, conduction band minimum (CBM), and valence band maximum (VBM) of the quantum wells of various sizes. The results (Figure 7) indicate a rather weak dependence of

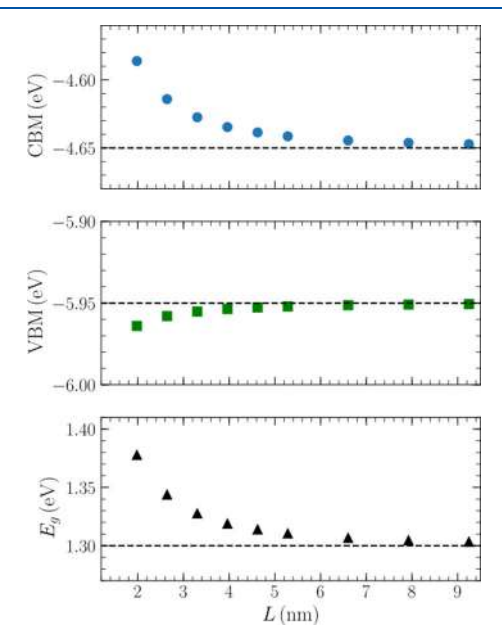


**Figure 7.** The dependence of CBM, VBM, and energy gap  $(E_{\rm g})$  on quantum well width. The results were obtained from the  ${\bf k}{\cdot}{\bf p}$  Hamiltonian parameterized using the data from hybrid PBE0 functional calculations of bulk Ag–Bi–I. Horizontal dashed lines denote the bulk values.

electronic states energies on the well width, consistent with previous conclusions obtained by using less accurate methods. It was also estimated that the dielectric contrast between the nanoplatelet and the solvent does not affect the energy levels of the nanoplatelet to a significant extent (see the Supporting Information for details).

#### CONCLUSIONS

In summary, we report a simple procedure for the chemical exfoliation of sliver/bismuth iodide powders into Ag-Bi-I nanoplatelets dispersible in acetonitrile together with results of characterization and electronic structure determination.

The XRD results showed that the material prepared is composed of a rhombohedral Ag-rich rudorffite phase with minor traces of the  $\gamma$ -AgI phase. The results of the morphological characterization revealed that the material is in the form of layered two-dimensional nanoplatelets with lateral dimensions of  $\sim$ 160 nm and thicknesses in the 1–8 nm range, indicating that the prepared nanoplatelets consist of 1-10 Ag-Bi-I monolayers. XPS analyses of the Ag 3d, Bi 4f, and I 3d core levels suggested that the Ag-Bi-I rudorffite phase is being formed by a redox reaction between Ag and BiI<sub>3</sub>, which also results in the formation of  $\gamma$ -AgI and metallic Bi phases. The valence band electronic structure of isolated Ag-Bi-I nanoplatelets was investigated by synchrotron radiation X-ray aerosol photoelectron spectroscopy. An ionization energy of  $6.1 \pm 0.2$  eV was obtained with respect to the vacuum level. The value of the ionization energy was found to be  $1.4 \pm 0.2$ eV with respect to the Fermi level by standard XPS. We therefore estimated the work function of Ag-Bi-I nanoplatelets to be 4.7 eV. The band gap value of Ag-Bi-I powder was estimated to be ~1.7 eV based on the diffuse reflectance spectrum. The UV-vis absorption spectroscopy of the Ag-Bi-I colloids showed that the optical properties of the nanoplatelets originate mainly from I 5p to Bi 6p and I 5p to I 5p transitions, which is further confirmed by DFT calculations. To interpret the electronic properties of the Ag-Bi-I nanoplatelets with larger lateral dimensions, we performed electronic structure calculations using the density functional theory and  $\mathbf{k} \cdot \mathbf{p}$  methods. The DFT results showed weak dependence of the ionization energy and the band gap values of Ag-Bi-I nanoplatelets on their thickness.

This work demonstrates a simple and innovative route for the preparation of colloidal 2D layered Ag-Bi-I nanomaterials. In addition, the study offers a deeper insight into the understanding of the electronic structure of the Ag-Bi-I nanoplatelets, which were further correlated with the particle size.

#### ASSOCIATED CONTENT

#### **Supporting Information**

The Supporting Information is available free of charge at https://pubs.acs.org/doi/10.1021/acs.jpcc.2c03208.

Images of Ag-Bi-I powder and Ag-Bi-I dispersed in acetonitrile; results of TEM and EDS analyses; AFM images with AFM profile analysis of Ag-Bi-I nanoplatelets; XPS survey scan of Ag-Bi-I nanoplatelets; valence region XPS spectra of Ag-Bi-I and BiI<sub>3</sub> nanoparticles; comparison of calculations with experimental absorption spectra; absorption spectra of Ag-Bi-I and BiI<sub>3</sub> powders and their dispersion in acetonitrile; PL spectra of Ag-Bi-I dispersed in acetonitrile; details of DFT calculations (PDF)

#### AUTHOR INFORMATION

#### **Corresponding Authors**

Aleksandar R. Milosavljević – Synchrotron SOLEIL, l'Orme des Merisiers, 91192 Gif sur Yvette Cedex, France;

o orcid.org/0000-0003-3541-8872; Email: milosavljevic@synchrotron-soleil.fr

 Dušan K. Božanić – Department of Radiation Chemistry and Physics, "Vinča" Institute of Nuclear Sciences - National Institute of the Republic of Serbia and Center of Excellence for Photoconversion, "Vinča" Institute of Nuclear Sciences - National Institute of the Republic of Serbia, University of Belgrade, 11001 Belgrade, Serbia; orcid.org/0000-0001-8246-9635; Email: bozanic@vin.bg.ac.rs

#### **Authors**

Danijela Danilović — Department of Radiation Chemistry and Physics, "Vinča" Institute of Nuclear Sciences - National Institute of the Republic of Serbia and Center of Excellence for Photoconversion, "Vinča" Institute of Nuclear Sciences - National Institute of the Republic of Serbia, University of Belgrade, 11001 Belgrade, Serbia

Pitambar Sapkota – Radiation Laboratory, University of Notre Dame, Notre Dame, Indiana 46556, United States; Department of Physics, University of Notre Dame, Notre Dame, Indiana 46556, United States

Radovan Dojčilović — Department of Radiation Chemistry and Physics, "Vinča" Institute of Nuclear Sciences - National Institute of the Republic of Serbia and Center of Excellence for Photoconversion, "Vinča" Institute of Nuclear Sciences - National Institute of the Republic of Serbia, University of Belgrade, 11001 Belgrade, Serbia; Department of Experimental and Health Sciences, Pompeu Fabra University, 08003 Barcelona, Spain

Dragana Tošić – Department of Radiation Chemistry and Physics, "Vinča" Institute of Nuclear Sciences - National Institute of the Republic of Serbia, University of Belgrade, 11001 Belgrade, Serbia

Nenad Vukmirović — Institute of Physics Belgrade, University of Belgrade, 11080 Belgrade, Serbia; orcid.org/0000-0002-4101-1713

Milan Jocić – Institute of Physics Belgrade, University of Belgrade, 11080 Belgrade, Serbia

Vladimir Djoković — Department of Radiation Chemistry and Physics, "Vinča" Institute of Nuclear Sciences - National Institute of the Republic of Serbia and Center of Excellence for Photoconversion, "Vinča" Institute of Nuclear Sciences -National Institute of the Republic of Serbia, University of Belgrade, 11001 Belgrade, Serbia

Sylwia Ptasinska — Radiation Laboratory, University of Notre Dame, Notre Dame, Indiana 46556, United States; Department of Physics, University of Notre Dame, Notre Dame, Indiana 46556, United States; orcid.org/0000-0002-7550-8189

Complete contact information is available at: https://pubs.acs.org/10.1021/acs.jpcc.2c03208

#### Notes

The authors declare no competing financial interest.

#### ACKNOWLEDGMENTS

The authors acknowledge funding from the Ministry of Education, Science, and Technological Development of the Republic of Serbia. The authors are grateful for the support of the entire staff of the Synchrotron SOLEIL for smooth operation during beamtime no. 20190421. Numerical simulations were performed on the PARADOX supercomputing facility at the Scientific Computing Laboratory, National Center of Excellence for the Study of Complex Systems, Institute of Physics Belgrade. P.S. and S.P. acknowledge the US Department of Energy Office of Science, Office of Basic Energy Sciences under award number DE-FC02-04ER15533 (NDRL no. 5356).

#### REFERENCES

- (1) Milosavljević, A. R.; Božanić, D. K.; Sadhu, S.; Vukmirović, N.; Dojčilović, R.; Sapkota, P.; Huang, W.; Bozek, J.; Nicolas, C.; Nahon, L.; et al. Electronic Properties of Free-Standing Surfactant-Capped Lead Halide Perovskite Nanocrystals Isolated in Vacuo. *J. Phys. Chem. Lett.* **2018**, *9*, 3604–3611.
- (2) Mei, A.; Li, X.; Liu, L.; Ku, Z.; Liu, T.; Rong, Y.; Xu, M.; Hu, M.; Chen, J.; Yang, Y.; et al. A Hole-Conductor—Free, Fully Printable Mesoscopic Perovskite Solar Cell with High Stability. *Science* **2014**, 345, 295—298.
- (3) Leung, S.-F.; Ho, K.-T.; Kung, P.-K.; Hsiao, V. K. S.; Alshareef, H. N.; Wang, Z. L.; He, J.-H. A Self-Powered and Flexible Organometallic Halide Perovskite Photodetector with Very High Detectivity. *Adv. Mater.* **2018**, *30*, 1704611.
- (4) Chen, Q.; de Marco, N.; Yang, Y. M.; Song, T.-B.; Chen, C.-C.; Zhao, H.; Hong, Z.; Zhou, H.; Yang, Y. Under the Spotlight: The Organic-Inorganic Hybrid Halide Perovskite for Optoelectronic Applications. *Nano Today* **2015**, *10*, 355–396.
- (5) Yuan, M.; Quan, L. N.; Comin, R.; Walters, G.; Sabatini, R.; Voznyy, O.; Hoogland, S.; Zhao, Y.; Beauregard, E. M.; Kanjanaboos, P.; et al. Perovskite Energy Funnels for Efficient Light-Emitting Diodes. *Nat. Nanotechnol.* **2016**, *11*, 872–877.
- (6) Yang, W. S.; Park, B.-W.; Jung, E. H.; Jeon, N. J.; Kim, Y. C.; Lee, D. U.; Shin, S. S.; Seo, J.; Kim, E. K.; Noh, J. H.; Seok, S. I. Iodide Management in Formamidinium-Lead-Halide—Based Perovskite Layers for Efficient Solar Cells. *Science* 2017, 356, 1376—1379.
- (7) NREL. Best Research-Cell Efficiency Chart. https://www.nrel.gov/pv/cell-efficiency.html (accessedFebruary 2, 2022).
- (8) Brandt, R. E.; Stevanović, V.; Ginley, D. S.; Buonassisi, T. Identifying Defect-Tolerant Semiconductors with High Minority-Carrier Lifetimes: Beyond Hybrid Lead Halide Perovskites. MRS Commun. 2015, 5, 265–275.
- (9) Aristidou, N.; Sanchez-Molina, I.; Chotchuangchutchaval, T.; Brown, M.; Martinez, L.; Rath, T.; Haque, S. A. The Role of Oxygen in the Degradation of Methylammonium Lead Trihalide Perovskite Photoactive Layers. *Am. Ethnol.* **2015**, *127*, 8326–8330.
- (10) Habisreutinger, S. N.; Leijtens, T.; Eperon, G. E.; Stranks, S. D.; Nicholas, R. J.; Snaith, H. J. Carbon Nanotube/Polymer Composites as a Highly Stable Hole Collection Layer in Perovskite Solar Cells. *Nano Lett.* **2014**, *14*, 5561–5568.
- (11) Bag, M.; Renna, L. A.; Adhikari, R. Y.; Karak, S.; Liu, F.; Lahti, P. M.; Russell, T. P.; Tuominen, M. T.; Venkataraman, D. Kinetics of Ion Transport in Perovskite Active Layers and Its Implications for Active Layer Stability. *J. Am. Chem. Soc.* **2015**, *137*, 13130–13137.
- (12) Chaudhary, B.; Kulkarni, A.; Jena, A. K.; Ikegami, M.; Udagawa, Y.; Kunugita, H.; Ema, K.; Miyasaka, T. Poly(4-Vinylpyridine)-Based Interfacial Passivation to Enhance Voltage and Moisture Stability of Lead Halide Perovskite Solar Cells. *ChemSusChem* **2017**, *10*, 2473–2479
- (13) Milosavljević, A. R.; Huang, W.; Sadhu, S.; Ptasinska, S. Low-Energy Electron-Induced Transformations in Organolead Halide Perovskite. *Angew. Chem., Int. Ed.* **2016**, *55*, 10083–10087.
- (14) Babayigit, A.; Ethirajan, A.; Muller, M.; Conings, B. Toxicity of Organometal Halide Perovskite Solar Cells. *Nat. Mater.* **2016**, *15*, 247–251.
- (15) Turkevych, I.; Kazaoui, S.; Ito, E.; Urano, T.; Yamada, K.; Tomiyasu, H.; Yamagishi, H.; Kondo, M.; Aramaki, S. Photovoltaic Rudorffites: Lead-Free Silver Bismuth Halides Alternative to Hybrid Lead Halide Perovskites. *ChemSusChem* **2017**, *10*, 3754–3759.
- (16) Oh, J. T.; Kim, D. H.; Kim, Y. Solution-Processed "silver-Bismuth-Iodine" Ternary Thin Films for Lead-Free Photovoltaic Absorbers. *J. Visualized Exp.* **2018**, 2018, No. e58286.
- (17) Hosseini, S. S.; Adelifard, M.; Ataei, M. An Investigation on Physical Properties of  $Ag_2BiI_5$  Absorber Layers Synthesized by Microwave Assisted Spin Coating Technique. *J. Mater. Sci.: Mater. Electron.* **2019**, *30*, 5021–5029.
- (18) Jung, K. W.; Sohn, M. R.; Lee, H. M.; Yang, I. S.; Sung, S. D.; Kim, J.; Wei-Guang Diau, E.; Lee, W. I. Silver Bismuth Iodides in

- Various Compositions as Potential Pb-Free Light Absorbers for Hybrid Solar Cells. Sustainable Energy Fuels 2018, 2, 294–302.
- (19) Koedtruad, A.; Goto, M.; Amano Patino, M.; Tan, Z.; Guo, H.; Nakamura, T.; Handa, T.; Chen, W. T.; Chuang, Y. C.; Sheu, H. S.; et al. Structure-Property Relations in Ag—Bi—I Compounds: Potential Pb-Free Absorbers in Solar Cells. *J. Mater. Chem. A* **2019**, *7*, 5583–5588
- (20) Mashadieva, L. F.; Aliev, Z. S.; Shevelkov, A. V.; Babanly, M. B. Experimental Investigation of the Ag-Bi-I Ternary System and Thermodynamic Properties of the Ternary Phases. *J. Alloys Compd.* **2013**, *551*, 512–520.
- (21) Ghosh, B.; Wu, B.; Guo, X.; Harikesh, P. C.; John, R. A.; Baikie, T.; Wee, A. T.; Guet, C.; Sum, T. C.; et al. Superior Performance of Silver Bismuth Iodide Photovoltaics Fabricated via Dynamic Hot-Casting Method under Ambient Conditions. *Adv. Energy Mater.* **2018**, *8*, 1802051.
- (22) Lu, C.; Zhang, J.; Sun, H.; Hou, D.; Gan, X.; Shang, M. H.; Li, Y.; Hu, Z.; Zhu, Y.; Han, L. Inorganic and Lead-Free AgBiI4 Rudorffite for Stable Solar Cell Applications. *ACS Appl. Energy Mater.* **2018**, *1*, 4485–4492.
- (23) Sansom, H. C.; Whitehead, G. F. S.; Dyer, M. S.; Zanella, M.; Manning, T. D.; Pitcher, M. J.; Whittles, T. J.; Dhanak, V. R.; Alaria, J.; Claridge, J. B.; et al. AgBiI<sub>4</sub> as a Lead-Free Solar Absorber with Potential Application in Photovoltaics. *Chem. Mater.* **2017**, 29, 1538–1549.
- (24) Zhang, Q.; Wu, C.; Qi, X.; Lv, F.; Zhang, Z.; Liu, Y.; Wang, S.; Qu, B.; Chen, Z.; Xiao, L. Photovoltage Approaching 0.9 v for Planar Heterojunction Silver Bismuth Iodide Solar Cells with Li-TFSI Additive. ACS Appl. Energy Mater. 2019, 2, 3651–3656.
- (25) Zhu, H.; Pan, M.; Johansson, M. B.; Johansson, E. M. J. High Photon-to-Current Conversion in Solar Cells Based on Light-Absorbing Silver Bismuth Iodide. *ChemSusChem* **2017**, *10*, 2592–2596.
- (26) Iyoda, F.; Nishikubo, R.; Wakamiya, A.; Saeki, A. Ag-(Bi, Sb, In, Ga)-I Solar Cells: Impacts of Elemental Composition and Additives on the Charge Carrier Dynamics and Crystal Structures. *ACS Appl. Energy Mater.* **2020**, *3*, 8224–8232.
- (27) Danilović, D.; Božanić, D. K.; Dojčilović, R.; Vukmirović, N.; Sapkota, P.; Vukašinović, I.; Djoković, V.; Bozek, J.; Nicolas, C.; Ptasinska, S.; et al. Aerosol Synthesis and Gas-Phase Photoelectron Spectroscopy of Ag–Bi–I Nanosystems. *J. Phys. Chem. C* **2020**, 124, 23930–23937.
- (28) Li, X.; Traoré, B.; Kepenekian, M.; Li, L.; Stoumpos, C. C.; Guo, P.; Even, J.; Katan, C.; Kanatzidis, M. G. Bismuth/Silver-Based Two-Dimensional Iodide Double and One-Dimensional Bi Perovskites: Interplay between Structural and Electronic Dimensions. *Chem. Mater.* **2021**, 33, 6206–6216.
- (29) Tyagi, P.; Arveson, S. M.; Tisdale, W. A. Colloidal Organohalide Perovskite Nanoplatelets Exhibiting Quantum Confinement. *J. Phys. Chem. Lett.* **2015**, *6*, 1911–1916.
- (30) Huang, C.; Gao, Y.; Wang, S.; Zhang, C.; Yi, N.; Xiao, S.; Song, Q. Giant Blueshifts of Excitonic Resonances in Two-Dimensional Lead Halide Perovskite. *Nano Energy* **2017**, *41*, 320–326.
- (31) Ding, Y.-F.; Zhao, Q.-Q.; Yu, Z.-L.; Zhao, Y.-Q.; Liu, B.; He, P.-B.; Zhou, H.; Li, K.; Yin, S.-F.; Cai, M.-Q. Strong Thickness-Dependent Quantum Confinement in All-Inorganic Perovskite Cs<sub>2</sub>PbI<sub>4</sub> with a Ruddlesden–Popper Structure. *J. Mater. Chem. C* **2019**, *7*, 7433–7441.
- (32) Connor, B. A.; Leppert, L.; Smith, M. D.; Neaton, J. B.; Karunadasa, H. I. Layered Halide Double Perovskites: Dimensional Reduction of  $Cs_2AgBiBr_6$ . J. Am. Chem. Soc. **2018**, 140, 5235–5240.
- (33) Gelmetti, I.; Cabau, L.; Montcada, N. F.; Palomares, E. Selective Organic Contacts for Methyl Ammonium Lead Iodide (MAPI) Perovskite Solar Cells: Influence of Layer Thickness on Carriers Extraction and Carriers Lifetime. ACS Appl. Mater. Interfaces 2017, 9, 21599–21605.
- (34) Bekenstein, Y.; Dahl, J. C.; Huang, J.; Osowiecki, W. T.; Swabeck, J. K.; Chan, E. M.; Yang, P.; Alivisatos, A. P. The Making and Breaking of Lead-Free Double Perovskite Nanocrystals of Cesium

- Silver-Bismuth Halide Compositions. Nano Lett. 2018, 18, 3502-3508.
- (35) Tan, Z.; Wu, Y.; Hong, H.; Yin, J.; Zhang, J.; Lin, L.; Wang, M.; Sun, X.; Sun, L.; Huang, Y.; et al. Two-Dimensional (C<sub>4</sub>H<sub>9</sub>NH<sub>3</sub>)<sub>2</sub>PbBr<sub>4</sub> Perovskite Crystals for High-Performance Photodetector. *J. Am. Chem. Soc.* **2016**, *138*, 16612–16615.
- (36) Creutz, S. E.; Crites, E. N.; de Siena, M. C.; Gamelin, D. R. Colloidal Nanocrystals of Lead-Free Double-Perovskite (Elpasolite) Semiconductors: Synthesis and Anion Exchange To Access New Materials. *Nano Lett.* **2018**, *18*, 1118–1123.
- (37) Pal, J.; Bhunia, A.; Chakraborty, S.; Manna, S.; Das, S.; Dewan, A.; Datta, S.; Nag, A. Synthesis and Optical Properties of Colloidal M3Bi2I9 (M = Cs, Rb) Perovskite Nanocrystals. *J. Phys. Chem. C* **2018**, *122*, 10643–10649.
- (38) Brus, L. E. Electron-Electron and Electron-Hole Interactions in Small Semiconductor Crystallites: The Size Dependence of the Lowest Excited Electronic State. *Chem. Phys.* **1984**, *80*, 4403–4409.
- (39) Sandroff, C. J.; Kelty, S. P.; Hwang, D. M. Clusters in Solution: Growth and Optical Properties of Layered Semiconductors with Hexagonal and Honeycombed Structures. *Chem. Phys.* **1986**, *85*, 5337–5340.
- (40) Micic, O. I.; Nenadovic, M. T.; Peterson, M. W.; Nozik, A. J. Size Quantization in Layered Semiconductor Colloids with Tetrahedral Bonding: Mercury Diiodide. *J. Phys. Chem.* **1987**, *91*, 1295–1297.
- (41) Micic, O. I.; Li, Z.; Mills, G.; Sullivan, J. C.; Meisel, D. Formation of Small Particles of Lead Iodide, Mercuric Iodide, and Bismuth Iodide Layered Semiconductors. *J. Phys. Chem.* **1987**, *91*, 6221–6229.
- (42) Liu, Z.; Yang, H.; Wang, J.; Yuan, Y.; Hills-Kimball, K.; Cai, T.; Wang, P.; Tang, A.; Chen, O. Synthesis of Lead-Free  $Cs_2AgBix_6$  (X = Cl, Br, I) Double Perovskite Nanoplatelets and Their Application in CO<sub>2</sub> Photocatalytic Reduction. *Nano Lett.* **2021**, 21, 1620–1627.
- (43) Božanić, D. K.; Garcia, G. A.; Sublemontier, O.; Pajović, J.; Djoković, V.; Nahon, L. Velocity Map Imaging VUV Angle-Resolved Photoemission on Isolated Nanosystems: Case of Gold Nanoparticles. *J. Phys. Chem. C* **2020**, *124*, 24500–24512.
- (44) Perdew, J. P.; Burke, K.; Ernzerhof, M. Generalized Gradient Approximation Made Simple. *Phys. Rev. Lett.* **1996**, 77, 3865–3868.
- (45) van Setten, M. J.; Giantomassi, M.; Bousquet, E.; Verstraete, M. J.; Hamann, D. R.; Gonze, X.; Rignanese, G.-M. The PseudoDojo: Training and Grading a 85 Element Optimized Norm-Conserving Pseudopotential Table. *Comput. Phys. Commun.* **2018**, 226, 39–54.
- (46) Hamann, D. R. Optimized Norm-Conserving Vanderbilt Pseudopotentials. *Phys. Rev. B* **2013**, *88*, 085117.
- (47) Giannozzi, P.; Andreussi, O.; Brumme, T.; Bunau, O.; Buongiorno Nardelli, M.; Calandra, M.; Car, R.; Cavazzoni, C.; Ceresoli, D.; Cococcioni, M.; et al. Advanced Capabilities for Materials Modelling with Quantum ESPRESSO. J. Phys.: Condens. Matter 2017, 29, 465901.
- (48) Garrity, K. F.; Bennett, J. W.; Rabe, K. M.; Vanderbilt, D. Pseudopotentials for High-Throughput DFT Calculations. *Comput. Mater. Sci.* **2014**, *81*, 446–452.
- (49) Perdew, J. P. Density Functional Theory and the Band Gap Problem. *Int. J. Quantum Chem.* **1985**, 28, 497–523.
- (50) Perdew, J. P.; Ernzerhof, M.; Burke, K. Rationale for Mixing Exact Exchange with Density Functional Approximations. *J. Chem. Phys.* **1996**, *105*, 9982–9985.
- (51) Adamo, C.; Barone, V. Toward Reliable Density Functional Methods without Adjustable Parameters: The PBE0 Model. *J. Chem. Phys.* **1999**, *110*, 6158–6170.
- (52) Chen, W.; Pasquarello, A. Band-Edge Levels in Semiconductors and Insulators: Hybrid Density Functional Theory versus Many-Body Perturbation Theory. *Phys. Rev. B* **2012**, *86*, No. 035134.
- (53) Steiner, K.; Chen, W.; Pasquarello, A. Band Offsets of Lattice-Matched Semiconductor Heterojunctions through Hybrid Functionals and G0W0. *Phys. Rev. B* **2014**, *89*, 205309.
- (54) Lin, L. Adaptively Compressed Exchange Operator. J. Chem. Theory Comput. 2016, 12, 2242–2249.

- (55) Jocić, M.; Vukmirović, N. Ab Initio Construction of Symmetry-Adapted k · p Hamiltonians for the Electronic Structure of Semiconductors. *Phys. Rev. B* **2020**, *102*, 085121.
- (56) Oldag, T.; Aussieker, T.; Keller, H. L.; Preitschaft, C.; Pfitzner, A. Solvothermale Synthese Und Bestimmung Der Kristallstrukturen von AgBiI<sub>4</sub> Und Ag<sub>3</sub>BiI<sub>6</sub>. Z. Anorg. Allg. Chem. **2005**, 631, 677–682.
- (57) Prasad, M. D.; Krishna, M. G.; Batabyal, S. K. Silver Bismuth Iodide Nanomaterials as Lead-Free Perovskite for Visible Light Photodetection. *ACS Appl. Nano Mater.* **2021**, *4*, 1252–1259.
- (58) Crovetto, A.; Hajijafarassar, A.; Hansen, O.; Seger, B.; Chorkendorff, I.; Vesborg, P. C. K. Parallel Evaluation of the Bil3, BiOI, and Ag3Bil6Layered Photoabsorbers. *Chem. Mater.* **2020**, 32, 3385–3395.
- (59) Sengupta, A.; Mandal, K. C.; Zhang, J. Z. Ultrafast Electronic Relaxation Dynamics in Layered Iodide Semiconductors: A Comparative Study of Colloidal BiI<sub>3</sub> and PbI<sub>2</sub> Nanoparticles. *J. Phys. Chem. B* **2000**, *104*, 9396–9403.
- (60) Gaarenstroom, S. W.; Winograd, N. Initial and Final State Effects in the ESCA Spectra of Cadmium and Silver Oxides. *J. Chem. Phys.* **1977**, *67*, 3500–3506.
- (61) Khazaee, M.; Sardashti, K.; Chung, C. C.; Sun, J. P.; Zhou, H.; Bergmann, E.; Dunlap-Shohl, W. A.; Han, Q.; Hill, I. G.; Jones, J. L.; et al. Dual-Source Evaporation of Silver Bismuth Iodide Films for Planar Junction Solar Cells. *J. Mater. Chem. A* **2019**, *7*, 2095–2105.
- (62) Qiu, W.; Dudder, G. J.; Zhao, X.; Perry, S. S.; Nino, J. C. Interfacial Reactivity of Au, Pd, and Pt on BiI <sub>3</sub> (001): Implications for Electrode Selection. *ACS Appl. Mater. Interfaces* **2011**, 3, 1910–1917.
- (63) Ferfolja, K.; Valant, M.; Mikulska, I.; Gardonio, S.; Fanetti, M. Chemical Instability of an Interface between Silver and Bi  $_2$  Se  $_3$  Topological Insulator at Room Temperature. *J. Phys. Chem. C* **2018**, 122, 9980–9984.
- (64) Pignié, M.-C.; Patra, S.; Huart, L.; Milosavljević, A. R.; Renault, J. P.; Leroy, J.; Nicolas, C.; Sublemontier, O.; le Caër, S.; Thill, A. Experimental Determination of the Curvature-Induced Intra-Wall Polarization of Inorganic Nanotubes. *Nanoscale* **2021**, *13*, 19650–19662
- (65) Schürmann, R.; Titov, E.; Ebel, K.; Kogikoski, S.; Mostafa, A.; Saalfrank, P.; Milosavljević, A. R.; Bald, I. The Electronic Structure of the Metal-Organic Interface of Isolated Ligand Coated Gold Nanoparticles. *Nanoscale Adv.* **2022**, *4*, 1599–1607.
- (66) Premkumar, S.; Liu, D.; Zhang, Y.; Nataraj, D.; Ramya, S.; Jin, Z.; Mamba, B. B.; Kuvarega, A. T.; Gui, J. Stable Lead-Free Silver Bismuth Iodide Perovskite Quantum Dots for UV Photodetection. *ACS Appl. Nano Mater.* **2020**, *3*, 9141–9150.
- (67) Hinuma, Y.; Pizzi, G.; Kumagai, Y.; Oba, F.; Tanaka, I. Band Structure Diagram Paths Based on Crystallography. *Comput. Mater. Sci.* **2017**, *128*, 140–184.

## PHYSICAL REVIEW B

Articles Published in AUGUST 2020 15(II)

covering condensed matter and materials physics

Published by
AMERICAN PHYSICAL SOCIETY™



Volume 102 Third Series Number 8

#### Ab initio construction of symmetry-adapted k · p Hamiltonians for the electronic structure of semiconductors

Milan Jocić\* and Nenad Vukmirović p† Institute of Physics Belgrade, University of Belgrade, Pregrevica 118, 11080 Belgrade, Serbia

(Received 30 April 2020; revised 26 June 2020; accepted 27 July 2020; published 11 August 2020)

While  $\mathbf{k} \cdot \mathbf{p}$  Hamiltonians are frequently used for the description of electronic states in quantum nanostructures, a method is lacking to obtain them in their symmetrized form directly from ab initio band structure calculations of bulk material. We developed a method for obtaining the parameters and the symmetry-adapted form of the  $\mathbf{k} \cdot \mathbf{p}$  Hamiltonian from the output of an *ab initio* band structure calculation. The method consists of (i) evaluation of momentum matrix elements between the wave functions obtained from band structure calculation; (ii) identification of the unitary transformation that transforms these wave functions to the symmetryadapted basis; (iii) transformation of the  $\mathbf{k} \cdot \mathbf{p}$  Hamiltonian to the symmetry-adapted basis. We illustrate the methodology by obtaining  $\mathbf{k} \cdot \mathbf{p}$  Hamiltonians that describe the band structure of zinc-blende CdSe and then we use the Hamiltonians obtained to calculate the electronic states in CdSe quantum wells. Excellent agreement between density functional theory and  $\mathbf{k} \cdot \mathbf{p}$  is obtained for the electronic structure, even for quite thin wells.

DOI: 10.1103/PhysRevB.102.085121

#### I. INTRODUCTION

Semiconductor materials and nanostructures based upon them are at the heart of the operation of almost all electronic and optical devices. For this reason, there is a significant interest in understanding the electronic states in these materials. The progress in developments of methodologies for ab initio electronic structure calculations has led us to the point where it is relatively straightforward to perform band structure calculations of bulk semiconducting materials. Density functional theory (DFT) calculations based on local or semilocal approximations for the exchange-correlation functional give band gaps that are significantly smaller than experimental band gaps [1]. However, improved treatments based on the use of hybrid functionals [2,3] or many body perturbation theory in GW (where G stands for the Green's function and W for screened Coulomb interaction) approximation [4] give rather accurate band gaps and band structure of the bulk material [5–7]. On the other hand, it is rather difficult to perform ab initio calculations of semiconductor nanostructures because the calculation needs to be performed for a supercell containing a very large number of atoms.

The method that proved to be both practical and successful in treating the electronic states in semiconductor nanostructures is the  $\mathbf{k} \cdot \mathbf{p}$  method [8–11]. It is based on the representation of the single-particle wave function in terms of Bloch functions of the bulk material at a certain point in the Brillouin zone (typically the  $\Gamma$  point) and slowly varying envelope functions. The  $\mathbf{k} \cdot \mathbf{p}$  Hamiltonian for a nanostructure is then an operator that acts on the column of envelope functions corresponding to each of the bulk bands.

Despite the success in using the  $\mathbf{k} \cdot \mathbf{p}$  method for description of bulk band structure around a certain point in the Brillouin zone (usually the  $\Gamma$  point) and for treating the semiconductor nanostructures, there is still no systematic way to construct the  $\mathbf{k} \cdot \mathbf{p}$  Hamiltonian for a given material and obtain the parameters of the Hamiltonian. The parameters of most conventional  $\mathbf{k} \cdot \mathbf{p}$  Hamiltonians (such as the eight-band Hamiltonian [10,12,13]) for a few most common classes of semiconductors can be found in the literature [14,15] and were obtained from the band gap and effective masses in the valence and conduction band. Parameters of  $\mathbf{k} \cdot \mathbf{p}$  Hamiltonians with larger number of bands (such as, for example, the 30-band Hamiltonian [16-20]) and recently introduced atomistic  $\mathbf{k} \cdot \mathbf{p}$  [21] are typically obtained by fitting to the calculated band structure of the material or to experimental data. However, given a relatively large number of fitting parameters, it is questionable if the fit gives unique parameters. It is also not clear what part of the Brillouin zone should be used in the fitting procedure, since it is not expected that the  $\mathbf{k} \cdot \mathbf{p}$  method describes the bulk band structure throughout the whole Brillouin zone.

Given the fact that new classes of semiconductor materials and nanostructures based upon them emerge or find new applications quite often, it would be of significant interest to develop the procedure for construction of desired  $\mathbf{k} \cdot \mathbf{p}$ Hamiltonians. Since all parameters of the  $\mathbf{k} \cdot \mathbf{p}$  Hamiltonian are related to momentum matrix elements between singleparticle wave functions of the bulk, it is in principle possible to obtain them from electronic structure calculation of the bulk material. This is indeed done when  $\mathbf{k} \cdot \mathbf{p}$  is used as a method for interpolation of ab initio calculated band structure to a more dense grid of k points [22-25]. However, there is a certain shortcoming of this approach when it comes to the construction of  $\mathbf{k} \cdot \mathbf{p}$  Hamiltonians that should be used in future applications. Namely, due to the symmetry of the

<sup>\*</sup>milan.jocic@ipb.ac.rs

<sup>†</sup>nenad.vukmirovic@ipb.ac.rs

crystalline material the energy levels in characteristic points in the Brillouin zone are degenerate and for this reason the choice of Bloch wave functions from the Hilbert space spanned by the degenerate states is not unique. As a consequence, one may end up with different forms of the final  $\mathbf{k} \cdot \mathbf{p}$  Hamiltonian depending on the particular choice of Bloch functions from this space. The number of Hamiltonian parameters in these forms might be significantly larger than the true number of parameters imposed by the symmetry of the crystal.

In this work, we develop the procedure for construction of the  $\mathbf{k} \cdot \mathbf{p}$  Hamiltonian in the symmetrized form with a minimal number of parameters imposed by crystal symmetry. In Sec. II we give a brief overview of the  $\mathbf{k} \cdot \mathbf{p}$  method and present our approach for the construction of the Hamiltonian. In Sec. III we illustrate the method by applying it to bulk zinc-blende CdSe and to CdSe quantum wells.

#### II. THEORETICAL APPROACH

#### A. $k \cdot p$ equation

We start this section by briefly reviewing the  $\mathbf{k} \cdot \mathbf{p}$  method to set the stage for description of our procedure for construction of  $\mathbf{k} \cdot \mathbf{p}$  Hamiltonian. We start with the equation for an electron in the periodic crystal that reads

$$\left[\frac{p^2}{2m_0} + U + T_{\rm rk} + H_{\rm D} + H_{\rm soc}\right] |\Psi_{n\mathbf{k}}\rangle = E_n(\mathbf{k}) |\Psi_{n\mathbf{k}}\rangle, \quad (1)$$

where  $p^2/(2m_0) = -\hbar^2 \nabla^2/(2m_0)$  is the kinetic energy operator and  $m_0$  is the free electron mass, U is the periodic crystal potential (including nuclei, core and valence electrons), while  $E_n(\mathbf{k})$  and  $|\Psi_{n\mathbf{k}}\rangle$  are the corresponding energy and wave function for the electron in band n at wave vector  $\mathbf{k}$  in the Brillouin zone. When the effects of spin-orbit interaction are included,  $|\Psi_{n\mathbf{k}}\rangle$  is a two-component spinor. The last three terms in brackets are the relativistic corrections accounting for kinetic energy  $T_{r\mathbf{k}} = -p^4/(8m_0^3c^2)$ , fine structure through the Darwin term  $H_D = \hbar^2 \nabla \cdot \nabla U/(8m_0^2c^2)$  and spin-orbit coupling (SOC)  $H_{\text{soc}} = \hbar(\sigma \times \nabla U) \cdot \mathbf{p}/(4m_0^2c^2)$ , where  $\sigma = (\sigma_x, \sigma_y, \sigma_z)$  denotes a vector with Pauli matrices as its components.

For an electron in a periodic potential, the Bloch theorem holds, by which the components of  $|\Psi_{nk}\rangle$  are of the form

$$\Psi_{\mathbf{n}\mathbf{k}}^{(a)}(\mathbf{r}) = e^{i\mathbf{k}\cdot\mathbf{r}} u_{\mathbf{n}\mathbf{k}}^{(a)}(\mathbf{r}), \tag{2}$$

where  $u_{n\mathbf{k}}^{(a)}(\mathbf{r})$  are periodic Bloch functions satisfying the condition  $u_{n\mathbf{k}}^{(a)}(\mathbf{r}+\mathbf{R})=u_{n\mathbf{k}}^{(a)}(\mathbf{r})$ , with **R** being the direct lattice vector. Inserting Eq. (2) into Eq. (1), we obtain the one-electron equation in terms of periodic Bloch functions:

$$\left[H + \frac{\hbar^2 k^2}{2m_0} + T'_{\rm rk}(\mathbf{k}) + \frac{\hbar \mathbf{k} \cdot \mathbf{p}_{\rm soc}}{m_0}\right] |u_{n\mathbf{k}}\rangle = E_n(\mathbf{k}) |u_{n\mathbf{k}}\rangle, \quad (3)$$

where  $H=p^2/(2m_0)+U+T_{\rm rk}+H_{\rm D}+H_{\rm soc}$  is the initial Hamiltonian from Eq. (1),  ${\bf p}_{\rm soc}={\bf p}+\hbar(\sigma\times\nabla U)/(4m_0c^2)$  is the momentum modified with the SOC part and  $T_{\rm rk}'({\bf k})$  is given

$$T_{\text{rk}}'(\mathbf{k}) = -\frac{1}{8m_0^3c^2} [4(\hbar\mathbf{k}\cdot\mathbf{p})p^2 + 4(\hbar\mathbf{k}\cdot\mathbf{p})^2 + 4(\hbar\mathbf{k})^2(\hbar\mathbf{k}\cdot\mathbf{p}) + 2(\hbar k)^2p^2 + (\hbar k)^4].$$
(4)

We further express  $|u_{a\mathbf{k}}\rangle$  in the basis of orthonormal functions  $|u_{m\mathbf{k}\alpha}\rangle$ :

$$|u_{a\mathbf{k}}\rangle = \sum_{m} B_{m}^{(a)}(\mathbf{k})|u_{m\mathbf{k}_{0}}\rangle,$$
 (5)

which are solutions of eigenproblem given by Eq. (3) at a certain  $\mathbf{k}_0$  with eigenvalues  $E_n(\mathbf{k}_0)$ . Inserting Eq. (5) into Eq. (3), multiplying from the left by  $\langle u_{n\mathbf{k}_0}|$  and exploiting the orthonormality condition we arrive at the equation

$$\sum_{m} \left[ \left( E_{n}(\mathbf{k}_{0}) + \frac{\hbar^{2}(k^{2} - k_{0}^{2})}{2m_{0}} \right) \delta_{nm} + \frac{\hbar(\mathbf{k} - \mathbf{k}_{0})}{m_{0}} \cdot \langle u_{n\mathbf{k}_{0}} | \mathbf{p} | u_{m\mathbf{k}_{0}} \rangle \right] B_{m}^{(a)}(\mathbf{k})$$

$$= E^{(a)}(\mathbf{k}) B_{n}^{(a)}(\mathbf{k}). \tag{6}$$

We have omitted  $T'_{rk}(\mathbf{k}, \mathbf{k}_0)$  that would appear in Eq. (6) because its contribution depends directly on the distance between  $\mathbf{k}$  and  $\mathbf{k}_0$  and becomes significant at distances far greater than the one where  $\mathbf{k} \cdot \mathbf{p}$  theory is applicable. We have performed a numerical check of this claim in case of zincblende CdSe and we have shown that the influence of this term on bulk eigenenergies is smaller than 0.3 meV throughout the whole Brillouin zone. For similar reasons, we neglected SOC modification to momentum (i.e., we take  $\mathbf{p}_{soc} \approx \mathbf{p}$ ). We note that SOC is fully included in our approach unlike in many theoretical treatments where it is treated as a perturbation. We further rewrite Eq. (6) in somewhat more convenient form by exploiting the relation

$$\langle \Psi_{n\mathbf{k}_0} | \mathbf{p} | \Psi_{m\mathbf{k}_0} \rangle = \hbar \mathbf{k} \delta_{nm} + \langle u_{n\mathbf{k}_0} | \mathbf{p} | u_{m\mathbf{k}_0} \rangle. \tag{7}$$

We then obtain

$$\sum_{m} \left[ \left( E_{n}(\mathbf{k}_{0}) + \frac{\hbar^{2}(\mathbf{k} - \mathbf{k}_{0})^{2}}{2m_{0}} \right) \delta_{nm} + \frac{\hbar(\mathbf{k} - \mathbf{k}_{0})}{m_{0}} \cdot \langle \Psi_{n\mathbf{k}_{0}} | \mathbf{p} | \Psi_{m\mathbf{k}_{0}} \rangle \right] B_{m}^{(a)}(\mathbf{k})$$

$$= E^{(a)}(\mathbf{k}) B_{n}^{(a)}(\mathbf{k}), \tag{8}$$

which takes the form of an eigenproblem:

$$\sum_{m} H_{nm}^{(1)} B_{m}^{(a)} = E^{(a)} B_{n}^{(a)}, \tag{9}$$

where  $H_{nm}^{(1)}$  is given by the term in square brackets in Eq. (8). The indices m and n in Eq. (9) go over the bands that were included in the expansion in Eq. (5). The accuracy of  $\mathbf{k} \cdot \mathbf{p}$  Hamiltonian can further be improved by adding the effect of remote bands [the bands not included in the expansion in Eq. (5)] perturbatively using the Löwdin's perturbation theory [11,26]. This yields additional term in the  $\mathbf{k} \cdot \mathbf{p}$  Hamiltonian which reads

$$H_{nm}^{(2)} = \frac{\hbar^2}{m_0^2} \sum_{l} \frac{\langle u_{n\mathbf{k}_0} | \mathbf{K} \cdot \mathbf{p} | u_{l\mathbf{k}_0} \rangle \langle u_{l\mathbf{k}_0} | \mathbf{K} \cdot \mathbf{p} | u_{m\mathbf{k}_0} \rangle}{[E_n(\mathbf{k}_0) + E_m(\mathbf{k}_0)]/2 - E_l(\mathbf{k}_0)}, \quad (10)$$

with  $\mathbf{K} = \mathbf{k} - \mathbf{k}_0$  and the summation goes over the bands l that were not included in the expansion in Eq. (5).

#### B. Construction of symmetrized k · p Hamiltonian

The expression (8) can be, in principle, used to construct the  $\mathbf{k} \cdot \mathbf{p}$  Hamiltonian directly from ab initio calculation of band structure of bulk. Namely, all Hamiltonian matrix elements can be calculated from band energies  $E_n(\mathbf{k}_0)$  at point  $\mathbf{k}_0$  and momentum matrix elements  $\langle \Psi_{n\mathbf{k}_0} | \mathbf{p} | \Psi_{m\mathbf{k}_0} \rangle$  between the wave functions at  $\mathbf{k}_0$ . However, an issue arises regarding the uniqueness of the constructed Hamiltonian matrix as a consequence of the fact that some of the eigenstates  $|\Psi_{n\mathbf{k}_0}\rangle$ are degenerate. A typical choice for the  $\mathbf{k}_0$  point is some high symmetry point where band dispersions exhibit minima or maxima (such as for example the  $\Gamma$  point) and the group  $G_{\mathbf{k}_0}$ of the wave vector  $\mathbf{k}_0$  is some high symmetry point group. For this reason, there is a degeneracy between the eigenstates at  $\mathbf{k}_0$ , where the degree of degeneracy is determined by the dimensions of irreducible representations (irreps) of the group  $G_{\mathbf{k}_0}$  corresponding to each of the states. For example, in the case of zinc-blende CdSe material used as an example in this work, the top valence band is threefold degenerate and the bottom conduction band is nondegenerate when spin degrees of freedom are not taken into account and the effect of spinorbit interaction is not included. When spin-orbit interaction is included, the bottom conduction band is twofold degenerate, while two top valence bands are twofold and fourfold degenerate.

Let d be the degeneracy of the set of eigenstates  $|\phi_1\rangle, |\phi_2\rangle, \ldots, |\phi_d\rangle$  at  $\mathbf{k}_0$  at let  $\mathcal{H}_d$  be the Hilbert space spanned by these states. The states  $|\phi_1\rangle, |\phi_2\rangle, \ldots, |\phi_d\rangle$  form an orthonormal basis of  $\mathcal{H}_d$  but any other orthonormal basis may well have been chosen. With the use of different basis, the momentum matrix elements in Eq. (8) would be different and the  $\mathbf{k} \cdot \mathbf{p}$  Hamiltonian would have a different form. Moreover, it might even appear that the Hamiltonian has a different number of parameters. Our goal is to overcome this issue by fixing the choice of the degenerate states and obtaining the  $\mathbf{k} \cdot \mathbf{p}$  Hamiltonian in the form where it has a minimal number of parameters imposed by the symmetry group  $G_{\mathbf{k}_0}$  of the wave vector  $\mathbf{k}_0$ .

The set  $|\phi_1\rangle$ ,  $|\phi_2\rangle$ , ...,  $|\phi_d\rangle$  is obtained from DFT and they form  $d \times d$  matrices  $\Gamma(g)$  of the irrep of group  $G_{\mathbf{k}_0}$  that are given as

$$\Gamma_{mn}(g) = \langle \phi_m | P(g) | \phi_n \rangle, \tag{11}$$

where g is an element of the group  $G_{\mathbf{k}_0}$  and P(g) is the operator that applies the symmetry operation g on the given wave function. The matrices  $\Gamma(g)$  are then obtained by directly calculating the matrix elements in Eq. (11). We then calculate the characters of  $\Gamma$  to match it with one of the equivalent conventional irreps  $\Gamma'$  of the point group  $G_{\mathbf{k}_0}$ . The matrices of irreps  $\Gamma'$  can be found in databases of irreps of point groups, for example in Bilbao crystallographic data server [27]. The matrices  $\Gamma(g)$  and  $\Gamma'(g)$  are connected via a unitary transformation

$$U^{\dagger}\Gamma(g)U = \Gamma'(g), \tag{12}$$

which is satisfied for each  $g \in G_{\mathbf{k}_0}$ . Therefore, to obtain the basis of states in  $\mathcal{H}_d$  which is adapted to conventional matrices  $\Gamma'(g)$  in databases of irreps, one has to make a unitary

transformation of the basis

$$|\psi_j\rangle = \sum_{i=1}^d U_{ij} |\phi_i\rangle. \tag{13}$$

Now, the representation of the operator P(g) from Eq. (11) in the new basis set  $|\psi_j\rangle$  is the conventional representation  $\Gamma'$ . In the  $|\psi_j\rangle$  basis, the  $\mathbf{k} \cdot \mathbf{p}$  Hamiltonian has a convenient, symmetry-adapted form, in which relevant parameters of the Hamiltonian can be straightforwardly identified.

It remains to define a procedure for obtaining the unitary matrix U that connects the two representations  $\Gamma$  and  $\Gamma'$ . Such a procedure has recently been developed in Ref. [28] and we outline it here. One first obtains a set of coefficients  $r_{ab}$  as

$$r_{ab} = \sqrt{\frac{n_{\Gamma}}{|G|}} \left( \sum_{g \in G} \Gamma_{aa}(g) \Gamma'_{bb}(g^{-1}) \right)^{1/2}, \tag{14}$$

where  $\Gamma_{aa}(g)$  and  $\Gamma'_{bb}(g^{-1})$  are known matrix elements for symmetry operation (group element) g and its inverse  $g^{-1}$ , respectively, |G| is the order of group G while  $n_{\Gamma}$  is the dimension of representations  $\Gamma$  and  $\Gamma'$ . Then, one chooses the pair (a,b) for which  $r_{ab} > 0$ . The existence of such a pair has been proven in Ref. [28]. The matrix U is then given as

$$U_{ij} = \frac{1}{r_{ab}} \frac{n_{\Gamma}}{|G|} \sum_{g \in G} \Gamma_{ia}(g^{-1}) \Gamma'_{bj}(g).$$
 (15)

With this, we complete our procedure for construction of symmetrized  $\mathbf{k} \cdot \mathbf{p}$  Hamiltonian. For clarity, we review all steps of the procedure here:

- (i) Perform *ab initio* calculation of band structure for bulk, using DFT with local functionals, hybrid functional DFT, or by including quasiparticle energy correction within the GW approximation.
- (ii) Choose the point  $\mathbf{k}_0$  in the Brillouin zone, that is most suited for  $\mathbf{k} \cdot \mathbf{p}$  expansion and extract band energies  $E_n(\mathbf{k}_0)$  and their eigenstates  $|\Psi_{n\mathbf{k}_0}\rangle$  from desired *ab initio* method.
- (iii) Identify the groups of degenerate states at  $\mathbf{k}_0$  and the symmetry point group  $G_{\mathbf{k}_0}$ . Select the groups of degenerate states (usually those around the gap) that will form the  $\mathbf{k} \cdot \mathbf{p}$  Hamiltonian. Extract these groups of degenerate states  $|\phi_i\rangle$  from *ab initio* eigenstates  $|\Psi_{n\mathbf{k}_0}\rangle$ .
- (iv) For each of selected groups of degenerate states calculate the matrices  $\Gamma(g)$  of corresponding irrep  $\Gamma$  using Eq. (11). Using characters of  $\Gamma(g)$ , match  $\Gamma$  to the equivalent conventional representation  $\Gamma'$  found in databases of irreps of point groups.
- (v) For each of selected groups of degenerate states, calculate the unitary matrices U using sets of matrices  $\Gamma(g)$  and  $\Gamma'(g)$  as inputs for Eqs. (14) and (15).
- (vi) Proceed with calculation of the new, symmetry-adapted basis, consisting of selected groups of degenerate states  $|\psi_j\rangle$  using matrices U, obtained from the previous step, and corresponding groups of degenerate states  $|\phi_i\rangle$  with Eq. (13).
- (vii) Evaluate the momentum matrix elements in the new basis using Eqs. (7) (8), (9), and (10) which then

give all parameters of the symmetrized  $\mathbf{k} \cdot \mathbf{p}$  Hamiltonian  $H_{nm} = H_{nm}^{(1)} + H_{nm}^{(2)}$ .

It is important to note that these steps constitute a well-defined and straightforward procedure that gives the desired  $\mathbf{k} \cdot \mathbf{p}$  Hamiltonian starting from output of an *ab initio* calculation. It does not involve any kind of fitting which would introduce certain arbitrariness.

Next, we discuss the form of the Hamiltonian that we obtain and its relation to the form of the Hamiltonian that would be obtained using Luttinger's method of invariants [11,29]. The form of the Hamiltonian that we obtain consists of blocks  $\mathcal{B}(\Gamma_a', \Gamma_b')$ , where each block originates from two groups of states: the states  $|\psi_1^{(a)}\rangle, \ldots, |\psi_{d_a}^{(a)}\rangle$  that transform in accordance with the representation  $\Gamma_a'$  of dimension  $d_a$  and the states  $|\psi_1^{(b)}\rangle, \ldots, |\psi_{d_b}^{(b)}\rangle$  that transform in accordance with the representation  $\Gamma_b'$  of dimension  $d_b$ . The Hamiltonian consists of the terms quadratic in electronic momentum K, the terms linear in K and the terms that do not contain K. Luttinger's method of invariants [11,29] gives a systematic way to obtain the form of each  $\mathcal{B}(\Gamma_a', \Gamma_b')$  for terms of given order in K. For this reason, our procedure yields the same form of the Hamiltonian as Luttinger's method of invariants applied to obtain the terms up to second order in K. By its construction, Luttinger's method fully exploits the point group symmetry and yields the Hamiltonian in the form where a minimal number of parameters appears. On the other hand, it is clear that Luttinger's method cannot give the values of these parameters, since it exploits the symmetry of the system only and does not consider other details of the system. Our procedure in some sense links Luttinger's method from 1950's to modern ab initio calculations as it enables to obtain the form of the Hamiltonian that would be obtained using Luttinger's method and additionally gives the values of these parameters starting from ab initio wave functions and energies.

In Sec. III we apply our procedure to zinc-blende CdSe crystal whose point group at the  $\Gamma$  point is the  $T_d$  group. However, we note that our procedure is by no means limited to this particular crystal symmetry. It can be used for crystals of any kind of symmetry, at any point  $\mathbf{k}_0$  in the Brillouin zone. Of course, benefits of this method will be greater if the symmetry point group  $G_{\mathbf{k}_0}$  at  $\mathbf{k}_0$  is of higher order. Having a symmetry-adapted form of the Hamiltonian also gives great advantage when it comes to calculation of nanostructures. Numerical codes for calculating nanostructures using  $\mathbf{k} \cdot \mathbf{p}$  Hamiltonians could be easily adapted to another material of the same symmetry by just changing the numerical values of the parameters, that can be straightforwardly obtained using *ab initio* calculation for bulk material and the procedure described in the paper.

Finally, we briefly discuss on the conventions for matrices of the representations  $\Gamma'$ . In all examples in this work we have taken the matrices from Bilbao crystallographic data server [27] and consequently we used the conventions used therein. Unfortunately, this is not the only convention in the literature. The discussion on the effect of the choice of the convention for  $\Gamma'$  on the form of basis states  $|\psi_i\rangle$  and the form of  $\mathbf{k} \cdot \mathbf{p}$  Hamiltonian is given at the end of Secs. II B and II C of Ref. [30].

#### III. RESULTS

In this section, we apply the methodology described in Sec. II to bulk zinc-blende CdSe crystal and to zinc-blende CdSe quantum well. We apply the methodology to obtain the form and the parameters of the  $8\times 8$  ( $4\times 4$ ) and  $26\times 26$  ( $13\times 13$ ) symmetry adapted  $\mathbf{k}\cdot\mathbf{p}$  Hamiltonian with (without) spin-orbit interaction included for CdSe in the zinc-blende structure. We will refer to the  $8\times 8$  ( $4\times 4$ ) Hamiltonian as the standard Hamiltonian, while  $26\times 26$  ( $13\times 13$ ) Hamiltonian will be referred to as the extended Hamiltonian.

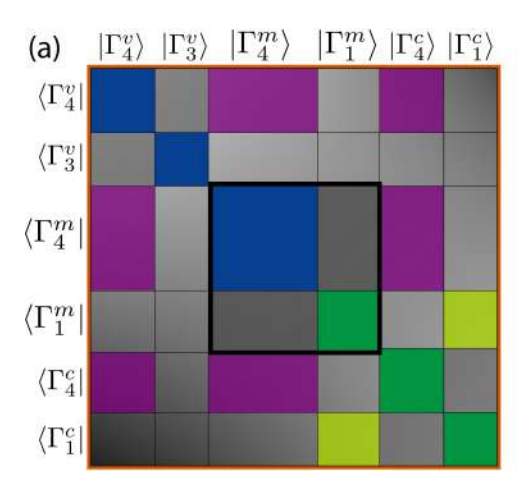
The band energies and wave functions were obtained from DFT where exchange-correlation energy was modeled using the Perdew-Burke-Ernzerhof generalized gradient approximation revised for solids (PBEsol) [31]. Calculations were performed using the Quantum Espresso code [32,33]. Core electrons were modeled using fully relativistic optimized normconserving Vanderbilt pseudopotentials [34,35]. The  $10 \times 10 \times 10$  grid in reciprocal space of the Brillouin zone was used, while the kinetic energy cutoff of the plane waves used to represent the wave functions was 90 Ry. The lattice constant of  $a = 6.096 \,\text{Å}$ , obtained by minimization of the energy of the structure, was used in all subsequent calculations.

Since local and semilocal approximations in DFT do not give accurate values of the band gap [1], we have also performed the band structure calculation using many-body perturbation theory in the GW approximation [4]. Within this approach, the electron self-energy is approximated using the expression containing the Green's function G and the screened Coulomb interaction W. In this work, we used the G<sub>0</sub>W<sub>0</sub> variant of GW approximation in which the selfenergy is obtained from Green's function G<sub>0</sub> of an electron in DFT Kohn-Sham potential, without further iterations. The calculations were performed using the YAMBO code [36,37], with input Kohn-Sham wave functions obtained from a previous DFT calculation on the  $4 \times 4 \times 4$  grid in reciprocal space. Plasmon-pole approximation was used to account for the frequency dependence of the dielectric function. Kinetic energy cutoff used for the calculation of dielectric function in G<sub>0</sub>W<sub>0</sub> calculation was 50 Ry. The corresponding number of bands was 400 (800), while the number of bands used in the evaluation of self-energy was 300 (600) in the case when spin-orbit interaction is omitted (included). We estimate that these values yield numerical accuracy of 20 meV or better for band energy corrections.

#### A. Bulk zinc-blende CdSe

We used the procedure described in Sec. II to obtain the standard and extended  $\mathbf{k} \cdot \mathbf{p}$  Hamiltonian in symmetry-adapted form.  $\Gamma$  point was chosen as the point  $\mathbf{k}_0$  in our procedure, since zinc-blende CdSe exhibits a direct gap at the  $\Gamma$  point. The corresponding group  $G_{\mathbf{k}_0}$  is then the point symmetry group of the crystal, which is the  $T_d$  group in the case of zinc-blende structures. We will denote irreps of this group using the convention of Ref. [38].

We will refer to the states that are included in the standard  $\mathbf{k} \cdot \mathbf{p}$  Hamiltonian as the main states, while remaining states included in the extended Hamiltonian will be referred to as



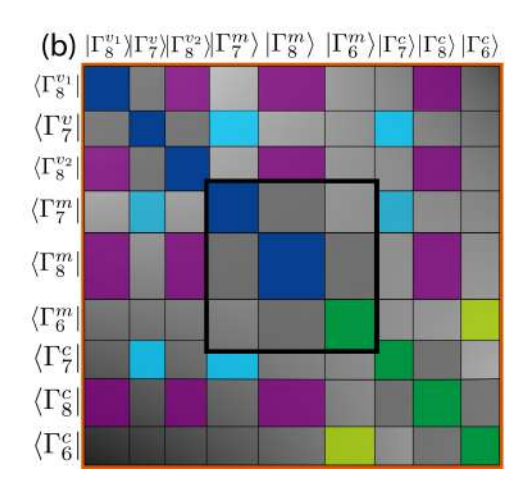


FIG. 1. The form of  $\mathbf{k} \cdot \mathbf{p}$  Hamiltonian obtained when spin-orbit interaction is (a) omitted; (b) included. Each block of the matrix contains the terms that originate from matrix elements between the states that transform according to irrep specified on the left and above the matrix. The superscripts v, m, and c denote the lower valence band states, the main states, and the higher conduction band states. The central square marked with thick black lines denotes the standard Hamiltonian.

lower valence band and higher conduction band states. When spin-orbit interaction is omitted, main states used to construct the standard Hamiltonian are the threefold degenerate  $\Gamma_4$  and nondegenerate  $\Gamma_1$  states that lie below and above the gap, respectively, giving a total of four states. Extended Hamiltonian is constructed by adding the twofold degenerate  $\Gamma_3$ and threefold degenerate  $\Gamma_4$  valence states and  $\Gamma_4$  and  $\Gamma_1$ conduction states, yielding a total of 13 states. When spinorbit interaction is included, the states transform according to irreps of the double  $T_d$  group. The states corresponding to  $\Gamma_4$  will split into fourfold  $\Gamma_8$  and twofold degenerate  $\Gamma_7$  state, the states corresponding to  $\Gamma_3$  become fourfold degenerate  $\Gamma_8$  and the states corresponding to  $\Gamma_1$  become twofold degenerate  $\Gamma_6$  states. The characters of the irreps of the single and the double point group  $T_d$  are given in Sec. I of Ref. [30].

In Fig. 1, we show the form of both extended and standard Hamiltonian, in cases when the effects of spin-orbit interaction are omitted and included. The Hamiltonian is divided into blocks, where each block originates from two groups of degenerate states with the corresponding irrep shown on the left and above the matrix. These blocks can be absolutely diagonal (connecting same irreps from same states), irrepdiagonal (connecting same irreps from different states) and off-diagonal. When our procedure is applied, each block is obtained in the form with smallest number of parameters in the block, determined by the point group of the crystal. Analytical expressions for the elements of all blocks of the  $\mathbf{k} \cdot \mathbf{p}$  Hamiltonian are given in Sec. II of Ref. [30]. We have checked that the same form of the blocks of the Hamiltonian is obtained when Luttinger's method of invariants [11,29] is applied. Numerical values of each parameter appearing in the blocks of the Hamiltonian are given in Sec. III of Ref. [30]. We note that the standard four-band Hamiltonian that we obtain coincides with the second-order four-band Kane Hamiltonian [11]. The standard eight-band Hamiltonian that we obtain coincides with Weiler eight-band Hamiltonian [11,12] after an appropriate unitary transformation is made. The details of this unitary transformation are given in Sec. II B of Ref. [30]. To better illustrate the advantage of using a symmetry-adapted form of the  $\mathbf{k} \cdot \mathbf{p}$  Hamiltonian (that is obtained from symmetrized wave functions  $|\psi_i\rangle$ ) rather than the form of the  $\mathbf{k} \cdot \mathbf{p}$  Hamiltonian that would be obtained directly from DFT wave functions  $|\phi_i\rangle$ , we compare the number of parameters in the two forms of the Hamiltonian. The two forms of the four-band Hamiltonian are presented in Sec. II C of Ref. [30]. The number of parameters of the symmetrized form is significantly smaller (1 versus 9 parameters for the terms linear in k and 5 versus 46 parameters for the terms quadratic in k), which clearly shows its advantage in terms of simplicity for further use in the study of nanostructures.

In Fig. 2 we plot the band structure of zinc-blende CdSe obtained from DFT calculation and by diagonalizing the standard and extended  $\mathbf{k} \cdot \mathbf{p}$  Hamiltonian in cases with and without the effects of spin-orbit interaction. As expected, extended Hamiltonian gives results that are qualitatively and quantitatively closer to full DFT than the standard one. It should be noted that it is preferable to add the states in extended Hamiltonian symmetrically around the main states. We found that expanding the standard Hamiltonian by a noneven number of valence and conduction states can lead to closing of the gap at points far away from  $\Gamma$  point. This was more prone to happen if the number of conduction states added was greater than number of valence states added. The presence of such spurious states then prevents the application of the  $\mathbf{k} \cdot \mathbf{p}$  Hamiltonian to the nanostructure. Our choice of 13 (26) bands used to construct the extended Hamiltonian was therefore a compromise between (i) the goal to accurately describe the band structure within the part of the Brillouin zone which is as large as possible; (ii) the desire to use the number of bands (and therefore the number of parameters of the  $\mathbf{k} \cdot \mathbf{p}$  Hamiltonian) that is not extremely large; (iii) the aim to avoid the appearance of spurious states that close the gap. To quantify in more detail the ability of derived  $\mathbf{k} \cdot \mathbf{p}$  Hamiltonians to reproduce the *ab initio* calculated band structure, we plot in Fig. 3 the maximal difference between  $\mathbf{k} \cdot \mathbf{p}$  and DFT results within the sphere of radius  $k_r$  (which is centered at the  $\Gamma$  point) for main bands. We find that standard

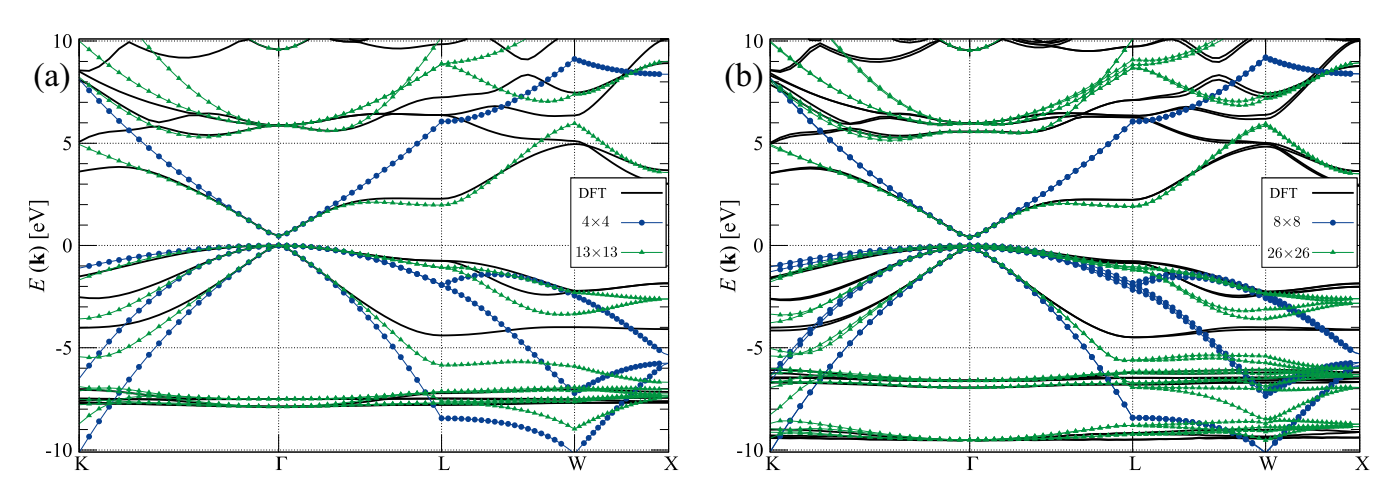


FIG. 2. Band structure of zinc-blende CdSe calculated using DFT and using standard and extended  $\mathbf{k} \cdot \mathbf{p}$  Hamiltonian when the effects of spin-orbit interaction are (a) omitted; (b) included.

(extended)  $\mathbf{k} \cdot \mathbf{p}$  results differ no more than 4 eV (1.75 eV) inside the sphere inscribed in the first Brillouin zone, with a difference not greater than 45 meV (35 meV) inside a sphere of radius  $k_r = 0.2$  in units of  $2\pi/a$ , where a is the lattice constant. Figure 3 shows that in the reasonable vicinity of  $\Gamma$ point, in any direction, extended  $\mathbf{k} \cdot \mathbf{p}$  Hamiltonians produce a band structure that is significantly closer to DFT results, than the standard  $\mathbf{k} \cdot \mathbf{p}$  Hamiltonians. The use of extended Hamiltonians is necessary in many practical cases. If one wishes to study only the low field electrical properties or the optical properties at photon energies just above the band gap, the standard Hamiltonians are usually sufficient. However, if one is interested in optical properties in a wider energy range (which is relevant, for example, for solar cells) or transport at larger electrical fields (which is relevant in field-effect transistors) extended Hamiltonians are required to properly describe all relevant electronic states.

For the results presented so far, the  $\mathbf{k}\cdot\mathbf{p}$  Hamiltonian was constructed starting from the wave functions and energies of Kohn-Sham orbitals obtained from DFT using the PBEsol

functional. It is well known that the DFT band gap is typically significantly smaller from experimental gap and for this reason the same applies to  $\mathbf{k} \cdot \mathbf{p}$  band structure obtained starting from DFT wave functions and energies. The methodology that we described is by no means limited to using the DFT wave functions and energies. To demonstrate this, we have calculated the self-energy corrections to energies  $E_n(\mathbf{k}_0)$  within the  $G_0W_0$  approximation. The  $G_0W_0$  calculation gives the band gap values of 1.77 and 1.60 eV without and with inclusion of spin-orbit interaction, respectively. These results are in good agreement with experimental value of 1.71 eV [39]. As expected, this is a great improvement over DFT, which underestimates the gap at 0.47 eV (without spin-orbit interaction) and 0.40 eV (with spin-orbit interaction).

The energies  $E_n(\mathbf{k}_0)$  obtained from  $G_0W_0$  calculation were then used in Eqs. (10) and (8) to construct the standard and extended  $\mathbf{k} \cdot \mathbf{p}$  Hamiltonian. The parameters of these Hamiltonians are given in Secs. III G and III H of Ref. [30], while the band structure obtained from diagonalization of these Hamiltonians is presented in Fig. 4.

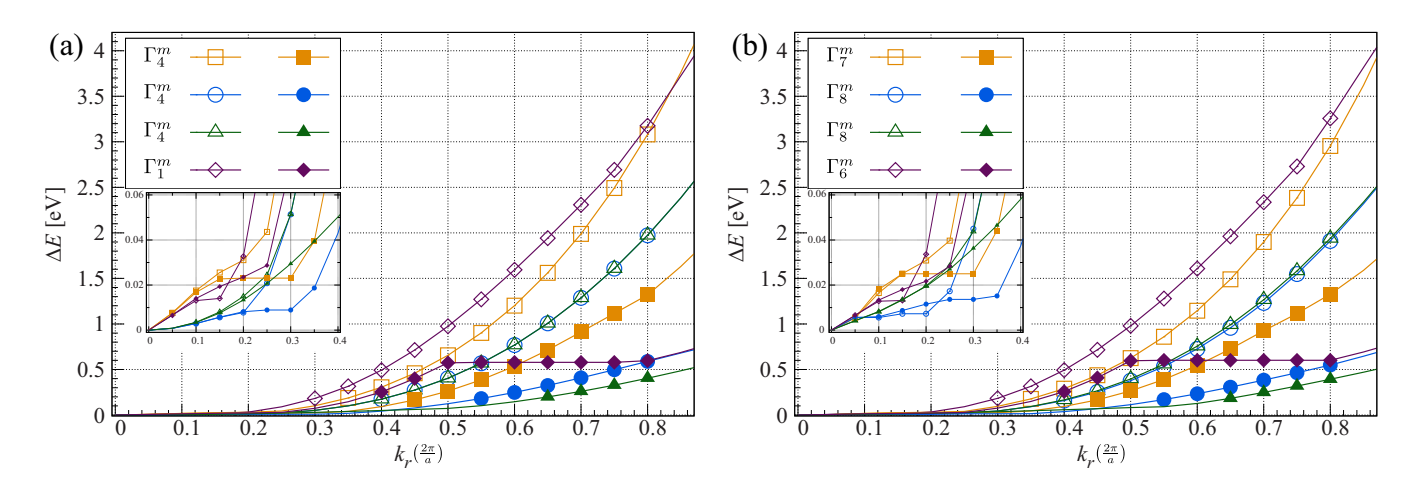


FIG. 3. Maximal absolute difference  $\Delta E$  between the band energy obtained from DFT and  $\mathbf{k} \cdot \mathbf{p}$  within the region of the Brillouin zone in the shape of a sphere of radius  $k_r$  centered at  $\Gamma$  when the effects of spin-orbit interaction are (a) omitted; (b) included. The difference is shown for main bands where the results obtained using standard  $\mathbf{k} \cdot \mathbf{p}$  Hamiltonian are shown using empty symbols, while the results obtained using the extended  $\mathbf{k} \cdot \mathbf{p}$  Hamiltonian are shown using filled symbols. Insets show a zoom of the same graph in the region around  $k_r = 0$ .

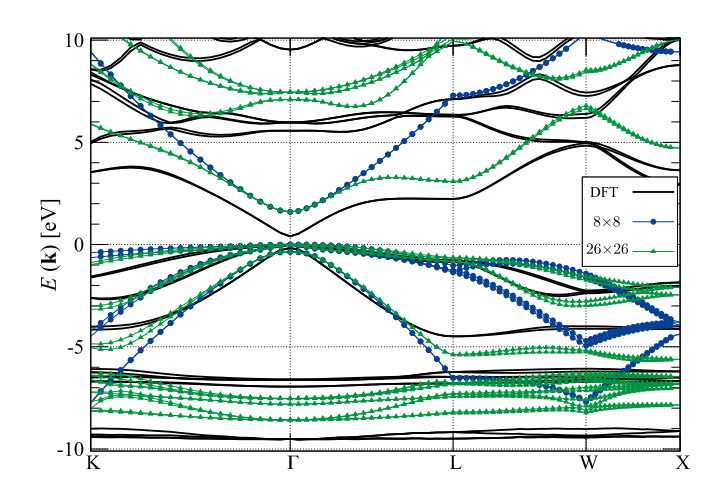


FIG. 4. Band structure of zinc-blende CdSe calculated using standard and extended  $\mathbf{k} \cdot \mathbf{p}$  Hamiltonian parametrized starting from band energies obtained in  $G_0W_0$  calculation. DFT results are given for comparison.

#### B. CdSe quantum well

We finally demonstrate the usefulness of the procedure developed and the Hamiltonians derived by applying them to calculate the electronic states in zinc-blende CdSe quantum wells of various well widths. We perform the calculation both using the  $\mathbf{k} \cdot \mathbf{p}$  method and using DFT and we compare the results that we obtain using the two approaches.

Within DFT, we perform the calculation of electronic states of a quantum well by considering the slab of CdSe material whose surfaces are perpendicular to the [001] direction. We terminate the slab with Cd layer at both surfaces and add pseudohydrogen atoms of charge 1.5 to passivate the dangling bonds at surfaces. Pseudohydrogen atoms are positioned at a distance of 1.58 Å from the corresponding Cd atom. For slabs of the width  $\leq 6a$  (>6a), the vacuum region of the width equal to 3a (half of the slab width) was added on both sides of the quantum well, to avoid the interaction of the quantum well with its images caused by periodic boundary conditions in the calculation. The calculation was performed for quantum wells containing from 1 to 18 CdSe unit cells. We define the quantum well width as the distance between the two pseudohydrogen passivating layers. We performed the calculation without the effect of spin-orbit interaction included to lower the computational cost and therefore extend the range of well widths for comparison of DFT and  $\mathbf{k} \cdot \mathbf{p}$ results.

In the case of a quantum well whose plane is perpendicular to the z direction, electronic states within the  $\mathbf{k} \cdot \mathbf{p}$  model can be obtained by solving the eigenvalue problem

$$\sum_{n} H_{mn} \left( k_x, k_y, -i \frac{d}{dz} \right) \Psi_n^{(a)}(z) = E^{(a)} \Psi_m^{(a)}(z), \tag{16}$$

where  $H_{mn}(k_x, k_y, -i\frac{d}{dz})$  is the  $\mathbf{k} \cdot \mathbf{p}$  Hamiltonian of the bulk with  $k_z$  component of the wave vector replaced by the differential operator  $-i\frac{d}{dz}$ ,  $\Psi_n^{(a)}(z)$  is the envelope function corresponding to the state (a) of band n, while  $E^{(a)}$  is the energy of that state. We solve the eigenvalue problem using the plane wave expansion method [40–45]. The well is embedded in the

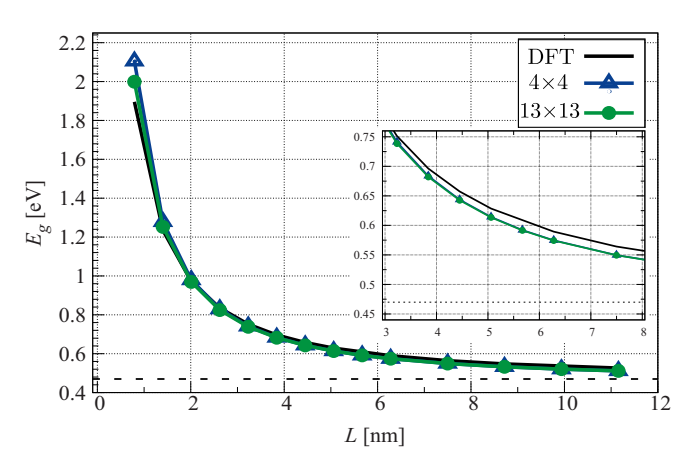


FIG. 5. Dependence of zinc-blende CdSe quantum well band gap on well width. The results obtained from DFT without the effects of spin-orbit coupling and from standard  $4 \times 4$  and extended  $13 \times 13$  **k** · **p** models are presented. The inset shows the zoom of the same dependence to the narrower range in the figure. The horizontal dashed line denotes the bulk DFT band gap.

region of length  $L_z$  and the envelope functions are expanded into a linear combination of plane waves

$$\Psi_n^{(a)}(z) = \frac{1}{\sqrt{L_z}} \sum_{n=-N_z}^{N_z} c_{n,n_z}^{(a)} e^{i\frac{2\pi}{L_z} n_z z},$$
 (17)

where  $c_{n,n_z}^{(a)}$  are expansion coefficients that have to be determined and  $N_z$  is an integer that defines the total number of plane waves. After substitution of Eq. (17) into Eq. (16) we obtain the eigenvalue problem of the Hermitian matrix that we diagonalize using standard numerical routines to obtain the coefficients  $c_{n,nz}^{(a)}$  and the energies  $E^{(a)}$ . For a fair comparison with DFT calculation of CdSe slab in vacuum, we perform the calculation for a quantum well inside a large energy barrier. We therefore model the region outside the quantum well as an artificial material whose all parameters are the same as CdSe parameters except the band energies at the  $\Gamma$  point. In this artificial material, we increase all energies of conduction bands by  $\Delta E$  with respect to corresponding energies in CdSe and decrease all energies of valence bands by the same amount  $\Delta E$ . In the calculation we use the values  $\Delta E = 5$  eV,  $L_z = 20 \text{ nm}$  and  $N_z = 50$ . We have checked that these are sufficiently large values whose further increase would not affect the results.

In Fig. 5 we present the dependence of the band gap on well width obtained within DFT and within the  $\mathbf{k} \cdot \mathbf{p}$  model. For a fair comparison, the results of DFT calculation without the effects of spin-orbit interaction were compared with  $\mathbf{k} \cdot \mathbf{p}$  models without spin-orbit interaction; the  $4 \times 4$  and the  $13 \times 13$  model. The agreement between DFT and  $\mathbf{k} \cdot \mathbf{p}$  results and between the results of the two  $\mathbf{k} \cdot \mathbf{p}$  models is excellent. For quantum well widths of three lattice constants and larger the band gap differences are smaller than 20 meV. The agreement is quite satisfactory even for rather thin wells of 1 and 2 unit cells, where one might not have expected that  $\mathbf{k} \cdot \mathbf{p}$  performs so well. It is also important to note that the calculation of electronic structure of the quantum well using the  $\mathbf{k} \cdot \mathbf{p}$  approach takes only up to a few seconds on a single-core desktop

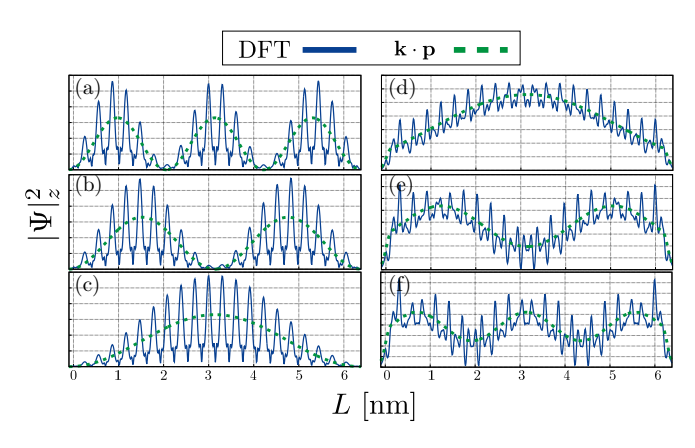


FIG. 6. The wave-function moduli squared of quantum well states obtained from DFT without the effects of spin-orbit coupling and the four-band  $\mathbf{k} \cdot \mathbf{p}$  model. The DFT wave functions are presented by performing the in-plane average of wave-function moduli squared. The  $\mathbf{k} \cdot \mathbf{p}$  wave functions are presented by a sum  $\sum_n |\Psi_n(z)|^2$ . The wave functions that are presented in the figure correspond to the following states: (a) VBM-4, (b) degenerate VBM-3 and VBM-2, (c) degenerate VBM-1 and VBM, (d) CBM, (e) CBM + 1, (f) CBM + 2, where VBM (valence band maximum) denotes the highest energy state in the valence band, while CBM (conduction band minimum) denotes the lowest energy state in the conduction band.

computer, regardless of the width of the quantum well. DFT calculations, however, take minutes or hours depending on the width of the quantum well on a computing cluster with several nodes. For example, our calculation times range from approximately 3 min (using 32 cores) to 21 h (using 64 cores) for narrowest and widest quantum wells calculated by DFT, respectively. In the case of nanostructures confined in all three spatial directions, such as quantum dots, the advantages of  $\mathbf{k} \cdot \mathbf{p}$  over DFT become even more pronounced. Due to a lack of periodicity in any direction, one needs to calculate supercells with quite a large number of atoms in DFT and the problem becomes computationally intractable for DFT. On the other hand,  $\mathbf{k} \cdot \mathbf{p}$  is almost routinely used to study quantum dots, see for example, Refs. [40–45].

We next discuss the origin of somewhat surprisingly good agreement between DFT and  $\mathbf{k} \cdot \mathbf{p}$  for thin wells. Within  $\mathbf{k} \cdot \mathbf{p}$ the atomistic wave function (shown in Fig. 6 in full lines) is represented in terms of the product of slowly varying envelope functions (shown in Fig. 6 in dashed lines) and rapidly varying bulk Bloch functions, while the only additional approximation in  $\mathbf{k} \cdot \mathbf{p}$  with respect to the atomistic method (DFT in our case) comes from truncation of the wave-function expansion to a limited set of bands. For this reason, we believe that excellent agreement between  $\mathbf{k} \cdot \mathbf{p}$  and DFT results for wide wells is expected because basis functions used in  $\mathbf{k} \cdot \mathbf{p}$  provide a good basis set in this case. In the case of very thin wells, one could argue that the representation of the wave function in terms of the product of envelope functions and bulk Bloch functions for a few bands only cannot be a good representation because the system is rather different from bulk and therefore the basis formed from bulk Bloch functions cannot be a good basis. Our results for CdSe wells confirm that such an argument is certainly valid to some extent because the agreement between

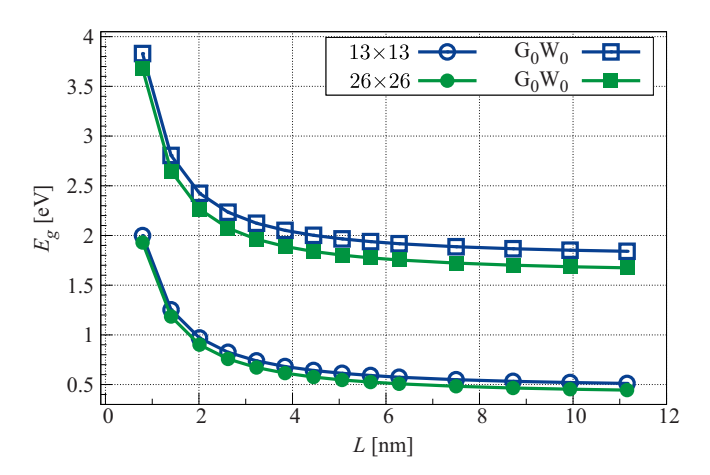


FIG. 7. Well width dependence of zinc-blende CdSe quantum well band gap calculated using the  $\mathbf{k} \cdot \mathbf{p}$  method. The parameters of the  $\mathbf{k} \cdot \mathbf{p}$  Hamiltonian were extracted from  $G_0W_0$  calculation of bulk band structure. The results obtained with and without the effects of spin-orbit interaction are shown, respectively, in full and empty squares. The results obtained from  $\mathbf{k} \cdot \mathbf{p}$  Hamiltonians parametrized from DFT are shown for comparison in full (the case with spin-orbit interaction) and empty (the case without spin-orbit interaction) circles.

DFT and  $\mathbf{k} \cdot \mathbf{p}$  becomes somewhat worse for quite thin wells. Nevertheless, we find that the agreement between DFT and  $\mathbf{k} \cdot \mathbf{p}$  is quite satisfactory even then and we note that it would be quite interesting to investigate in the future if this is also the case for other materials. It should be noted as well that the use of pseudohydrogen surface passivation also contributes in making the wave functions of thin wells closer to wave functions of bulk material.

We finally present the results of the calculation of CdSe quantum well electronic states, using the  $\mathbf{k} \cdot \mathbf{p}$  Hamiltonians parametrized from  $G_0W_0$  calculation of bulk band structure (the parameters of these Hamiltonians are given in Secs. III F and III H of Ref. [30]). To obtain an accurate quasiparticle band gap, we add to the band gap obtained from  $\mathbf{k} \cdot \mathbf{p}$  Hamiltonian the correction which takes into account the dielectric mismatch between the quantum well and the vacuum, i.e., the image charge effect. The correction was added using the analytical formula presented in Ref. [46], which was also recently applied in a DFT study of CdSe nanoplatelets [47]. The results obtained are presented in Fig. 7 along with the results obtained from  $\mathbf{k} \cdot \mathbf{p}$  Hamiltonians parametrized from DFT, which are given for comparison. As expected, we obtain significantly larger band gaps using  $\mathbf{k} \cdot \mathbf{p}$  Hamiltonians parametrized from G<sub>0</sub>W<sub>0</sub> calculation of bulk. We note that we focused in this work on single particle energies and the reported gaps are the quasiparticle band gaps. To obtain the optical gap, one would additionally need to consider excitonic effects, which was also recently done for CdSe nanoplatelets in Ref. [47].

#### IV. CONCLUSION

In conclusion, we presented the method that allows automatic construction of  $\mathbf{k} \cdot \mathbf{p}$  Hamiltonians in their symmetry-adapted form starting from output of *ab initio* band structure calculation of bulk material. We then presented

the application of the method to construct the  $\mathbf{k} \cdot \mathbf{p}$  Hamiltonians for zinc-blende CdSe material. These Hamiltonians were subsequently used to calculate the electronic states in CdSe quantum wells. Interestingly, excellent agreement was obtained between the results obtained from  $\mathbf{k} \cdot \mathbf{p}$  and DFT calculations of quantum wells, even for rather thin wells. While construction and parametrization of  $\mathbf{k} \cdot \mathbf{p}$  Hamiltonians is usually believed to be a rather difficult and time consuming task, we expect that the method that we presented will change this situation and that it will be straightforward in the future to obtain  $\mathbf{k} \cdot \mathbf{p}$  Hamiltonians for new materials and apply them to study electronic properties of nanostructures based

on these materials without the need to perform any kind of fitting.

#### ACKNOWLEDGMENTS

The authors acknowledge funding provided by the Institute of Physics Belgrade, through the grant by Ministry of Education, Science and Technological Development of the Republic of Serbia. Numerical simulations were run on the PARADOX-IV supercomputing facility at the Scientific Computing Laboratory, National Center of Excellence for the Study of Complex Systems, Institute of Physics Belgrade.

- [1] J. P. Perdew, Density functional theory and the band gap problem, Int. J. Quantum Chem. **28**, 497 (1985).
- [2] J. P. Perdew, M. Ernzerhof, and K. Burke, Rationale for mixing exact exchange with density functional approximations, J. Chem. Phys. 105, 9982 (1996).
- [3] C. Adamo and V. Barone, Toward reliable density functional methods without adjustable parameters: The PBE0 model, J. Chem. Phys. 110, 6158 (1999).
- [4] L. Hedin, New method for calculating the one-particle Green's function with application to the electron-gas problem, Phys. Rev. 139, A796 (1965).
- [5] M. Shishkin and G. Kresse, Self-consistent GW calculations for semiconductors and insulators, Phys. Rev. B 75, 235102 (2007).
- [6] W. Chen and A. Pasquarello, Band-edge levels in semiconductors and insulators: Hybrid density functional theory versus many-body perturbation theory, Phys. Rev. B 86, 035134 (2012).
- [7] Y. Hinuma, Y. Kumagai, I. Tanaka, and F. Oba, Band alignment of semiconductors and insulators using dielectric-dependent hybrid functionals: Toward high-throughput evaluation, Phys. Rev. B 95, 075302 (2017).
- [8] J. M. Luttinger and W. Kohn, Motion of electrons and holes in perturbed periodic fields, Phys. Rev. 97, 869 (1955).
- [9] E. Kane, Energy band structure in p-type germanium and silicon, J. Phys. Chem. Solids 1, 82 (1956).
- [10] C. R. Pidgeon and R. N. Brown, Interband magneto-absorption and Faraday rotation in InSb, Phys. Rev. 146, 575 (1966).
- [11] L. C. Lew Yan Voon and M. Willatzen, *The* **k** · **p** *Method: Electronic Properties of Semiconductors* (Springer-Verlag, Berlin, 2009).
- [12] M. H. Weiler, R. L. Aggarwal, and B. Lax, Warping- and inversion-asymmetry-induced cyclotron-harmonic transitions in InSb. Phys. Rev. B 17, 3269 (1978).
- [13] T. B. Bahder, Eight-band k ⋅ p model of strained zinc-blende crystals, Phys. Rev. B **41**, 11992 (1990).
- [14] I. Vurgaftman, J. R. Meyer, and L. R. Ram-Mohan, Band parameters for III-V compound semiconductors and their alloys, J. Appl. Phys. 89, 5815 (2001).
- [15] I. Vurgaftman and J. R. Meyer, Band parameters for nitrogen-containing semiconductors, J. Appl. Phys. **94**, 3675 (2003).
- [16] M. El Kurdi, G. Fishman, S. Sauvage, and P. Boucaud, Band structure and optical gain of tensile-strained germanium based on a 30 band k · p formalism, J. Appl. Phys. **107**, 013710 (2010).

- [17] S. Richard, F. Aniel, and G. Fishman, Energy-band structure of Ge, Si, and GaAs: A thirty-band **k** · **p** method, Phys. Rev. B **70**, 235204 (2004).
- [18] S. Boyer-Richard, F. Raouafi, A. Bondi, L. Pédesseau, C. Katan, J.-M. Jancu, and J. Even, 30-band k ⋅ p method for quantum semiconductor heterostructures, Appl. Phys. Lett. 98, 251913 (2011).
- [19] Z. Song, W. Fan, C. S. Tan, Q. Wang, D. Nam, D. H. Zhang, and G. Sun, Band structure of  $Ge_{1-x}Sn_x$  alloy: A full-zone 30-band  $k \cdot p$  model, New J. Phys. **21**, 073037 (2019).
- [20] N. A. Čukarić, M. Ž. Tadić, B. Partoens, and F. M. Peeters, 30-band **k** · **p** model of electron and hole states in silicon quantum wells, Phys. Rev. B **88**, 205306 (2013).
- [21] C. E. Pryor and M.-E. Pistol, Atomistic k ⋅ p theory, J. Appl. Phys. **118**, 225702 (2015).
- [22] C. Persson and C. Ambrosch-Draxl, A full-band FPLAPW + k·p-method for solving the Kohn-Sham equation, Comput. Phys. Commun. 177, 280 (2007).
- [23] K. Berland and C. Persson, Enabling accurate first-principle calculations of electronic properties with a corrected k · p scheme, Comput. Mater. Sci. **134**, 17 (2017).
- [24] T. Shishidou and T. Oguchi,  $\mathbf{k} \cdot \mathbf{p}$  formula for use with linearized augmented plane waves, Phys. Rev. B **78**, 245107 (2008).
- [25] C. J. Pickard and M. C. Payne, Extrapolative approaches to Brillouin-zone integration, Phys. Rev. B **59**, 4685 (1999).
- [26] P. Löwdin, A note on the quantum-mechanical perturbation theory, J. Chem. Phys. 19, 1396 (1951).
- [27] M. I. Aroyo, A. Kirov, C. Capillas, J. M. Perez-Mato, and H. Wondratschek, Bilbao Crystallographic Server. II. Representations of crystallographic point groups and space groups, Acta Crystallogr. Sect. A 62, 115 (2006).
- [28] M. Mozrzymas, M. Studziński, and M. Horodecki, Explicit constructions of unitary transformations between equivalent irreducible representations, J. Phys. A. 47, 505203 (2014).
- [29] J. M. Luttinger, Quantum theory of cyclotron resonance in semiconductors: General theory, Phys. Rev. 102, 1030 (1956).
- [30] See Supplemental Material at http://link.aps.org/supplemental/ 10.1103/PhysRevB.102.085121 for characters of irreducible representations of the  $T_d$  group, analytical expressions for the elements of all blocks of the  $\mathbf{k} \cdot \mathbf{p}$  Hamiltonians and numerical values of the parameters of the Hamiltonians.

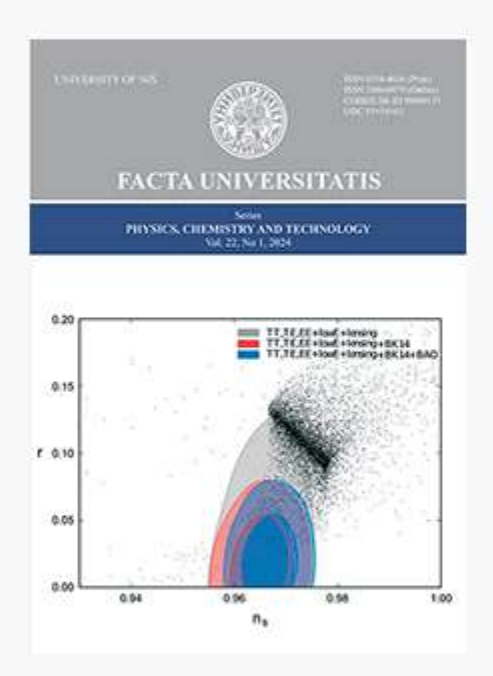
- [31] J. P. Perdew, A. Ruzsinszky, G. I. Csonka, O. A. Vydrov, G. E. Scuseria, L. A. Constantin, X. Zhou, and K. Burke, Restoring the Density-Gradient Expansion for Exchange in Solids and Surfaces, Phys. Rev. Lett. 100, 136406 (2008).
- [32] P. Giannozzi, S. Baroni, N. Bonini, M. Calandra, R. Car, C. Cavazzoni, D. Ceresoli, G. L. Chiarotti, M. Cococcioni, I. Dabo, A. Dal Corso, S. de Gironcoli, S. Fabris, G. Fratesi, R. Gebauer, U. Gerstmann, C. Gougoussis, A. Kokalj, M. Lazzeri, L. Martin-Samos, N. Marzari, F. Mauri, R. Mazzarello, S. Paolini, A. Pasquarello, L. Paulatto, C. Sbraccia, S. Scandolo, G. Sclauzero, A. P. Seitsonen, A. Smogunov, P. Umari, and R. M. Wentzcovitch, QUANTUM ESPRESSO: A modular and open-source software project for quantum simulations of materials, J. Phys.: Condens. Matter 21, 395502 (2009).
- [33] P. Giannozzi, O. Andreussi, T. Brumme, O. Bunau, M. B. Nardelli, M. Calandra, R. Car, C. Cavazzoni, D. Ceresoli, M. Cococcioni, N. Colonna, I. Carnimeo, A. D. Corso, S. de Gironcoli, P. Delugas, R. A. D. Jr, A. Ferretti, A. Floris, G. Fratesi, G. Fugallo, R. Gebauer, U. Gerstmann, F. Giustino, T. Gorni, J. Jia, M. Kawamura, H.-Y. Ko, A. Kokalj, E. Kucukbenli, M. Lazzeri, M. Marsili, N. Marzari, F. Mauri, N. L. Nguyen, H.-V. Nguyen, A. O. de-la Roza, L. Paulatto, S. Poncé, D. Rocca, R. Sabatini, B. Santra, M. Schlipf, A. P. Seitsonen, A. Smogunov, I. Timrov, T. Thonhauser, P. Umari, N. Vast, X. Wu, and S. Baroni, Advanced capabilities for materials modeling with Quantum ESPRESSO, J. Phys.: Condens. Matter 29, 465901 (2017).
- [34] D. R. Hamann, Optimized norm-conserving Vanderbilt pseudopotentials, Phys. Rev. B **88**, 085117 (2013).
- [35] M. van Setten, M. Giantomassi, E. Bousquet, M. Verstraete, D. Hamann, X. Gonze, and G.-M. Rignanese, The pseudodojo: Training and grading a 85 element optimized norm-conserving pseudopotential table, Comp. Phys. Comm. 226, 39 (2018).
- [36] D. Sangalli, A. Ferretti, H. Miranda, C. Attaccalite, I. Marri, E. Cannuccia, P. Melo, M. Marsili, F. Paleari, A. Marrazzo, G. Prandini, P. Bonfà, M. O. Atambo, F. Affinito, M. Palummo, A. Molina-Sánchez, C. Hogan, M. Grüning, D. Varsano, and A.

- Marini, Many-body perturbation theory calculations using the Yambo code, J. Phys.: Condens. Matter **31**, 325902 (2019).
- [37] A. Marini, C. Hogan, M. Grüning, and D. Varsano, Yambo: An *ab initio* tool for excited state calculations, Comp. Phys. Comm. **180**, 1392 (2009).
- [38] A. P. Cracknell, B. L. Davies, S. C. Miller, and W. F. Love, Kronecker Product Tables, 1, General Introduction and Tables of Irreducible Representations of Space groups (IFI/Plenum, New York, 1979).
- [39] S. Ninomiya and S. Adachi, Optical properties of cubic and hexagonal CdSe, J. Appl. Phys. 78, 4681 (1995).
- [40] M. A. Cusack, P. R. Briddon, and M. Jaros, Electronic structure of InAs/GaAs self-assembled quantum dots, Phys. Rev. B 54, R2300 (1996).
- [41] S.-S. Li, J.-B. Xia, Z. L. Yuan, Z. Y. Xu, W. Ge, X. R. Wang, Y. Wang, J. Wang, and L. L. Chang, Effective-mass theory for InAs/GaAs strained coupled quantum dots, Phys. Rev. B 54, 11575 (1996).
- [42] A. D. Andreev and E. P. O'Reilly, Theory of the electronic structure of GaN/AlN hexagonal quantum dots, Phys. Rev. B 62, 15851 (2000).
- [43] S. Tomić, A. G. Sunderland, and I. J. Bush, Parallel multi-band k · p code for electronic structure of zinc blend semiconductor quantum dots, J. Mater. Chem. 16, 1963 (2006).
- [44] N. Vukmirović, D. Indjin, V. D. Jovanović, Z. Ikonić, and P. Harrison, Symmetry of  $\mathbf{k} \cdot \mathbf{p}$  Hamiltonian in pyramidal InAs/GaAs quantum dots: Application to the calculation of electronic structure, Phys. Rev. B **72**, 075356 (2005).
- [45] N. Vukmirović and S. Tomić, Plane wave methodology for single quantum dot electronic structure calculations, J. Appl. Phys. 103, 103718 (2008).
- [46] Y. Cho and T. C. Berkelbach, Environmentally sensitive theory of electronic and optical transitions in atomically thin semiconductors, Phys. Rev. B **97**, 041409(R) (2018).
- [47] Q. Zhou, Y. Cho, S. Yang, E. A. Weiss, T. C. Berkelbach, and P. Darancet, Large band edge tunability in colloidal nanoplatelets, Nano Lett. 19, 7124 (2019).

### Facta Universitatis, Series: Physics, Chemistry and Technology

Facta Universitatis. Series: Physics, Chemistry and Technology (FU Phys Chem Tech) is an international, peer-reviewed, Open Access journal devoted to basic and applied research in physics, chemistry and technology with the experience of almost twenty years of publishing of high quality research. The journal features topics in all areas of physics, chemistry and technology and related disciplines. The content is freely accessible online and authors can publish scientific articles free of charge as the journal is completely funded by the University of Niš and the Ministry of Education, Science and Technological Development of the Republic of Serbia. Editor-in-Chief: Niko Radulović

In order to create/register an account for submitting a paper, first time authors are to contact the Computer Support at mile@ni.ac.rs stating your first name, last name, affiliation with the link, and your email. We will then send you back an email with your login parameters. Once you receive your parameters from us you will then be able to log in and begin article submission.



Editor-in-Chief: Niko Radulović e-mail: nikoradulovic@yahoo.com

Section editor: Polina Blagojević e-mail: blagojevicpolina@pmf.ni.ac.rs

Editorial Board

View issues from 1994 to 2013

Instructions for authors

Announcements

Editor-in-Chief: Niko Radulović e-mail: nikoradulovic@yahoo.com

Section editor: Polina Blagojević e-mail: blagojevicpolina@pmf.ni.ac.rs

Editorial Board

View issues from 1994 to 2013

Instructions for authors

#### Announcements

#### Call for papers

FU PCT welcomes contributions from any field of physics, chemistry or technology

Posted: 2013-05-23

More Announcements...

001-011

Vol. 22, No 1, 2024

#### Table of Contents

#### Physics

METHOD

Milan Jocić, Nenad Vukmirović		
TACHYON INFLATION WITH A GENERALIZED T-MODE POTENTIAL IN THE FRAMEWORK OF THE HOLOGRAPHICS BRANEWORLD COSMOLOGY	PDF	013-023
Marko Stojanović, Neven Bilić, Dragoljub D. Dimitrijević, Goran S. Đorđević, Milan Milošević DIFFERENTIAL CROSS SECTIONS FOR ELECTRON CAPTURE FROM ATOMIC HYDROGEN BY FAST ALPHA PARTICLES	PDF	
Danilo Delibašić, Nenad Milojević, Ivan Mančev		025-036
Chemistry		
FERROCENE-CONTAINING CHOLINESTERASE INHIBITORS	PDF	11.14-04.750.750.740
Marija S. Genčić, Jelena D. Živanović, Jelena M. Denić, Danijela N. Nikolić, Niko S. Radulović		037-051
COMPARATIVE CHEMICAL ANALYSIS OF ORIGANUM MAJORANA ESSENTIAL OILS FROM SERBIA AND EGYPT	PDF	111000000000000000000000000000000000000
Miljana R. Đorđević Zlatković, Dragan B. Zlatković, Niko S. Radulović		053-059
ESSENTIAL-OIL COMPOSITION OF PLANT SPECIES OF THE GENUS PELARGONIUM	PDF	VAN-SACROSS
Šejla F. Gusinac Avdović, Marko Z. Mladenović, Niko S. Radulović		061-077

TEMPERATURE DEPENDENCE OF THE ELECTRONIC BAND GAP OF CsPbBr3 QUANTUM WELLS OBTAINED USING K+P

ISSN 0354-4656 (print)

ISSN 2406-0879 (online)

#### FACTA UNIVERSITATIS

Series: Physics, Chemistry and Technology Vol. 22, No 1, 2024, pp. 1 - 11

https://doi.org/10.2298/FUPCT2401001J

Original scientific paper

# TEMPERATURE DEPENDENCE OF THE ELECTRONIC BAND GAP OF CsPbBr3 QUANTUM WELLS OBTAINED USING K•P METHOD

#### Milan Jocić<sup>1</sup>, Nenad Vukmirović<sup>2</sup>

<sup>1</sup>Department of Physics, Faculty of Sciences and Mathematics, University of Niš, Niš, Serbia <sup>2</sup>Institute of Physics Belgrade, University of Belgrade, Belgrade, Serbia

**Abstract**. We calculated the electronic structure of CsPbBr<sub>3</sub> quantum wells using the **k•p** model with parameters extracted from hybrid functional based DFT calculations supplemented with self-energy corrections arising from the electron-phonon interaction. We obtained the temperature dependence of the band gap for different sizes of the quantum well. The results show that the temperature dependence in quantum wells is similar to the one found in bulk phase for all sizes of the well that were considered.

**Key words**: nanostructure, temperature dependence, quantum well,  $k \cdot p$  method.

#### 1. Introduction

Since most electronic and optical devices consist of semiconductor materials, there is a great significance in knowing the properties of these materials. Over the years, general improvements of these devices made them smaller in size and more power efficient. Reducing the size from a bulk phase, that can be as small as few micrometers, down to a nanostructure that has a scale of a few dozen nanometers or less introduces a change in electronic properties of the material. This makes it possible to tune the electronic properties, like the band gap of a material, to desired values, allowing us to replicate the electronic properties of a much more expensive or less durable material with a material that is cheaper to produce or more durable. Working with nanostructures whose electronic properties change with their size introduces new challenges for investigating and modeling semiconductor materials.

For the past few decades, density functional theory (DFT) has been routinely used for modeling the properties of the bulk phase of semiconductors with much success, while their nanostructures would prove to be challenging since the required computational

Received: January 15th, 2024; accepted: December 10th, 2024

Corresponding author: Milan Jocić

Department of Physics, Faculty of Sciences and Mathematics, Višegradska 33, 18000 Niš, Serbia

E-mail: milan.jocic@pmf.ni.ac.rs

© 2024 by University of Niš, Serbia | Creative Commons License: CC BY-NC-ND

resources are increasing with the size of the nanostructure, and in some cases they become infeasible. Relying on the **k•p** method, alongside DFT, the computational resources required to obtain the electronic structure can be significantly reduced. One disadvantage of the **k•p** is that it considers only several selected bands of interest, while the rest of them are treated perturbatively (like in Löwdin, 1951.). The energy of these bands and their wave-functions have to be extracted from DFT calculation. Another disadvantage is that it can be a good approximation only in a relatively small vicinity around the point in the Brillouin zone from which DFT results are extracted. Since our main interest is the band gap of a nanostructure device, these disadvantages come at an acceptable cost. On the other hand, DFT provides information about all bands in the whole Brillouin zone which is more than sufficient in this case.

Once we determine the size dependent electronic properties of the nanostructure for the desired device, we have to take into account various external conditions that such device would operate under like the surrounding temperature. Both **k•p** and DFT, however, by themselves do not take into account any temperature effects that such devices might be exposed to, and since in practice they are expected to perform at a wide range of outside temperature conditions, these effects should be taken into account as well.

Regarding ab initio modeling of nanostructures, in our previous work (Jocić and Vukmirović 2020.) we provided, among other, a detailed explanation and comparison of DFT and k•p methods for bulk and quantum well (QW) nanostructures of CdSe. We have shown that the k•p method is in excellent agreement with DFT, even for rather thin QWs, using standard 8×8 (H8) and extended 26×26 (H26) k•p Hamiltonians which take into account the effects of spin-orbit coupling (SOC), which is necessary in the case of heavy ions such as lead.

To determine the effects of temperature on the electronic structure, in our recent paper (Jocic and Vukmirovic 2023.) we proposed a method that combines hybrid PBE0 functional based calculation in DFT with the Allen-Heine-Cardona (AHC) theory that provides temperature dependent self-energy correction of electronic bands. Because this self-energy has its origin in electron-phonon interactions it was necessary to obtain proper phonon frequencies, which are also temperature dependent and were obtained using the self-consistent phonon (SCPH) method. Self-energies are then obtained within the AHC theory using the on-the-mass-shell (OTMS) approximation. We also introduced a self-consistent procedure (SCP), which improves upon OTMS approximation, which evaluates these self-energies using interacting Green's functions and extracts the results from the corresponding spectral function. We performed this for several bands below and above the band gap at key points in the first Brillouin zone (1BZ). These methods allowed us to obtain good agreement of the band gap with the available experimental data for CsPbCl<sub>3</sub>, CsPbBr<sub>3</sub> and CsPbI<sub>3</sub> at zero temperature and the temperature at which transition to cubic phase takes place.

In this work, we turn our attention to perovskite crystal CsPbBr<sub>3</sub>, and calculate the temperature dependent gap of quantum wells (QW) made from this material. It was observed that CsPbBr<sub>3</sub> has two phase transitions as temperature increases. At low temperatures it forms an orthorhombic crystal structure that transforms to a tetragonal structure for a narrow range of temperatures, and then transforms to a cubic structure at a temperature of T = 403 K. Since CsPbBr<sub>3</sub> has recently found application in solar cells, the most interesting region would be the one of high temperatures of the cubic structure at which these solar cells would operate.

In this paper, we combine the method from our previous (Jocić and Vukmirović 2020.) and results from our recent (Jocić and Vukmirović 2023.) work in order to obtain the temperature dependence of band gaps for CsPbBr<sub>3</sub> OW nanostructures. The structure of the paper is as follows: In Theory section, we first provide a brief theoretical overview of the k\*p method for QW nanostructures using a plane wave (PW) basis and discuss the ordering of the bands that go into H8 and H26 Hamiltonians for the cubic structure of CsPbBr<sub>3</sub>. In the Results section, we first demonstrate the procedure for obtaining the convergence of the results with respect to necessary numerical parameters used in k•p method for OWs. We then present band structure with a more accurate band gap that is obtained from k•p, using hybrid DFT and temperature corrections for bulk, and a band structure for QW of fixed size using the same parameters. Finally, we show the temperature dependence of the electronic bands and band gaps for OW sizes ranging from around 2 nm to around 18 nm for temperature range from 400 to 700 K.

#### 2. Theory

Constructing a k·p Hamiltonian for nanostructures requires rewriting equations for bulk in a new form that is suitable for that case. Since the periodicity of the crystal is violated, in the general case, the electron momentum k is not a good quantum number anymore and we have to introduce envelope functions  $\psi_m$  alongside Bloch unit cell functions  $u_m$  in the expression for the wave-function  $\Psi$ :

$$\Psi = \sum_{m} \psi_{m} u_{m}. \tag{1}$$

In the case of a cubic CsPbBr<sub>3</sub> lattice, the OW is periodic in the (x, y) plane, and its size can be determined by counting the number of bulk unit cells along the z-direction. We choose the coordinate system in such a way that the QW is located in the region from  $l_I$  to  $l_2$  ( $0 < l_1 < l_2 < L$ ) and the surrounding material is in the region from 0 to L.

We expand envelopes in PW basis as  $\psi_m(z) = \sum_q W_{mq} a_q$ , where  $a_q(z) = L^{-1/2} \exp(ik_q z)$ are a set of basis functions, and  $k_q = 2\pi q/L$ , with  $q = 0, \pm 1, \pm 2, \pm 3, ... \pm N_{PW}$ , where  $2N_{PW} + 1$  is the number of plane waves. This makes the envelope function periodic in space as  $\psi_m(z) = \psi_m(z+L)$ . Using the condition that  $\psi_m(r)$  are smooth, continuous, infinitely differentiable and slowly varying functions, whose plane-wave expansion is restricted to the 1BZ and  $u_m(r)$  are a complete set of orthogonal Bloch functions at  $\mathbf{k}_0$ , periodic over the whole structure, with the periodicity of Bravais lattice (Lew Yan Voon and Willatzen, 2009. ), we arrive at **k•p** equations for QWs:

$$\sum_{m,q} \left[ \frac{\hbar^{2}}{2m_{0}} (\mathbf{k} - \mathbf{k}_{0})^{2}_{(x,y)} \delta_{sq} + \frac{\hbar^{2}}{2m_{0}} k_{q}^{2} \delta_{sq} + I^{sq}(E_{m}) \right] \delta_{nm} W_{mq} 
+ \sum_{m,q} \left[ \frac{\hbar}{m_{0}} (\mathbf{k} - \mathbf{k}_{0})_{(x,y)} \cdot \mathbf{p}_{nm} \delta_{sq} + \frac{\hbar}{m_{0}} k_{q} \mathbf{e}_{z} \cdot \mathbf{p}_{nm} \right] W_{mq} 
+ \sum_{m,q} H_{nm}^{(2)}(s,q) W_{mq} = E W_{ns} ,$$
(2)

where  $\mathbf{p}_{nm}$  and  $E_m$  are momentum matrix elements and band energies obtained as  $\mathbf{k} \cdot \mathbf{p}$ parameters in bulk for  $\mathbf{k}_0$ ,  $m_0$  is the electron mass, and:

$$\Delta k_{sq} = 2\pi(s - q)/L,$$

$$I^{sq}(E) = (E - E_B)I^{sq}(E) \Big|_{l_2}^{l_1}, E_B = E \pm \Delta E_B,$$

$$I^{sq}(E) \Big|_{l_2}^{l_1} = \frac{1}{L} \int_{l_1}^{l_2} e^{-i\Delta k_{sq}z} dz$$

$$= \frac{l_1 - l_2}{L} \delta_{sq} + \frac{\delta_{sq} - 1}{iL\Delta k_{sq}} \left( e^{-i\Delta k_{sq}l_1} - e^{-i\Delta k_{wq}l_2} \right).$$
(3)

The second-order perturbation band term  $H_{nm}^{(2)}(s,q)$ , which accounts for remote bands r that are not present in the first-order Hamiltonian are:

$$H_{nm}^{(2)}(s,q) = \sum_{r} \frac{1}{L} \int dz \ e^{-ik_{S}z} \frac{(\hbar \mathbf{K} \cdot \mathbf{p}_{nr})(\mathbf{p}_{rn} \cdot \hbar \mathbf{K})}{m_{0}^{2}[(E_{n} + E_{m})/2 - E_{r}]} e^{ik_{q}z}$$

$$= \sum_{\alpha,\beta} \frac{1}{L} \int dz \ e^{-ik_{S}z} \frac{\hbar K_{\alpha}}{m_{0}} P_{nm,\alpha\beta} \frac{\hbar K_{\beta}}{m_{0}} e^{ik_{q}z}$$
(4)

where  $\hbar \mathbf{K} = (\hbar \mathbf{k} - \hbar \mathbf{k}_0)_{(x,y)} + p_z \mathbf{e}_z$ ,  $p_z = -i\hbar \partial_z$  is the momentum operator, and  $P_{nm,\alpha\beta}$  is the second-order  $\mathbf{k} \cdot \mathbf{p}$  momentum tensor. We used n,m for band indices in bulk and  $\alpha$ ,  $\beta$  indices for directions x, y, z.

We assume that the surrounding material has the same parameters as the QW, except for the valence and conduction band energies, that are respectively shifted by  $-\Delta E_B$  and  $+\Delta E_B$  with respect to the QW parameters, where  $\Delta E_B$  is the absolute shift of the bands. This shift is chosen to be large enough to ensure that the wave functions are located in the QW and was set to 10 eV for all our calculations.

Size of the well (surrounding material) is a product of the size of the unit cell in z-direction a and some integer  $N(N_B)$ , l = Na ( $L = N_Ba$ ).  $N_{PW}$  and L/l are the parameters that need to be studied in more detail, and we will show how to determine them in the next section.

In the limit where  $\mathbf{k}$  is a good quantum number, eqn. (2) transforms to the case of bulk by removing every integration over z-components and PWs from envelope function expansion, reducing to:

$$\sum_{m} \left[ \frac{\hbar^{2}}{2m_{0}} (\mathbf{k} - \mathbf{k}_{0})^{2} + E_{m} \right] \delta_{nm} W_{m}$$

$$+ \sum_{m} \left[ \frac{\hbar}{m_{0}} (\mathbf{k} - \mathbf{k}_{0}) \cdot \mathbf{p}_{nm} + H_{nm}^{(2)} \right] W_{m} = E W_{m}, \qquad (5)$$

$$H_{nm}^{(2)} = \sum_{\alpha,\beta} \frac{\hbar (\mathbf{k} - \mathbf{k}_{0})_{\alpha}}{m_{0}} P_{nm,\alpha\beta} \frac{\hbar (\mathbf{k} - \mathbf{k}_{0})_{\beta}}{m_{0}} .$$

Eqn. (2) and eqn. (5) show us how to construct the Hamiltonian, but not which bands and which **k**-point should be used for unperturbed results from DFT. Most of the electronic properties are governed by the symmetry of the crystal and most of the information about the current carriers can be obtained by considering points with the greatest probability for their detection. Extremal states in the electron structure are most likely to have current carriers: holes in the valence band maximum (VBM), and electrons in the conduction band minimum (CBM). Historically, these points and their symmetry have been the center of interest when DFT calculations were not yet computationally feasible, so the electronic

structure was mostly studied by analytical methods in combination with available experimental data. A good overview of these analytical methods can be found in a book by Bir and Pikus, 1974.

The point group of the bulk cubic CsPbBr<sub>3</sub> crystal is  $O_h$ , and the band gap is located at the R-point in the 1BZ. Point group  $O_h$  transforms to a double group, that describes bands when SOC in included, by multiplying all irreducible representations by a spinor representation  $\Gamma^+_{6}$ . Fig. 1 illustrates this for bands around the gap in the bulk CsPbBr<sub>3</sub>. When SOC is not included, VBM at R-point is non-degenerate band corresponding to  $\Gamma_{-2}$ irreducible representation that transforms to 2-fold degenerate band  $\Gamma_7$  when SOC is included. CBM is 3-fold degenerate band at R-point, corresponding to  $\Gamma^{+}_{5}$  when SOC is omitted, and transforms by splitting into a 2-fold  $\Gamma^+_7$  with lower energy, now CBM, and 4fold  $\Gamma_8^+$  band with higher energy, now CBM1. These 8 bands in total make the H8 Hamiltonian.

The larger H26 Hamiltonian is formed when along these 8, we include 3 more valence bands, counting with decreasing energies from VBM: 4-fold  $\Gamma^-_8$ , 2-fold  $\Gamma^-_7$ , and 4-fold  $\Gamma^-_8$ , respectively, and 3 more conduction bands, counting with increasing energies from CBM1: 2-fold  $\Gamma^+_{6}$ , 2-fold  $\Gamma^+_{7}$ , and 4-fold  $\Gamma^+_{8}$ , respectively.

Both H8 and H26 have a unique set of  $\mathbf{k} \cdot \mathbf{p}$  parameters that consist of energies  $E_m$ , momentum matrix elements  $\mathbf{p}_{nm}$  and second-order momentum tensors  $P_{nm,\alpha\beta}$ . Using the same parameters for bulk, we construct the H26 Hamiltonian for QW from eqn. (2), taking note that the periodicity is now valid only in the (x, y) plane.

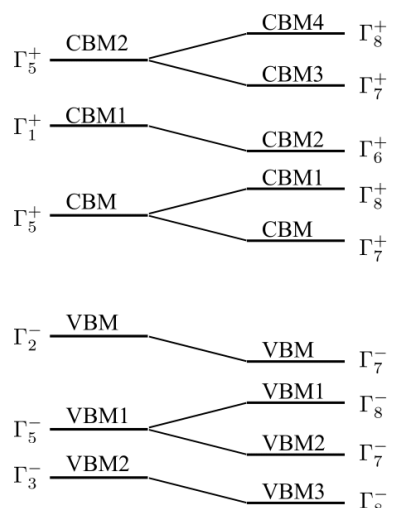
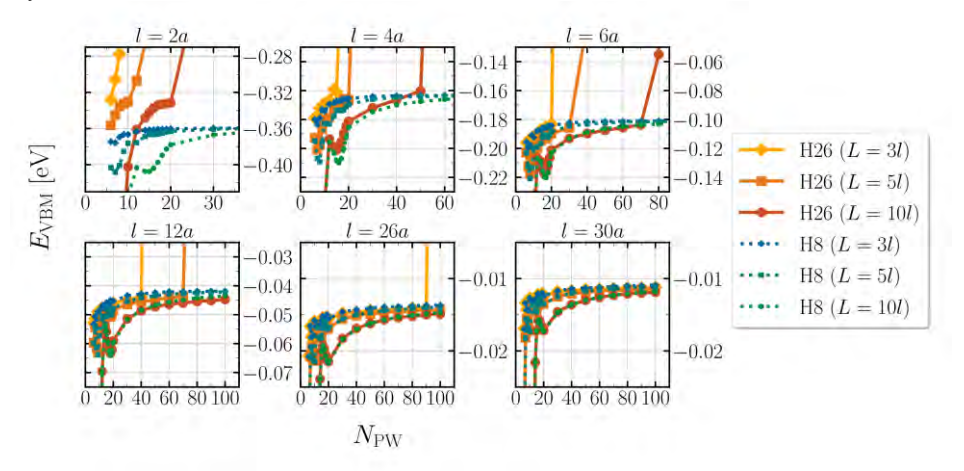


Fig. 1 Ordering of the bands around the gap and their transformation when SOC is included. Distance between the bands does not scale with energy distance between them. Notation for the irreducible representations that was used here follows the one found in Bradley and Cracknell, 2010.

#### 3. RESULTS AND DISCUSSIONS

Depending on the size of the **k•p** Hamiltonian, a small change of numerical parameters L/l and  $N_{PW}$  can have a significant effect on the result. This is especially true for smaller wells, while large wells that approach bulk in terms of size are less sensitive to those changes. For this reason, we inspect the convergence with respect to those parameters as follows. First, we fix some l, and gradually increase the size of the surrounding material L and number of plane waves  $N_{PW}$  until we achieve convergence. This process is repeated for every l.



**Fig.** 2 Energy of VBM as a function of  $N_{PW}$ , in QWs. The results were obtained using H26 (solid lines) and H8 (dotted lines) Hamiltonians, respectively, for QWs of the size l=2a, l=4a, l=6a, l=12a, l=26a, l=30a in units of the lattice constant a. The size of the surrounding material is L=3l (diamonds), L=5l (squares), and L=10l (circles).

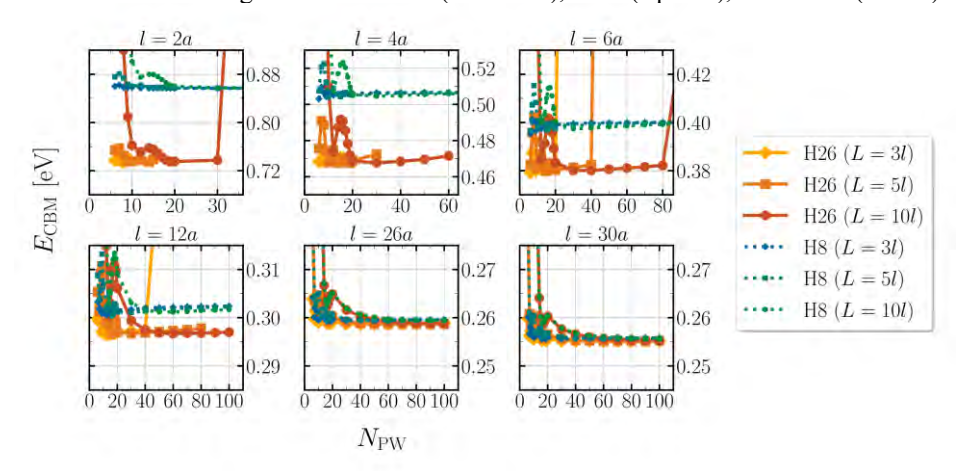


**Fig.** 3 Energy of CBM as a function of  $N_{PW}$ , in QWs. The results were obtained using H26 (solid lines) and H8 (dotted lines) Hamiltonians, respectively, for QWs of the size l=2a, l=4a, l=6a, l=12a, l=26a, l=30a in units of the lattice constant a. The size of the surrounding material is L=3l (diamonds), L=5l (squares), and L=10l (circles).

We will focus on H8 and H26 kep Hamiltonians, both of which we first construct for bulk from DFT results using PBEsol functional as described in Jocić and Vukmirović 2020. and eqn.(2). For DFT calculation we used a 4×4×4 k-grid for electron states, electron kinetic energy cutoff of 50 Ry, and a total of 240 bands for cubic phase of CsPbBr<sub>3</sub> with a lattice constant of a = 11.1  $a_{\theta}$  (where  $a_{\theta}$  is the first Bohr radius). DFT calculations were performed with included SOC. Since we are most interested in the position of VBM and CBM, and therefore the band gap, we will focus our convergence tests on these bands.

In Fig. 2 (Fig. 3) we present the energy of the VBM (CBM), as a function of  $N_{\rm PW}$ , respectively. The resulting band gap is presented in Fig. 4. All three figures show results for small (l = 2a) and l = 4a), intermediate (l = 6a) and l = 12a and l = 26a and l = 30aQWs, respectively.

Although the **k•p** method for OWs itself does not require much computational resources and it can be done, on a single-core desktop computer, it is important to estimate, for every l, at which point increasing L/l and N<sub>PW</sub> does not change the results of the band gap by more than 10 meV. For H8 one usually needs a smaller ratio of L/l, and for L/l = 3, the  $N_{PW}$  of 10, 20, 30, 40 and 40, for l = 2a, l = 4a, l = 12a, l = 26a, and l = 30a, respectively, was sufficient. For H26 one usually needs a larger L/l ratio for smaller wells, while larger wells that approach bulk can have acceptable results for a smaller size of the surrounding material. For l = 2a and l = 4a, it was sufficient to use  $N_{PW} = 16$  and  $N_{PW} = 30$ , respectively with L/l = 10. For l = 6aand l = 12a, it was sufficient to use  $N_{PW} = 20$  and  $N_{PW} = 40$ , respectively with L/l = 5. For l= 26a and l = 30a, it was sufficient to use  $N_{PW} = 30$  and L/l = 3.

For small QWs, the results for band gaps obtained from H8 and H26 can differ as much as 150 meV (see Fig. 4), with H8 overestimating the band gap with respect to H26. For intermediate and large OWs, difference in band gaps between H8 and H26 is still present, although it is much smaller and does not exceed 15 meV and 2 meV, respectively.

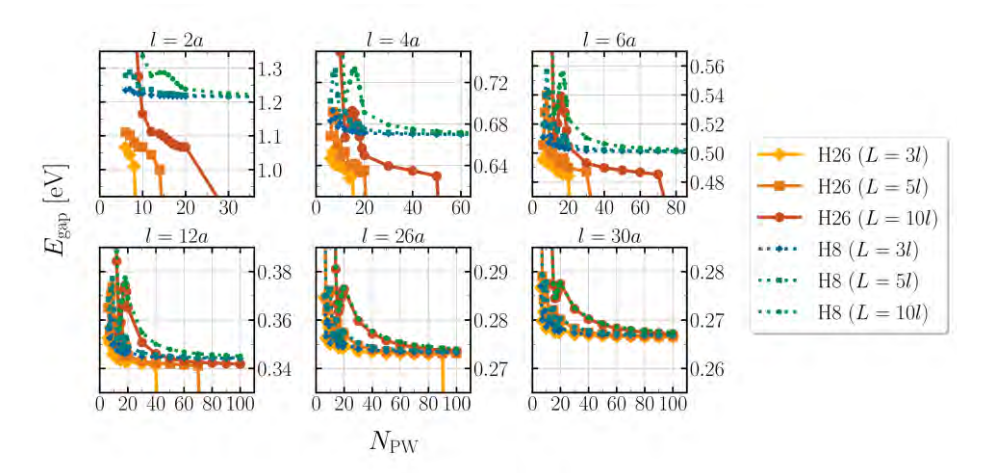
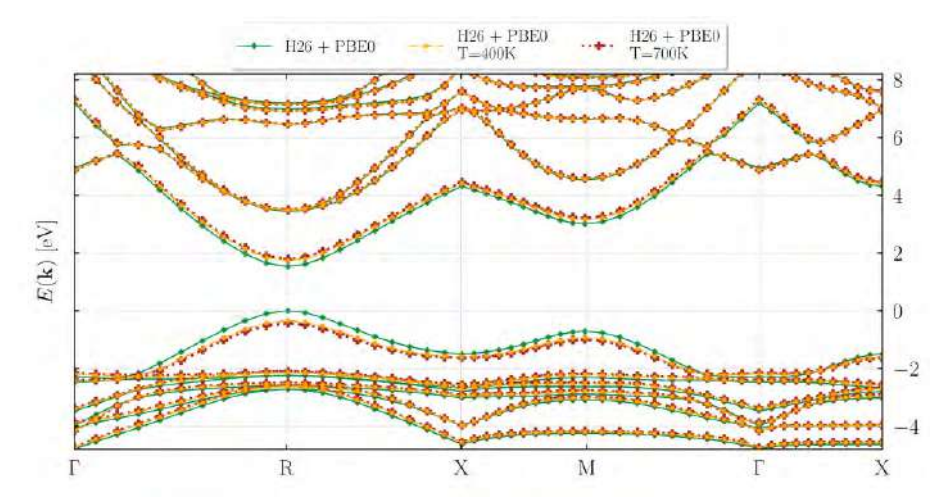
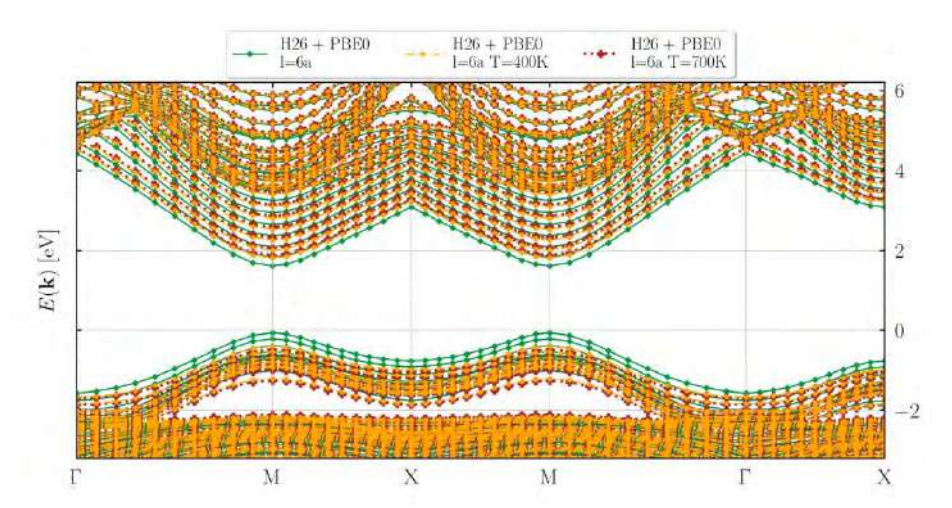


Fig. 4 Energy of the band gap as a function of N<sub>PW</sub>, in QWs. The results were obtained using H26 (solid lines) and H8 (dotted lines) Hamiltonians, respectively, for QWs of the size l=2a, l=4a, l=6a, l=12a, l=26a, l=30a in units of the lattice constant a. The size of the surrounding material is L = 3l (diamonds), L = 5l(squares), and L=10l (circles).



**Fig. 5** The band structure of bulk CsPbBr<sub>3</sub> obtained using H26 Hamiltonians, replacing  $E_m$  with  $E_m^{PBE0}$  (solid line with diamonds) and with  $E_m^{PBE0} + \Sigma_{\rm m}(T)$  correction from SCP calculations at T = 400 K (dash-dot line with circles) and T = 700 K (dotted line with crosses), respectively.



**Fig. 6** The band structure of CsPbBr<sub>3</sub> QW of size l=6a obtained using H26 Hamiltonians replacing  $E_m$  with  $E_m^{PBE0}$  (solid line with diamonds) and with  $E_m^{PBE0} + \Sigma_{\rm m}(T)$  correction from SCP calculations at T=400 K (dash-dotted line with circles) and T=700 K (dotted line with crosses), respectively.

In eqn. (2), we restrict envelope functions to the expansion on plane-waves only in the 1BZ. Therefore, in the general case, one would expect some kind of divergence for both H8 and H26, when  $N_{\rm PW} > L/a$  or equivalently when  $N_{\rm PW} > N_{\rm B}$ . However, due to having much less parameters than H26, H8 seems to be stable even when  $N_{\rm PW} > N_{\rm B}$  unlike H26

which shows divergence in this case, as seen in Fig. 2, Fig. 3 and Fig. 4. We also note that H8 always converges before  $N_{\rm PW}$  exceeds the limits of the 1BZ. However, for large wells, both H8 and H26 require less plane-waves than are needed to fill the whole 1BZ, in order to calculate the band gap. For these reasons, we can also check the convergence, by fixing the  $N_{PW} = N_{B}$  to always include all plane-waves in the 1BZ, while only increasing the size ratio of the surrounding material and the OW L/l, and then checking if the resulting band gap changes with reduction of  $N_{PW}$ .

Since DFT has a well-documented problem that it typically underestimates the band gaps (Perdew, 1985.), we can improve our kep results by replacing DFT bulk PBEsol energies with the ones obtained using PBE0 (Perdew, 1996.) to obtain a more accurate gap. To include the temperature correction, we add the electron self-energy correction  $\Sigma_m(T)$ that comes from the electron-phonon interaction. When calculating PBE0 energies  $E_m^{PBE0}$ , we used the same numerical parameters as previously mentioned for PBEsol, with the addition of  $4\times4\times4$  q-grid for sampling the required Fock operator and we used the Gygi-Baldereschi method to treat the singularity at  $q \to 0$ . Results for  $\Sigma_m(T)$  were used from our recent paper (Jocić and Vukmirović 2023.), where we used the maxima of the spectral function from SCP method to obtain band energy corrections. The results are available for temperatures from T = 400 K to T = 700 K.

In eqn. (5), we replace all  $E_m$  with  $E_m^{PBE0}$ , for H26 without temperature correction, and with  $E_m^{PBE0} + \Sigma_{\rm m}(T)$  for T = 400 K and T = 700 K, respectively, to include temperature effects in bulk. The resulting band dispersion plot is presented in Fig. 5. As expected from our recent work the biggest shift in energies is observed for VBM and CBM (when comparing against other bands that form H26), which effectively gives the band gap of 2.08 eV and 2.23 eV at T = 400K and T = 700K, respectively, and 1.5 eV without the  $\Sigma_m(T)$ . Inserting the same parameters in eqn. (2), we obtained the band gaps of 1.67 eV, 2.21 eV and 2.35 eV, respectively for QW of size l = 6a with its band dispersion shown in Fig. 6.

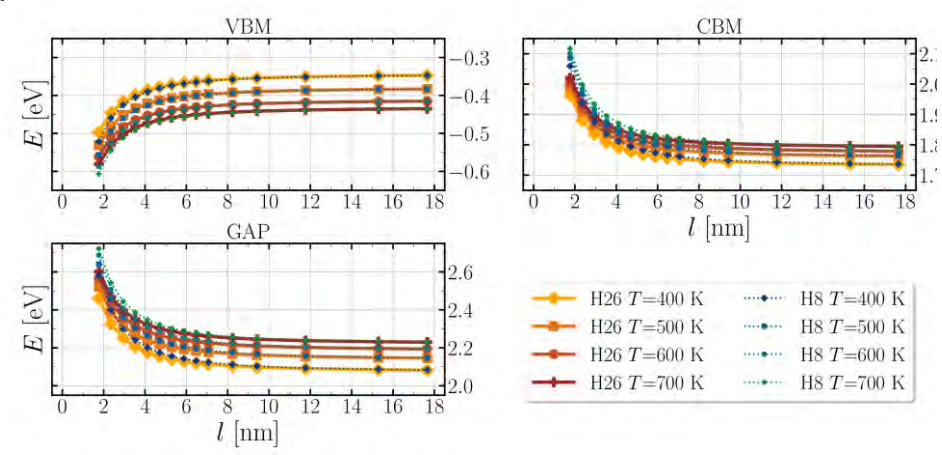


Fig. 7 Energies of VBM, CBM and band gaps for CsPbBr<sub>3</sub> QW as a function of the size of the QW l, obtained using H26 Hamiltonian (solid lines) and H8 (dotted lines) when  $E_m$  is replaced by  $E_m^{PBE0} + \Sigma_m(T)$ , at temperatures of T = 400 K(diamonds), T = 500 K (squares), T = 600 K (circles), T = 700 K (crosses).

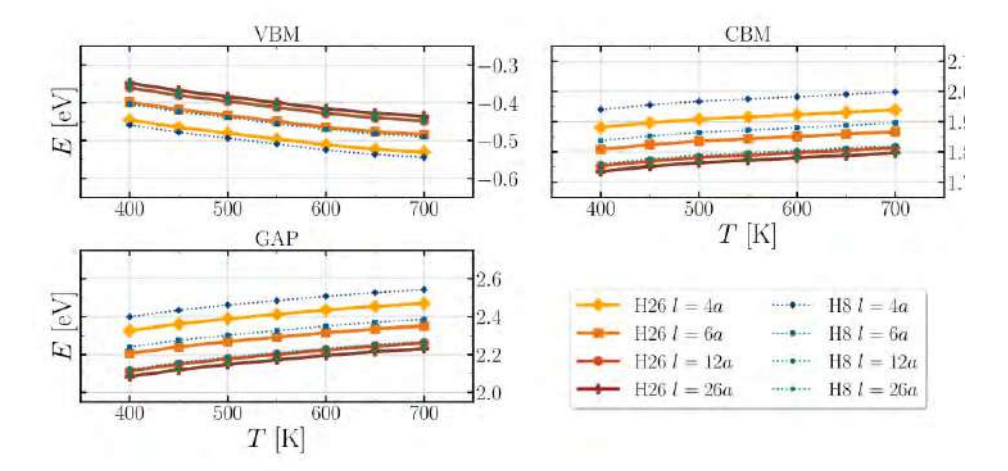


Fig. 8 Energies of VBM, CBM and band gaps for CsPbBr<sub>3</sub> QW as a function of temperature T, obtained using H26 Hamiltonian (solid lines) and H8 (dotted lines) when  $E_m$  is replaced by  $E_m^{PBE0} + \Sigma_m(T)$ , respectively for several sizes of QWs l = 4a (diamonds), l = 6a (squares), l = 12a (circles), l = 26a (crosses) in units of lattice constant a.

Finally, we present the temperature dependence of QW band gaps using H26 and H8 Hamiltonians. We calculated how energies of VBM, CBM, and the band gap change with the size of the QW and temperature, respectively. The E=0 level is the one VBM takes for the bulk phase with  $E_m^{PBE0}$  energy set. Consistent with the previous figures, H26 and H8 give almost identical results for intermediate and large QWs, while they show a slight discrepancy for small QWs.

Fig. 7 shows energies of VBM, CBM, and band gaps, respectively, as a function of QW size l, starting from l=2a and going to l=30a for several temperatures that range from 400 to 700 K. From this figure we can conclude that the energies of the bands and therefore the gap change significantly with the increase of the QW size until certain point (around 8 nm), after which the results very slowly approach the same ones found in the bulk phase.

Fig. 8 shows energies of VBM, CBM, and band gaps, respectively, for temperatures from T = 400 K to T = 700 K for several QW sizes of l = 4a, l = 6a, l = 12a, and l = 26a. From this figure we can see that the relative change of energies with temperature is similar for all sizes of QWs and again similar for bulk when compared to results from Jocić and Vukmirović 2023.

#### 4. CONCLUSION

In this work, we demonstrated a procedure for obtaining convergence with respect to numerical parameters used for H8 and H26  $\mathbf{k} \cdot \mathbf{p}$  Hamiltonians for QWs like the size ratio of the surrounding material and the QW of width L/l and the number of plane waves in the envelope function expansion  $N_{\text{PW}}$ , relying on the procedure used in Jocić and Vukmirović 2020. We demonstrated that even when H8 shows no divergence for  $N_{\text{PW}} > N_{\text{B}}$ , the results do not change from the ones that take all plane-waves in the 1BZ. The H26 produces

diverging results whenever  $N_{\rm PW} > N_{\rm B}$ , but for large QWs a good result can be obtained when  $N_{\rm PW} < N_{\rm B}$ . We obtained a band dispersion with improved value for the band gap for bulk and QW, using H26 and replacing PBEsol energies  $E_m$  with PBE0 energies  $E_m^{PBE0}$  and then introducing the temperature effects from electron self-energy corrections  $\Sigma_m(T)$ , obtained from spectral function maxima, as in Jocić and Vukmirović 2023. Finally, we obtained results for the temperature dependence of band gaps for QWs using the **k•p** method. Band gap results were obtained for wells in the range from l = 2a to l = 30a, and for the temperatures from 400 K to 700 K. This way, we showed how the band gap of the QWs changes with size and temperature in the case of perovskite CsPbBr<sub>3</sub> in cubic form.

**Acknowledgments**. We acknowledge funding provided by the Institute of Physics Belgrade, through the grant by the Ministry of Science, Technological Development and Innovation of the Republic of Serbia. Numerical computations were performed on the PARADOX-IV supercomputing facility at the Scientific Computing Laboratory, National Center of Excellence for the Study of Complex Systems, Institute of Physics Belgrade.

#### REFERENCES

Bir, G., Pikus, G., Symmetry and Strain-induced Effects in Semiconductors, Wiley, New York, 1974.

Bradley, C., Cracknell, A., The Mathematical Theory of Symmetry in Solids: Representation Theory for Point Groups and Space Groups, Oxford University Press, Oxford 2010.

Jocić, M., Vukmirović, N., 2020. Phys. Rev. B, 102, 085121. doi: 10.1103/PhysRevB.102.085121

Jocić, M., Vukmirović, N., 2023. Phys. Chem. Chem. Phys., 25, 29017-29031, doi: 10.1039/D3CP02054A

Lew Yan Voon, L. C., Willatzen, M., The k\*p Method: Electronic Properties of Semiconductors, Springer-Verlag, Berlin Heidelberg, 2009.

Löwdin, P., 1951. J. Chem. Phys., 19, 1396–1401, doi: 10.1063/1.1748067

Perdew, J. P., 1985. Int. J. Quantum Chem., 28, 497–523, doi: 10.1002/qua.560280846

Perdew, J. P., Burke, K., Emzerhof, M., 1996. Phys. Rev. Lett., 77, 3865–3868, doi: 10.1103/PhysRevLett.77.3865

#### TEMPERATURSKA ZAVISNOST ELEKTRONSKOG ENERGETSKOG PROCEPA KVANTNIH JAMA CsPbBr3 DOBIJENIH POMOĆU k•p METODA

Izračunali smo elektronsku strukturu CsPbBr3 kvantne jame pomoću k•p modela korišćenjem parametara iz DFT proračuna na bazi hibridnih funkcionala sa dodatkom korekcija za self-energije koje potiču od elektron-fonon interakcije. Dobili smo temperatursku zavisnost procepa za različite veličine kvantne jame. Rezultati pokazuju da je temperaturska zavisnost u kvantnim jamama, za sve veličine jama koje su uzete u obzir, slična onoj koja se dobija za balk fazu.

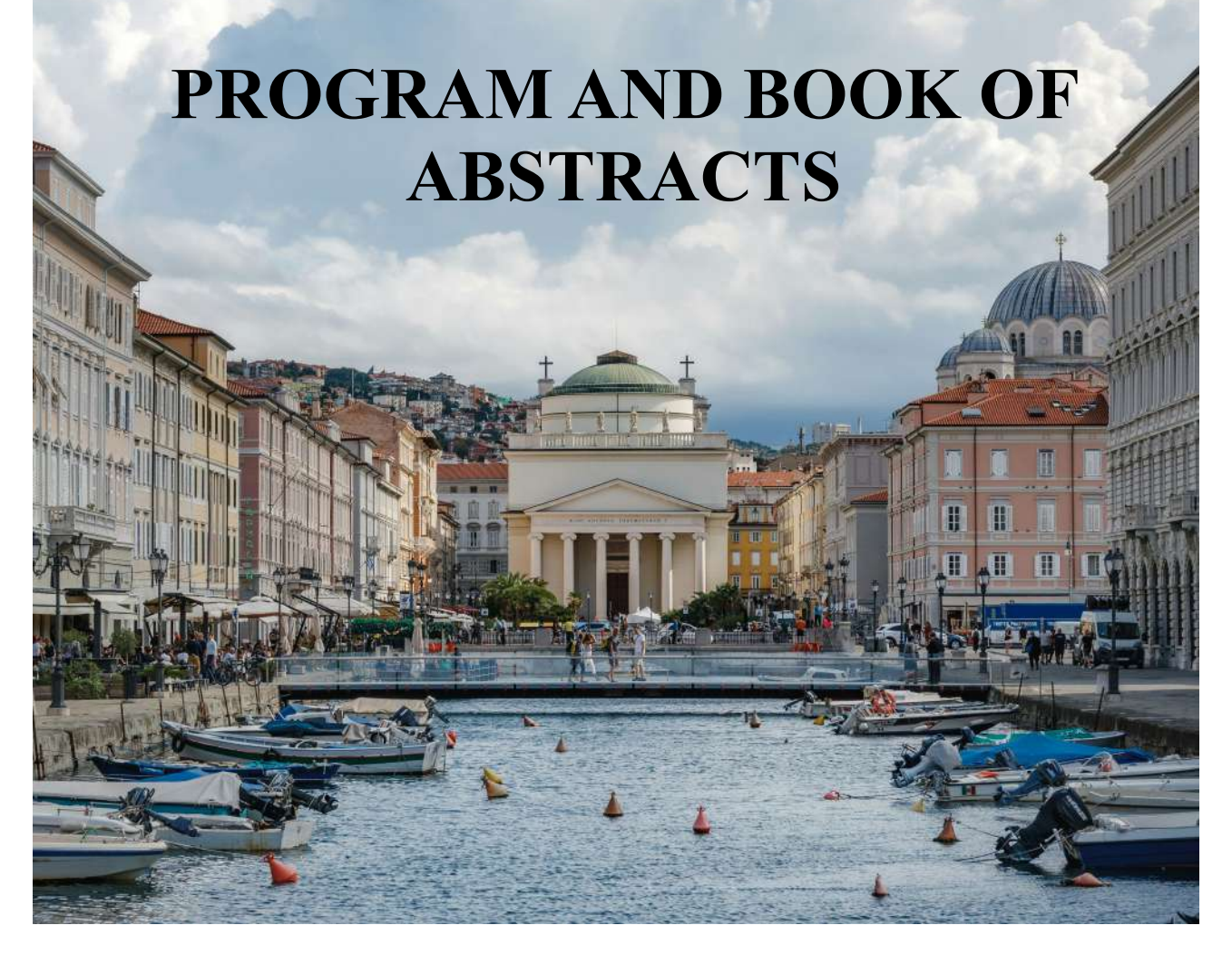
Ključne reči: nanostrukture, temperaturska zavisnost, kvantne jame, k•p metod.

# Прилог 2:

# Доказ о научним публикацијама категорије М34



The 21st Young Researchers' Meeting 26-30 May 2025, Trieste, Italy.











#### **Website and Contact**

https://sites.google.com/view/yrm2025/home You can contact us at yrm2025organizers@gmail.com.

#### **Venue & Conference Room**

SISSA – Scuola Internazionale Superiore di Studi Avanzati – was founded in 1978 and is a scientific center of excellence within the national and international academic scene. The SISSA campus is located in Opicina (Trieste), in Via Bonomea 265. It can easily be reached via public transportation, which connects the campus to downtown Trieste (at 4 km only), or via highway. Main options are taking the bus line 38 or tram 2. Tickets must be purchased beforehand at newsstands or tobacconists or tickets machines on Trieste streets and must be validated using the machines on the buses. There are single-run tickets, 10-run tickets or transit pass (biweekly, monthly, for the whole buses transport system). It's not possible to buy tickets on board. For more information on how to reach SISSA, please visit https://www.sissa.it/about/how-reach-us.

SISSA building may be entered through two entrances: main entrance on level 0 and a back entrance on level 2 (note that the back entrance requires badge access). From the main entrance, the venue (Room 005) is easily reached on the ground floor by walking straight forward past the reception desk. It may be found next to Room 004, visible as one enters through the main entrance. From the back entrance on the second floor, it's necessary to take the staircase or elevator to the ground floor, which may be accessed to either the left or right as one enters through the back entrance. Reaching the ground floor, one may find Room 005 in the area straight below the back entrance, next to the reception desk.

#### Hotels

#### Opera Figli del Popolo

Easily accessible from the city center and the Trieste train station, Opera Figli del Popolo is located at *Largo Papa Giovanni XXIII*, 7, *Salita dei Montanelli*, 1/1. To reach the conference from the hotel, you will need to transfer to bus line 38 (through which passes by SISSA.

#### Le Terrazze

Located right at the city center, Le Terrazze is located at *Via Fabio Filzi, 21*. To reach the conference from the hotel, you will need to take the bus 38 which reaches SISSA in 15 minutes.

### **Organizers**

Muhammed H. Gunes, <u>muhammed.gunes@polytechnique.edu</u>, École Polytechnique, Palaiseau, France.

Alessia Muroni, <u>alessia.muroni@uniroma2.it</u>, University of Rome "Tor Vergata", Rome, Italy. Gabriele Fabbro, <u>gfabbro@irsamc.ups-tlse.fr</u>, Laboratoire de Chimie et Physique Quantique, Université Toulouse III - Paul Sabatier, Toulouse, France.

Marie Tardieux, <u>m.c.s.tardieux@uva.nl</u>, Institut of Physics, University of Amsterdam, Netherlands. Sarbajit Dutta, <u>sarbajit.dutta@polytechnique.edu</u>, Ecole Polytechnique, Paris, France.

Erik Linnér, <u>elinner@sissa.it</u>, Scuola Internazionale Superiore di Studi Avanzati (SISSA), Trieste, Italy.

### Sponsors and acknowledgement

We are truly grateful for our sponsors and their generous support which makes this edition of YRM possible. This study has been (partially) supported through the EUR grant NanoX n° ANR-17-EURE-0009 in the framework of the "Programme des Investissements d'Avenir".









# **Detailed Program**

	Monday	Tuesday	Wednesday	Thursday	Friday
	Electronic Structure and Method Development		Optical Properties of Materials	Strongly Correlated Systems and Magnetism	High Performance Computing
8:30 - 9:30	Registration & Welcome Talk				
9:30 - 10:30	Tommaso Nottoli	Maryam Azizi	Marta Monti	Francesca Paoletti	Aleksandar Zivkovic
10:30 - 10:55	Coffee break	Coffee break	Coffee break	Coffee break	Coffee break
10:55 - 11:20	Flash presentations	Advancing Photoemission Spectra Analysis with Three-Body Green's Function Formalism Emma Nogué	Computational and Experimental Investigation of Curcumin Derivatives as Potential Photosensitizers for Photodynamic Therapy  Ali Ghiami-Shomami	Extended Hubbard functionals insight on transition-metal oxides for sodium-ion batteries  Domenico Corona	Exploiting Parallelism for Fast Feynman Diagrammatics John Sturt
11:20 - 11:45	Computing the one-body reduced density matrix with Quantum Monte Carlo for solids  Carlos Rodriguez Perez	Exploring superconducting nickelates electronic structures with the GW approximation  Jean-Baptiste de Vaulx	Finite momentum excitons in scintillating materials and their implications for dark matterelectron scattering  Nora Taufertshöfer	Bouncing-ball quantum scars in two-dimensional systems Simo Selinummi	Fabio Caleffi
11:45 - 12:10	First-principles study of Bi(trimer) on a Ge(111) surface  Montserrat Navarro Espino	Simulations of the Thorium Nuclear Clock  Martin Pimon  Vibrational Properties of Materials and Transport	Optical properties of anisotropic excitons in GeS  Mehdi Arfaoui	Revealing spinons by proximity effect  Antonio Maria Tagliente	Industry session
12:10 - 13:40	Lunch break	Lunch break	Lunch break	Lunch break	Closing remarks
13:40 - 14:40	Abdallah El Sahili	Ivan Maliyov (online)	Elisa Serrano Richaud	Pauline Besserve	Ü
14:40 - 15:05	Benchmark study of many-body methods for the prediction of band alignment at hetero-interfaces, using 1D Hubbard models	Scartronics: Boosting Quantum Transport in Two-Dimensional Systems with Variational Scarring Fartash Chalangari	Optical Absorption in Indirect Semiconductor to Semimetal PtSe2 Arises from Direct Transitions	Local classical correlations between physical electrons Gabriele Bellomia	End of Conference
15:05 - 15:30	Jean Goossaert  Coffee break	Coffee break	Sabrine Ayari  Coffee break	Coffee break	
15:30 - 15:55	Temperature dependence of band gaps of inorganic halide perovskites  Milan Jocic	From Symmetry to Stability: Structural and Electronic Transformation in Cs2KInI6  Mohammad Bakhsh	Unveiling the Role of Electron-Phonon Scattering in High-Order Harmonics  Thomas Lettau	Altermagnetism from interaction-driven itinerant magnetism  Samuele Giuli	
15:55 - 16:20	From single bond to line defects: a case study from a novel two-dimensional network-forming material  Marco Dirindin	Structural phase transitions in monolayer TMDs with a neural-network interatomic potential  Davide Bidoggia	Electronic properties of 2D Transition Metal Dichalcogenides : an ab initio study confirmed by experiment  Felana Andriambelaza		
16:20 - 16:45		Chaotic dynamics creates and destroys branched flow  Esko Toivonen	Sum frequency generation from real-time simulation in 2D crystals Mike Pionteck	Social debate	
16:45 - 18:00	Social event  Hiking to Castelletto di Miramare (through Strada Napoleonica)	Coffee break & poster session			
18:00 - 20:00					
20:00 -				Social dinner @ Suban	

### Temperature dependence of band gaps of inorganic halide perovskites

M. Jocić<sup>1</sup>, N. Vukmirović<sup>1</sup>

<sup>1</sup>Institute of Physics Belgrade, University of Belgrade, Pregrevica 118, 11080 Belgrade, Serbia

Recently, halide perovskites have been praised for their low-cost and high performance capabilities. However, in order to give reliable and accurate predictions on their performance and stability using *ab-initio* methods, one should first provide an adequate description of their electronic structure.

Reasonably accurate band gaps can be obtained using conventional DFT with local or semi-local functionals but this is a result of error cancellation due to the neglect of spin-orbit coupling (SOC) effects. Using hybrid functionals with full SOC treatment still yields an underestimated value of the band gap. In order to get correct results of the band gap, temperature effects caused by electron-phonon interaction must also be included.

We propose a combination of DFT with hybrid PBE0 functional, combined with Allen-Heine-Cardona (AHC) method, and the evaluation of anharmonic phonon frequencies using self-consistent phonon method [1]. We also propose a way to account for energy level renormalization and broadening at the same time by utilizing a procedure based on self-consistent Migdal approximation. Obtained results for CsPbX<sub>3</sub> (X=Cl, Br, I) halide perovskite band gaps for bulk crystals cover a wide range of temperatures which can be compared with experimental data, as seen in Figure 1.

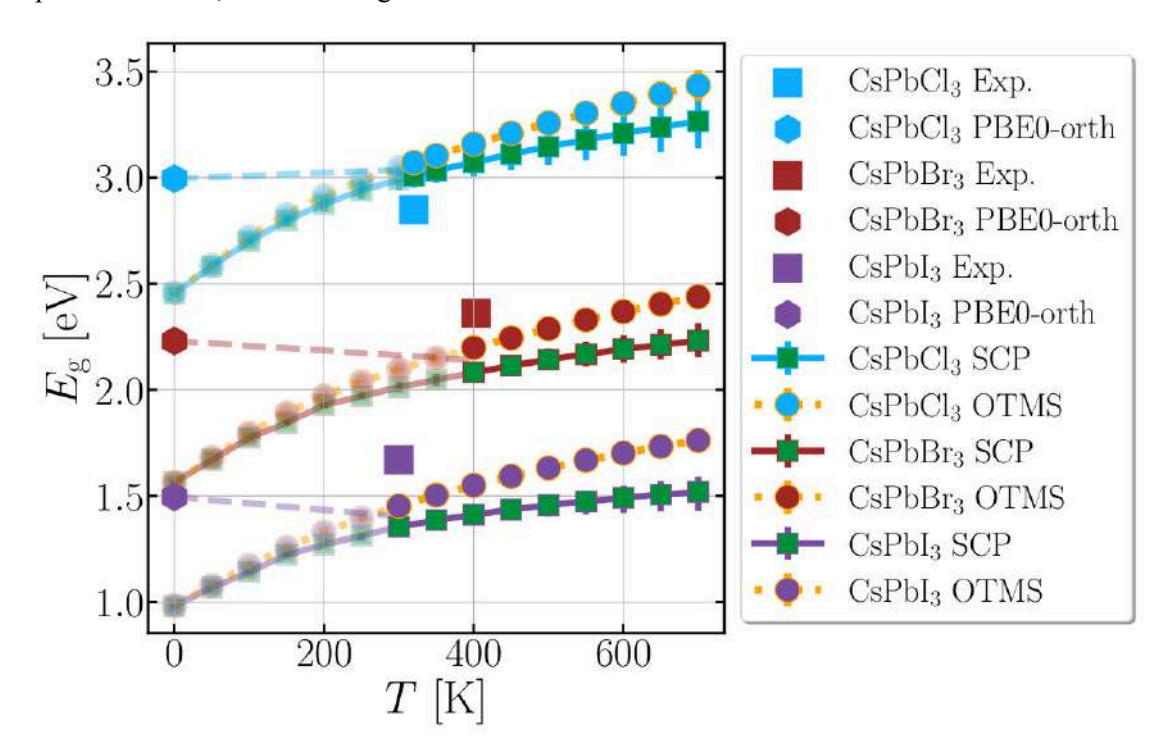


**Figure 1:** Band gaps of CsPbX<sub>3</sub> (X=Cl, Br, I) obtained using DFT with PBE0 hybrid functional and AHC correction for temperature effects compared with experimental values (disconnected squares). Results are obtained using on-the-mass-shell (OTMS) approximation (circles) and more refined self-consistent procedure (SCP) based on self-consistent Migdal approximation (connected squares). Zero temperature calculations were performed on an orthorhombic structure (hexagons), while temperature corrections were added on results with cubic phase. Lines and symbols at temperatures above (below) the formation of the cubic phase are shown as opaque (transparent) for each material.

#### References

[1] M. Jocić, N. Vukmirović, *Phys. Chem. Chem. Phys.* **25**, 29017 (2023).



Contribution ID: 188 Contribution code: S06-CMPSP-108 Type: Oral presentation

# Ab-initio calculations of the temperature-dependent band gap of inorganic halide perovskites

Tuesday, August 30, 2022 5:15 PM (15 minutes)

Inorganic metal-halide perovskites have drawn much attention as candidates for producing low cost high-performance solar cells having efficiency reported as high as 20% in single-junction architecture. Their electronic and structural properties have been the case of intense study in both experimental setups and computational simulations. Since solar cells are expected to perform outside of such laboratory conditions, it is important to have an understanding of how their performance will be affected by their surroundings. Temperature is the main parameter which governs both the crystal and the electronic structure of inorganic metal-halide perovskites. Theoretical approaches that rely on either Monte-Carlo sampling of vibrational states [1] or classical molecular dynamics [2] have been successful to some extent. However, quantum mechanical abinitio studies that yield accurate temperature dependence of band gaps of inorganic halide perovskites are still lacking.

In this work, we perform such studies for  $CsPbC_3$ ,  $CsPbBr_3$  and  $CsPbI_3$ . First, we use the density functional theory (DFT) with PBEsol exchange-correlation functional to obtain a decent starting estimate at zero temperature. Such an approach has a well-known error of underestimating the band gap. To overcome this, we employ the PBE0 hybrid functional whose parameters are chosen to enforce Koopman's condition for localized defect states [3]. Second, we include the effects of electron-phonon interaction that depend on the temperature of the material using the Allen-Heine-Cardona (AHC) theory [4]. Phonon modes are obtained from density functional perturbation theory, that in the present case produces unphysical imaginary frequencies in the phonon spectrum due to the harmonic approximation. We overcome this issue by calculating the phonon spectrum using the self-consistent phonon method that accounts for the effects of anharmonicity [5]. We obtain the electronic band gaps for the cubic phase of  $CsPbCl_3$ ,  $CsPbBr_3$ , and  $CsPbI_3$ , at temperatures of 320, 403, and 300 K, respectively, of 3.07, 2.30, and 1.70 eV. These results differ by no more than 0.25 eV from the experimental ones found in the literature.

#### References

- 1. W. A. Saidi et al, J. Phys. Chem. Lett. 2016, 7, 5247-5252
- 2. J. Wiktor et al, J. Phys. Chem. Lett. 2017, 8, 5507-5512
- 3. T. Bischoff et al, Phys. Rev. Mater. 2019, 3, 123802
- 4. S. Ponce et al, J. Chem. Phys. 2015, 143, 102813
- 5. Y.N. Wu et al, J. Phys. Chem. Lett. 2020, 11, 2518-2523

**Primary authors:** JOCIĆ, Milan (Institute of Physics Belgrade, University of Belgrade, Serbia); VUKMIROVIC, Nenad (Institute of Physics Belgrade, University of Belgrade, Serbia)

Presenter: JOCIĆ, Milan (Institute of Physics Belgrade, University of Belgrade, Serbia)Session Classification: S06 Condensed Matter Physics and Statistical Physics

Track Classification: Scientific Sections: S06 Condensed Matter Physics and Statistical Physics





# **BPU11 CONGRESS**

28 August 2022 - 1 September 2022

# **Book of Abstracts**

**Editors:** Antun Balaž, Goran Djordjević, Jugoslav Karamarković, Nenad Lazarević

#### **BPU11 CONGRESS**

The 11th International Conference of the Balkan Physical Union **The Book of Abstracts** 

#### **Editors:**

Antun Balaž, Goran Djordjević, Jugoslav Karamarković, Nenad Lazarević

Technical Editor: Milan Milošević

Cover Design: Elena Denda

Printed by: Planeta Print, Belgrade

ISBN: 978-86-7025-950-8

Print run: 350

#### **International Advisory Committee**

- Petar Adžić (Belgade, Serbia)
- Gediz Akdeniz (Istanbul, Turkey)
- Ignatios Antoniadis (Paris, France / Bern, Switzerland)
- Metin Arik (Istanbul, Turkey)
- Pervin Arıkan (Ankara, Turkey)
- · Istvan Bikit (Novi Sad, Serbia)
- · Neven Bilić (Zagreb, Croatia)
- Madalin Bunoiu (Timisoara, Romania)
- · Florin Buzatu (Bucharest, Romania)
- · Luisa Cifarelli (Bologna, Italy)
- · Victor Ciupina (Constanta, Romania)
- Radu Constantinescu (Craiova, Romania / BPU VP), co-chair
- · Atish Dabholkar (Trieste, Italy), TBC
- Brunilda Daci (Tirana, Albania)
- Milan Damnjanović (Belgrade, Serbia)
- Antoneta Deda (Tirana, Albania)
- · Polikron Dhoqina (Tirana, Albania)
- · Vladimir Dobrosavljević (Tallahassee, FL, USA)
- Mahmut Dogru (Elazığ, Turkey)
- Branko Dragović (Belgrade, Serbia)
- Vladimir Dragović (Dallas, USA/ MI SANU Belgrade, Serbia)
- · Alexander Dreischuh (Sofia, Bulgaria)
- Sondan Durukanoglu Feyiz (Istanbul, Turkey)
- Elcin Ekdal Karali (Izmir, Turkey)
- · Mitko Gaydarov (Sofia, Bulgaria)
- · Ana Georgieva (Sofia, Bulgaria)
- · Mihai Girtu (Constanta, Romania)
- İbrahim Halil Mutlu (Antalya, Turkey)
- Fedor Herbut (Belgrade, Serbia), TBC
- Tristan Hübsch (Washington, DC, USA / Novi Sad, Serbia)
- · Gregorios Itskos (Nicosia, Cyprus)
- Branislav Jelenković (Belgrade, Serbia)
- · Zoran Knežević (Belgrade, Serbia)
- Ljupčo Kocarev (Skopje, North Macedonia)
- · Nikola Konjević (Belgrade, Serbia), TBC
- · Latchesar Kostov (Dubna, Russia)
- Danica Krstovska (Skopje, North Macedonia)
- Dhurata Kuqi (Tirana, Albania)
- Ivan Lalov (Sofia, Bulgaria)
- Ivan Mančev (Niš, Serbia)
- Jovan Mirković (Podgorica, Montenegro)
- Xenophon Moussas (Athens, Greece)
- · Dragoslav Nikezić (Kragujevac, Serbia)
- · Yeşim Öktem (Istanbul, Turkey)

- Blerina Papajani (Elbasan, Albania)
- Alexander Petrov (Sofia, Bulgaria)
- Zoran Petrović (Belgrade, Serbia)
- Stevan Pilipović (Novi Sad, Serbia), TBC
- · Stefan Pokorski (Warsaw, Poland)
- · Zoran Popović (Belgrade, Serbia), co-chair
- Zoran Radović (Belgrade, Serbia)
- Petra Rudolf (Groningen, Netherlands / EPS)
- Miljko Satarić (Belgrade, Serbia)
- Dejan Stojković (Buffalo, NY, USA)
- Đorđe Šijački (Belgrade, Serbia), TBC
- Milan Tadić (Belgrade, Serbia)
- Efstratios Theodossiou (Athens, Greece)
- Ion Tiginyanu (Chişinău, Moldova)
- Viktor Urumov (Skopje, North Macedonia)
- Evgeniya Valcheva (Sofia, Bulgaria)
- Mihai Visinescu (Bucharest, Romania)
- · Gerti Xhixha (Tirana, Albania)
- Oliver Zajkov (Skopje, North Macedonia)
- Christos Zerefos (Athens, Greece)

#### **International Scientific Committee**

- · Antun Balaž (Belgrade, Serbia), co-chair
- · Jugoslav Karamarković (Niš, Serbia), co-chair
- · Nenad Lazarević (Belgrade, Serbia), co-chair

#### 1. Nuclear Physics and Nuclear Energy

- Daniel Andreica (Cluj-Napoca, Romania)
- Burcu Cakirli Mutlu (Istanbul, Turkey)
- Igor Čeliković (Belgrade, Serbia), coordinator
- · Dimitrije Maletić (Belgrade, Serbia), secretary
- · Georgi Raynovski (Sofia, Bulgaria)
- Svetislav Savović (Kragujevac, Serbia)
- Erjon Spahiu (Tirana, Albania)

#### 2. Astronomy and Astrophysics

- Vesna Borka (Belgrade, Serbia)
- Gojko Đurašević (Belgrade, Serbia)
- Mimoza Hafizi (Tirana, Albania)
- Gordana Jovanović (Podgorica, Montenegro)
- Milan Milošević (Niš, Serbia)
- Jelena Petrović (Belgrade, Serbia)
- Marius Piso (Bucharest, Romania)
- Luka Popović (Belgrade, Serbia), coordinator

- · Evgeni Semkov (Sofia, Bulgaria)
- · Saša Simić (Kragujevac, Serbia)
- Nikolaos Spyrou (Thessaloniki, Greece)
- · Vladimir Srećković (Belgrade, Serbia), coordinator
- · Dejan Urošević (Belgrade, Serbia)

#### 3. Gravitation and Cosmology

- · Duško Borka (Belgrade, Serbia)
- · Dragoljub Dimitrijević (Niš, Serbia), secretary
- · Mimoza Hafizi (Tirana, Albania)
- Predrag Jovanović (Belgrade, Serbia)
- · Kostas Kleidis (Thessaloniki, Greece)
- Voja Radovanović (Belgrade, Serbia)
- · Zoran Rakić (Belgrade, Serbia)
- · Marko Vojinović (Belgrade, Serbia), coordinator
- Dumitru Vulcanov (Timisoara, Romania)
- Stoycho Yazadzhiev (Sofia, Bulgaria)

#### 4. Atomic and Molecular Physics

- · Tasko Grozdanov (Belgrade, Serbia)
- Lucian Ion (Bucharest, Romania)
- Slavoljub Mijović (Podgorica, Montenegro)
- · Nenad Milojević (Niš, Serbia), secretary
- Asen Pashov (Sofia, Bulgaria)
- Violeta Petrović (Kragujevac, Serbia), coordinator
- · Igor Savić (Novi Sad, Serbia), coordinator
- Nenad Simonović (Belgrade, Serbia)

#### 5. High Energy Physics (Particles and Fields)

- Tatjana Agatonović Jovin (Belgrade, Serbia)
- Calin Alexa (Bucharest, Romania)
- Biljana Antunović (Banja Luka, Bosnia and Herzcegovina)
- Ion Cotaescu (Timisoara, Romania)
- Dragoljub Dimitrijević (Niš, Serbia), secretary
- Magdalena Đorđević (Belgrade, Serbia)
- Miloš Đorđević (Belgrade, Serbia)
- Plamen Iaydjiev (Sofia, Bulgaria)
- · Predrag Milenović (Belgrade, Serbia), coordinator
- Rudina Osmanaj (Tirana, Albania)
- · Fotios Ptochos (Nicosia, Cyprus)
- · Voja Radovanović (Belgrade, Serbia)
- Nataša Raičević (Podgorica, Montenegro)
- · Ömer Yavas (Ankara, Turkey)
- · Lidija Živković (Belgrade, Serbia), coordinator

#### 6. Condensed Matter Physics and Statistical Physics

- · Miroslav Abrashev (Sofia, Bulgaria)
- Antun Balaž (Belgrade, Serbia)
- Jelena Belošević-Čavor (Belgrade, Serbia), coordinator
- Željka Cvejić (Novi Sad, Serbia), coordinator

- Zorana Dohčević-Mitrović (Belgrade, Serbia)
- Sinasi Ellialtioglu (Ankara, Turkey)
- Cristian Enachescu (Iasi, Romania)
- Oguz Gulseren (Ankara, Turkey)
- · Sanja Janićević (Kragujevac, Serbia)
- · Nataša Jović Orsini (Belgrade, Serbia)
- · Nenad Lazarević (Belgrade, Serbia)
- Panos Patsalas (Thessaloniki, Greece)
- · Dušan Popović (Belgrade, Serbia)
- · Vadim Sirkeli (Chişinău, Moldova)
- Nicolaos Toumbas (Nicosia, Cyprus)
- Daniel Vizman (Timisoara, Romania)
- George Vourlias (Thessaloniki, Greece)
- · Nenad Vukmirović (Belgrade, Serbia), coordinator
- Tatjana Vuković (Belgrade, Serbia)

#### 7. Optics and Photonics

- Petar Atanasov (Sofia, Bulgaria)
- Tudor Braniste (Chișinău, Moldova)
- · Maria Dinescu (Bucharest, Romania)
- Nikola Filipović (Niš, Serbia)
- Milan Kovačević (Kragujevac, Serbia)
- · Ana Mančić (Niš, Serbia)
- Peđa Mihailović (Belgrade, Serbia), secretary
- Stanko Nikolić (Belgrade, Serbia)
- · Vladan Pavlović (Niš, Serbia)
- Marica Popović (Belgrade, Serbia)
- Svetislav Savović (Kragujevac, Serbia)
- Milutin Stepić (Belgrade, Serbia), coordinator
- Rodica Vladoiu (Constanta, Romania)

#### 8. Plasma and Gas-Discharge Physics

- Gheorghe Dinescu (Bucharest, Romania)
- Saša Dujko (Belgrade, Serbia), coordinator
- · Saša Gocić (Niš, Serbia)
- · Zhivko Kissovski (Sofia, Bulgaria)
- Milan Kovačević (Kragujevac, Serbia)
- Bratislav Obradović (Belgrade, Serbia), coordinator
- Mara Šćepanović (Podgorica, Montenegro)

#### 9. Theoretical, Mathematical and Computational Physics

- Metin Arık (Istanbul, Turkey)
- · Miroljub Dugić (Kragujevac, Serbia)
- · Igor Franović (Belgrade, Serbia), coordinator
- Borislav Gajić (Belgrade, Serbia), secretary
- Aurelian Isar (Bucharest, Romania)
- Milan Milošević (Niš, Serbia)
- Klaudio Peqini (Tirana, Albania)
- · Slobodan Radošević (Novi Sad, Serbia)

- Radoslav Rashkov (Sofia, Bulgaria)
- · Neli Stoilova (Sofia, Bulgaria)

#### 10. Meteorology and Geophysics

- Ekaterina Bachvarova (Sofia, Bulgaria)
- · Vladimir Đurđević (Belgrade, Serbia), coordinator
- · Kostadin Ganev (Sofia, Bulgaria)
- · Slobodan Ničković (Belgrade, Serbia), secretary
- Klaudio Peqini (Tirana, Albania)
- Tanja Porja (Tirana, Albania)
- · Sabina Stefan (Bucharest, Romania)

#### 11. Environmental Physics - Alternative Sources of Energy

- Balis Dimitrios (Thessaloniki, Greece)
- Valentin Ivanovski (Belgrade, Serbia)
- Zoran Mijić (Belgrade, Serbia), coordinator
- Ioan Stamatin (Bucharest, Romania)
- · Ana Umićević (Belgrade, Serbia), secretary
- Petko Vitanov (Sofia, Bulgaria)
- Gerti Xhixha (Tirana, Albania)

#### 12. Physics of Socioeconomic Systems and Applied Physics

- Olta Çakaj (Tirana, Albania)
- Dragana Krstić (Kragujevac, Serbia)
- Mihail Lungu (Timisoara, Romania)
- · Vladimir Marković (Kragujevac, Serbia), secretary
- · Marija Mitrović Dankulov (Belgrade, Serbia), coordinator
- Petar Petrov (Sofia, Bulgaria)
- Dode Prenga (Tirana, Albania)
- Stavros Stavrinides (Thessaloniki, Greece)

#### 13. Biophysics and Medical Physics

- Aleksandar Krmpot (Belgrade, Serbia), coordinator
- Dragana Krstić (Kragujevac, Serbia), secretary
- · Mihai Radu (Bucharest, Romania)
- Miloš Vićić (Belgrade, Serbia)
- · Victoria Vitkova (Sofia, Bulgaria)
- · Gerti Xhixha (Tirana, Albania)
- · Emil Xhuvani (Tirana, Albania)

#### 14. Physics Education, History and Philosophy of Physics

- · Dejan Đokić (Belgrade, Serbia), secretary
- Maya Gaydarova (Sofia, Bulgaria)
- · Ivan Lalov (Sofia, Bulgaria)
- Dragana Malivuk Gak (Banja Luka, Bosnia and Herzcegovina)
- · Silvana Mico (Tirana, Albania)
- Violeta Petrović (Kragujevac, Serbia), coordinator
- Sebastian Popescu (Iasi, Romania)
- Stavros Stavrinides (Thessaloniki, Greece)
- · Maja Stojanović (Novi Sad, Serbia)
- Mira Vučeljić (Podgorica, Montenegro)
- Andrijana Žekić (Belgrade, Serbia)

#### 15. Metrology and Instrumentation

- Luljeta Gjeçi (Tirana, Albania)
- Aleksandar Kandić (Belgrade, Serbia)
- · Marina Lekić (Belgrade, Serbia), coordinator
- · Aurelian Luca (Bucharest, Romania)
- Ivan Stefanov (Sofia, Bulgaria)
- · Stevan Stojadinović (Belgrade, Serbia), secretary

#### **International Organizing Committee**

- Baki Akkuş (Istanbul, Turkey)
- · Lambe Barandovski (Skopje, North Macedonia)
- Ivan Belča (Belgrade, Serbia)
- · Luc Berge (DAM Arpjaon, France/ EPS P), co-chair
- · Aleksandar Bogojević (Belgrade, Serbia)
- Radu Constantinescu (Craiova, Romania)
- Dragoljub Dimitrijević (Niš, Serbia)
- Marija Dimitrijević Ćirić (Belgrade, Serbia)
- · Goran Djordjević (Niš, Serbia), co-chair
- Polikron Dhoqina (Tirana, Albania)
- Danica Dobrosavljevic (Niš, Serbia)
- Nikola Filipović (Niš, Serbia)
- · Ertan Güdekli (Istanbul, Turkey)
- Valentin Ivanovski (Belgrade, Serbia)
- · Jasmina Jeknić Dugić (Niš, Serbia)
- · Božidar Jovanović (Belgrade, Serbia)
- · Nikola Konjik (Belgrade, Serbia)
- Milan Kovačević (Kragujevac, Serbia)
- · Nenad Lazarević (Belgrade, Serbia)
- David Lee (Mulhouse, France / EPS GS)
- Vladimir Marković (Kragujevac, Serbia)
- Milan Milošević (Niš, Serbia)
- · Peđa Mihailović (Belgrade, Serbia), TBC
- Predrag Miranović (Podgorica, Montenegro)
- Dušan Mrđa (Novi Sad, Serbia)
- Zoran Ognjanović (Belgrade, Serbia)
- Şener Oktik (Istanbul, Turkey)
- · Snežana Pajović (Belgrade, Serbia)
- Milica Pavkov Hrvojević (Novi Sad, Serbia)
- Alexander Petrov (Sofia, Bulgaria)
- Goran Poparić (Belgrade, Serbia)
- · Zoran Rakić (Belgrade, Serbia)
- Goran Ristić (Niš, Serbia)
- Nenad Stevanović (Kragujevac, Serbia)

### **BPU11 CONGRESS**

11th International Conference of The Balkan Physical Union 28 August – 1 September 2022, Belgrade, Serbia

THIS CERTIFIES THAT

# MILAN JOCIĆ

he/she presented contribution **S06-CMPSP-108** with title **Ab-initio calculations of the temperature-dependent band gap of inorganic halide perovskites** as **Oral presentation**.

Prof. Dr. Dragoljub D. Dimitrijević Chair of the BPU11 LOC FOUNDED 1985

Prof. Dr. Goran Djordjevic President of the BPU



# NINETEENTH YOUNG RESEARCHERS' CONFERENCE MATERIALS SCIENCE AND ENGINEERING

December 1-3, 2021, Belgrade, Serbia

## Program and the Book of Abstracts

Materials Research Society of Serbia &

Institute of Technical Sciences of SASA

Book title:

Nineteenth Young Researchers' Conference - Materials Science and Engineering: Program and the Book of Abstracts

Publisher:

Institute of Technical Sciences of SASA Knez Mihailova 35/IV, 11000 Belgrade, Serbia

Tel: +381-11-2636994, 2185263, http://www.itn.sanu.ac.rs

Conference organizers:

Materials Research Society of Serbia, Belgrade, Serbia Institute of Technical Sciences of SASA, Belgrade, Serbia

Editor:

Dr. Smilja Marković

Technical Editor: Aleksandra Stojičić

Cover page: Aleksandra Stojičić and Milica Ševkušić

Cover: Milica Ševkušić

Printing:

Gama digital centar

Autoput No. 6, 11070 Belgrade, Serbia

Tel: +381-11-6306992, 6306962

http://www.gdc.rs

Publication year: 2021

Print-run: 120 copies

CIP - Каталогизација у публикацији

Народна библиотека Србије, Београд

66.017/.018(048)

#### YOUNG Researchers Conference Materials Sciences and Engineering (19; 2021; Beograd)

Program; and the Book of abstracts / Nineteenth Young Researchers' Conference Materials Science and Engineering, December 1-3, 2021, Belgrade, Serbia; [organized by] Materials Research Society of Serbia & Institute of Technical Sciences of SASA; [editor Smilja Marković]. - Belgrade: Institute of Technical Sciences of SASA, 2021 (Belgrade: Gama digital centar). - XVIII, 86 str.: ilustr.; 23 cm

Tiraž 120. - Registar.

ISBN 978-86-80321-36-3

а) Наука о материјалима -- Апстракти б) Технички материјали – Апстракти

COBISS.SR-ID 51231241

#### Aim of the Conference

Main aim of the conference is to enable young researchers (post-graduate, master or doctoral student, or a PhD holder younger than 35) working in the field of materials science and engineering, to meet their colleagues and exchange experiences about their research.

#### **Topics**

Biomaterials

Environmental science

Materials for high-technology applications Materials for new generation solar cells

Nanostructured materials

New synthesis and processing methods

Theoretical modelling of materials

#### **Scientific and Organizing Committee**

Committee President

Smilja Marković Institute of Technical Sciences of SASA, Belgrade, Serbia

Vice-presidents

Dragana Jugović Institute of Technical Sciences of SASA, Belgrade, Serbia Magdalena Stevanović Institute of Technical Sciences of SASA, Belgrade, Serbia Faculty of Technology and Metallurgy, Belgrade, Serbia

Members

Tatiana Demina Enikolopov Institute of Synthetic Polymeric Materials,

Russian Academy of Sciences

Jasmina Dostanić Institute of Chemistry, Technology and Metallurgy, Belgrade,

Serbia

Xuesen Du Chongqing University, Chongqing, China Branka Hadžić Institute of Physics, Belgrade, Serbia

Ivana Jevremović Norwegian University of Science and Technology, Trondheim,

Norway

Sonja Jovanović Institute of Nuclear Sciences "Vinča", Belgrade, Serbia

Snežana Lazić Universidad Autónoma de Madrid, Spain

Lidija Mančić Institute of Technical Sciences of SASA, Belgrade, Serbia

Marija Milanović Faculty of Technology, Novi Sad, Serbia

Miloš Milović Institute of Technical Sciences of SASA, Belgrade, Serbia

Nebojša Mitrović Faculty of Technical Sciences, Čačak, Serbia

Irena Nikolić Faculty of Metallurgy and Technology, Podgorica, Montenegro

Marko Opačić Institute of Physics, Belgrade, Serbia

Vuk Radmilović Faculty of Technology and Metallurgy, Belgrade, Serbia Tatjana D. Savić Institute of Nuclear Sciences "Vinča", Belgrade, Serbia Ana Stanković Institute of Technical Sciences of SASA, Belgrade, Serbia

Srečo Škapin Institute Jožef Stefan, Ljubljana, Slovenia Boban Stojanović Faculty of Sciences, Kragujevac, Serbia

## Nineteenth Young Researchers Conference – Materials Science and Engineering December 1-3, 2021, Belgrade, Serbia

Ivana Stojković-Simatović Faculty of Physical Chemistry, Belgrade, Serbia

Konrad Terpiłowski Department of Interfacial Phenomena, Institute of Chemical

Sciences, Faculty of Chemistry, Maria Curie-Skłodowska

University in Lublin, Poland

Vuk Uskoković TardigradeNano, Irvine, CA, USA Rastko Vasilić Faculty of Physics, Belgrade, Serbia

Ljiljana Veselinović Institute of Technical Sciences of SASA, Belgrade, Serbia Siniša Vučenović Faculty of Sciences, Department of Physics, Banja Luka, B&H

Marija Vukomanović Institute Jožef Stefan, Ljubljana, Slovenia

Conference Secretary

Aleksandra Stojičić Institute of Technical Sciences of SASA, Belgrade, Serbia

#### **Conference Technical Committee**

Milica Ševkušić, Ivana Dinić, Marina Vuković, Vukašin Ugrinović, Tamara Matić

#### **Results of the Conference**

Beside printed «Program and the Book of Abstracts», which is disseminated to all conference participants, selected and awarded peer-reviewed papers will be published in journal "Tehnika – Novi Materijali". The best presented papers, suggested by Session Chairpersons and selected by Awards Committee, will be proclaimed at the Closing Ceremony. Part of the award is free-of-charge conference fee at YUCOMAT 2022.

#### **Sponsors**



#### Acknowledgement

The editor and the publisher of the Book of abstracts are grateful to the Ministry of Education, Sciences and Technological Development of the Republic of Serbia for its financial support of this book and The Nineteenth Young Researchers' Conference - Materials Sciences and Engineering, held in Belgrade, Serbia.

9-4

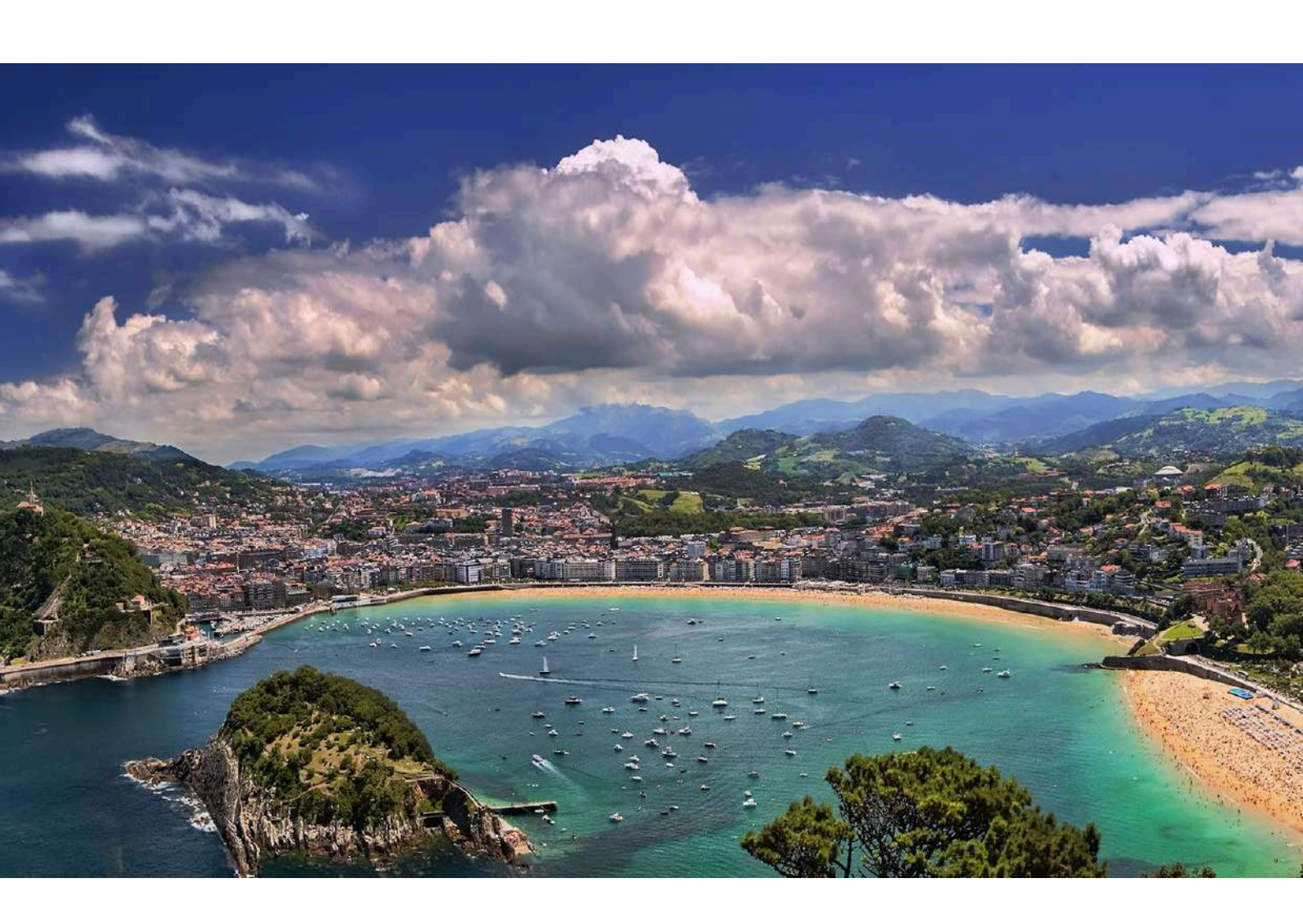
### Construction of Symmetry-adapted k.p Hamiltonians for semiconductor nanostructures

Milan Jocić, Nenad Vukmirović Institute of Physics Belgrade, University of Belgrade, Pregrevica 118, 11080 Belgrade, Serbia

Using ab-initio methods like DFT for nanostructures is computationally very expensive, even with modern supercomputers. However, we will show that an accurate quantitative picture can be obtained with a k.p method by starting with Kohn-Sham (KS) states obtained from ab-initio calculations for bulk structure. We demonstrate this by comparing k.p with DFT calculations for the case of CdSe quantum wells. We obtain the analytical form and numerical parameters of well-studied 4x4 and 8x8 k.p Hamiltonians found in literature, for the case where spin-orbit coupling is omitted and included, respectively. Also, we demonstrate an improvement over 4x4 and 8x8 Hamiltonians, by expanding the number of states from 4(8) to 13(26), which yields more accurate excited states. Another improvement can be made, by using the GW approximation within the many-body perturbation theory, thus correcting the DFT electronic structure. This method can give more accurate bulk band gaps, which in turn yields improved results for nanostructures.

ETSF Young Researchers'
Meeting
2-7 June, 2019
San Sebastian, Spain





### Dear colleagues,

Welcome to 16th ETSF Young Researchers' Meeting, San Sebastian 2019. The Young Researchers' Meeting (YRM) of the European Theoretical Spectroscopy Facility (ETSF) is an annual meeting of the first stage researchers (MSc and PhD students and Postdoctoral researchers) who work on the novel theoretical and computational approaches to study electronic and optical properties of materials. This meeting provides researchers in beginning of their careers opportunity to share their work, introduce themselves with state-of-the-art theoretical methods for describing properties of materials, exchange ideas and make connections with other researchers at similar point of career.

YRM 2019 will have five oral sessions. Topics of all the sessions will be on ab-initio approaches of modelling material properties. First session will be on the ground state of the system and second will be on excited states of atomic, molecular and solid state systems. Third session will be on vibrational properties of materials. Fourth session will be on multi-scale simulation and fifth session will be on highly-correlated systems.

Conference will also host poster session where some of the participants will have opportunity to show their work in graphical representation and to explain it to other researchers in less formal way. Industry session is also scheduled where people who transferred from academia to industry will tell participants their experiences and provide them with insight in needs and expectations of industry regarding physicists and material scientists.

Contents

Conference Location	vii
Conference talks	1
Spin in Quantum Materials (Manuel dos Santos Dias)	. 2
Mori $Sanchez^2$ )	. 3
High-Pressure Iron as a Spin-Smectic State (Tommaso Gorni <sup>1</sup> )	
Analysis of defect states in MoSe <sub>2</sub> and unfolding of defect band structure (Stefan Rost <sup>1</sup> , Christoph Friedrich <sup>1</sup> , Irene Aguilera <sup>1</sup> , Beata Kardynal <sup>1</sup> , Stefan Blügel <sup>1</sup> )	. 5
Charge-transfer features in the exact Kohn-Sham potential of ensemble density functional theory for excited states (M. J. P. Hodgson <sup>1</sup> , Eli	
$Kraisler^{1,2}$ , $Axel\ Schild^{1,3}$ and $E.\ K.\ U.\ Gross^{1,2}$ ) Stable ordered phases of cuprous iodide with complexes of copper vacancies	. 6
$(M\'{a}rio~Rui~Gonçalves^1)$	. 7
Charge disproportionation, mixed valence, and Janus effect in multiorbital	0
systems: A tale of two insulators (Aldo Isidori <sup>1</sup> )	
Orbital selectivity in Hund's correlated metals $(Maja\ Berovic^1)$ Enhanced electronic compressibility in a doped Mott insulator in the pres-	. 9
ence of a crystal field (Maria Chatzieleftheriou <sup>1</sup> , Maja Berovic <sup>2</sup> , Pablo Villar Arribi <sup>1</sup> , Massimo Capone <sup>2</sup> , Luca de' Medici <sup>1</sup> )	. 10
Effect of van Hove singularities in the quasiparticle weight (Pablo Villar	
$Arribi^1$ and $Luca$ de $Medici^1$ )	. 11
Charge and spin transport in correlated nano-junctions (Andrea Droghetti Advantageous nearsightedness of many-body perturbation theory contrasted	
with Kohn-Sham density functional theory <sup>1</sup> (Jack Wetherell)	
Superconductivity, Pseudogap and Their Interplay with the Mott Transi-	
tion (Lorenzo Fratino)	. 14
Amplification of magneto-optical activity via hybridization with dark plasmons in magnetoplasmonic nanocavities ( <i>Mario Zapata Herrera</i> )	. 15
Ultrafast relaxation of symmetry-breaking photo-induced atomic forces	
(Shane M. O'Mahony <sup>1,2</sup> , Felipe Murphy-Armando <sup>1</sup> , Éamonn D. Murra	
<sup>1</sup> , José D. Querales-Flores <sup>1</sup> , Ivana Savić <sup>1</sup> , Stephen Fahy <sup>1,2</sup> ) Towards optimal orbital description of molecules and solids. (Aleksei Ivanov	
Elvar Örn Jónsson <sup>1</sup> , Hannes Jónsson <sup>1</sup> )	. 17
Dielectric function of homogeneous electron gas from Bethe-Salpeter equation (J. $Koskelo^{1,2}$ , M. $Panholzer^{3,2}$ , L. $Reining^{1,2}$ , M. $Gatti^{1,2,4}$ )	. 18
DFT ground-state based approaches in the simulation of core-level excita-	
tion energies ( $Georg S. Michelitsch^1$ )	. 19
Going beyond TDDFT for some of its pathological cases: double excitations and magnetic excitations ( <i>Elisa Rebolini</i> )	. 20
Anharmonic Properties of Solids within the Stochastic Self-Consistent Harmonic Approximation: Phonons, Second-Order Structural Phase Transition of the Phonons of the Phono	
sitions, and Thermal Properties (Ion Errea)	. 22
Quantum Anharmonic Effects on the Superconducting $LaH_{10}$ ( <u>F.Belli</u> <sup>1,2*</sup> , I. $Errea^{1,2,3}$ )	. 23

Phonon collapse and second-order phase transition in thermoelectric SnSe	
(Unai Aseginolaza <sup>1,2,3</sup> , Raffaello Bianco <sup>4,5,6</sup> , Lorenzo Monacelli <sup>4</sup> , Lorenzo	
Paulatto <sup>7</sup> , Matteo Calandra <sup>8</sup> , Francesco Mauri <sup>4,5</sup> , Aitor Bergara <sup>1,2,9</sup>	
	25
,	20
Prediction of photoinduced phase transitions and coherent optical phonon	
generation in $BaTiO_3$ (Fangyuan GU, amonn Murray, and Paul Tangney)	27
Anharmonicity and electron-doping determine the charge density wave crit-	
ical temperature in single-layer TiSe <sub>2</sub> (Jianqiang Sky Zhou <sup>1</sup> , Lorenzo	
Monacelli <sup>2</sup> , Raffaello Bianco <sup>2,3</sup> , Ion Errea <sup>4,5,6</sup> , Fracesco Mauri <sup>2,3</sup> , and	
1.	28
Multi-scale journey through the molecular mechanisms of colour expression	20
in anthocyanins (Sara Laporte <sup>1</sup> , Mariami Rusishvili <sup>1,2</sup> , Luca Grisanti <sup>1,3</sup> ,	20
, ,	29
Multiscale atomistic simulations in the wake of machine learning (Miguel	
$A.\ Caro)$	30
Understanding X-ray spectroscopy of carbonaceous materials by combining	
simulations with experimental data (Anja Aarva <sup>1</sup> , Volker L. Deringer <sup>2,3</sup> ,	
	31
Machine learning the exchange-correlation functional of DFT: a Jacob-	<b>J</b>
selevator through modern neural networks architecture (Jonathan	
•	0.0
, , , , , , , , , , , , , , , , , , , ,	33
Fundamental energy gaps from grand canonical quantum Monte Carlo cal-	
culations applied to solid hydrogen (Vitaly Gorelov <sup>1</sup> , Markus Holzmann <sup>2,3</sup> ,	
$D.M. \ Ceperley^4, \ Carlo \ Pierleoni^{1,5}) \ \dots \dots \dots \dots \dots \dots \dots$	34
	35
Ab initio study of possible metastable occupation of tetrahedral sites in	
Palladium Hydride compounds (Antonella Meninno <sup>1,2</sup> and Ion Errea	
$^{1,2,3})$	35
Ab initio study of Silver chloride: Modelization of the dielectric function	
	37
Excitations in the Raman spectra of $SrRu_2O_6$ with honeycomb lattice.	01
- · · · · · · · · · · · · · · · · · · ·	
(Yu.S. Ponosov <sup>1,2</sup> , E.V. Komleva <sup>1</sup> , D. A. Zamyatin <sup>3</sup> , R. I. Walton <sup>4</sup>	00
,	38
Electron-phonon coupling in hybrid inorganic/organic systems from first-	
principles (Ignacio Gonzalez Oliva, Fabio Caruso and Claudia Draxl)	39
Construction of symmetry adapted $k \cdot p$ Hamiltonian from DFT calcula-	
tions (Milan Jocić, Nenad Vukmirović)	40
Theoretical description of non-linear processes in magnetic materials (Shalu	
	42
,	14
Surface spectroscopy of Si(001) surface functionalized with nucleobases	40
$(Stefano\ Mazzei^1,\ Christine\ Giorgetti^1,\ Val\'erie\ V\'eniard^1)\ \dots\ \dots\ \dots$	43
Author Indox	15
Author Index	45

# Construction of symmetry adapted $k \cdot p$ Hamiltonian from DFT calculations

Milan Jocić, Nenad Vukmirović

Scientific Computing Laboratory, Center for the Study of Complex Systems, Institute of Physics Belgrade, University of Belgrade, Pregrevica 118, 11080 Belgrade, Serbia

Electronic structure of semiconductors and their nanostructures can be described using the well known  $\mathbf{k} \cdot \mathbf{p}$  perturbation theory of Kane for bulk materials and Burt for heterostructures. Corresponding Hamiltonians are represented in a basis of Bloch wave-functions and parameters of the Hamiltonian are related to momentum matrix elements between the basis states. Due to crystal symmetry some of these matrix elements vanish, while some have the same value and consequently the  $\mathbf{k}$ . **p** Hamiltonian has a relatively simple form with a limited number of parameters. However, there is still no automatic way to obtain the  $\mathbf{k} \cdot \mathbf{p}$  Hamiltonian in this standard symmetrical form from ab-initio electronic structure calculation. In this work, we established the procedure to achieve this. The first step of the procedure is to perform density functional theory calculation of material band structure and obtain the Kohn-Sham wave-functions. Next, for each of these wave-functions we determine the corresponding irreducible representation of the symmetry group and transform them to a standard symmetry-adapted basis. We then calculate the momentum matrix elements in this basis which leads to the parameters of desired  $\mathbf{k} \cdot \mathbf{p}$ Hamiltonian. We illustrate the method by applying it to cubic lead-based perovskite CsPbBr<sub>3</sub> as seen in Figure below.

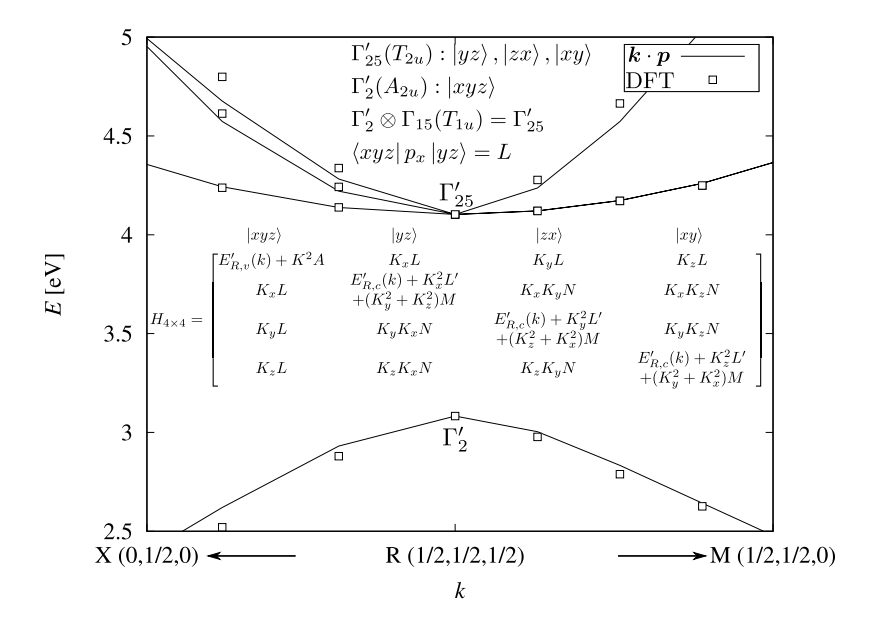


Figure 7: Calculated band structure of CsPbBr<sub>3</sub> near the band-gap (point R) obtained from DFT (squares) and from symmetry-adapted  $\mathbf{k} \cdot \mathbf{p}$  Hamiltonian (full line). Valence and conduction states at R correspond to irreducible representations  $\Gamma_2'$  and  $\Gamma_{25}'$ , respectively. Alternative labels for irreducible representations, their partners and their product as well as an example of momentum matrix element are shown in the top inset. The symmetry-adapted  $\mathbf{k} \cdot \mathbf{p}$  Hamiltonian is shown in the bottom inset.